國立臺灣師範大學科技與工程學院

光電工程研究所

博士論文

Graduate Institute of Electro-Optical Engineering

College of Technology and Engineering

National Taiwan Normal University

Doctoral Dissertation

光學共振生物感測器的計算和實驗方法：從LSPR到SPR - 拉曼積分和無金屬有損模式共振

Computational and Experimental Approach in Optical Resonance Biosensors: From LSPR to SPR- Raman Integration and Metal-Free Lossy Mode Resonance

Devi Taufiq Nurrohman

指導教授：邱南福 博士

Advisor: Nan-Fu Chiu Ph.D.

中華民國 114 年 8 月

August 2025

Acknowledgement

First, I would like to express my deepest gratitude to Prof. Nan-Fu Chiu for giving me the opportunity to study in his laboratory. His guidance and knowledge have been invaluable throughout my academic journey. I am also very grateful for the financial support he has given me during my studies as an international student at NTNU.

I want to thank all my colleagues from the Laboratory of Quantum Photonics and Biosensors, especially Ming-Jung Tai, Gerald Reymari Acoba Cagayan, and Rou-Chen Lin, for their help and support during my research. I am also thankful to my friend "*Muhammad Saukani*" and "*my apartment mates*" for their thoughtful advice and encouragement. To my friends at PPI (Indonesian Student Association in Taiwan), I am truly grateful for your companionship and support throughout my journey in Taiwan.

Lastly, I wish to dedicate my deepest thanks to my family. To my beloved wife and children, your unwavering prayers, support, and presence have been my greatest strength during my studies in Taiwan. To my father and mother in Indonesia, thank you for your patience and prayers, which have been instrumental in the smooth progress of my studies.

Abstract

Computational studies have become an essential complement to research, enabling the exploration of physical phenomena that are challenging or even impossible to observe experimentally. In this thesis, computational and experimental studies were conducted in studying resonance-based optical biosensors, namely Localized Surface Plasmon Resonance (LSPR), integration of Surface Plasmon Resonance (SPR) and Raman, and non-metal optical sensors. In LSPR-based optical sensors, the investigation focuses on the interaction of the gold nanoparticle (AuNPs) transducer used for BSA detection. Experimental results reveal the presence of the Hook effect, characterized by a decrease in the LSPR signal response. From a computational perspective, the dielectric layer on the AuNPs surface enhances the electric field, disrupting the LSPR signal, particularly in the aggregated state.

In the integration of SPR sensors with Raman technology, a one-dimensional (1D) gold grating chip was selected as the transducer. Reflectance map analysis identified a surface plasmon mode (SPM) at grating periods ranging from 644 nm to 800 nm. Additionally, a distinct resonance mode, known as cavity mode (CM), was observed, exhibiting a different signal response from the SPR mode when tested with varying refractive indices of the sensing medium. The experimental results further confirmed that the Raman signal can still be enhanced by utilizing the electric field generated due to SPR excitation.

In the third study, the investigation focuses on finding material combinations that can replace SPR sensors, which heavily rely on gold as transducers. In this context, two-dimensional (2D) materials such as MoS_2, and WS_2 have been selected as lossy layers, with their performance optimized by incorporating a matching layer of Cytop or MgF_2. Computational results indicate that Lossy Mode Resonance (LMR) sensor utilizing Cytop and WS_2 exhibits excellent signal quality and stability. This sensor also offers a wider dynamic range, capable of detecting refractive indices up to 1.5, which exceeds the detection capability of SPR sensors excited at either 633 nm or 670 nm. Additionally, the proposed structure provides a longer penetration depth than SPR sensors, making it highly promising for detecting analytes ranging from the nanoscale to the microscale.

Overall, the findings of this study are expected to serve as a reference in designing more effective and accurate optical biosensors for biomedical and chemical applications, by understanding their signal characteristics and electric field characteristics to maximize sensor performance. The study's contributions include optimizing resonance-based biosensors to improve sensitivity and accuracy in detection applications, which can support the development of future diagnostic devices.

Keywords: *Localized Surface Plasmon Resonance, Surface Plasmon Resonance, Raman scattering, Lossy Mode Resonance*

Table of Contents

List of Figures

List of Tables

Abbreviations and Symbols

A	: Absorbance intensity
AgNT	: Silver nanotriangle
aq	: Aqueous
ATR	: Attenuated Total Reflection
Au	: Gold
AuNPs	: Gold nanoparticles
CHA	: Catalytic hairpin assembly
CM	: Cavity mode
Cr	: Chromium
CRP	: C-reactive protein
Cys	: Cystamine dihydrochloride
c_m	: The concentration of the sample
d	: The effective adsorbate layer thickness
DFM	: Dark-field microscopy
EIS	: Electrochemical Impedance Spectroscopy
FDTD	: Finite different time domain
FO	: Fiber optics
FoM	: Figure of merit
$FWHM$	: Full-width half maximum
h	: Grating height
I_{RS}	: Signal intensity on plane Au film
I_{SERS}	: Signal intensity on grating with λ_{RS} excitation
$I_{SERS+SPR}$	: Signal intensity on grating with λ_{RS} and λ_{SPR} excitation
ITO	: Indium tin oxide
k	: Extinction coefficient
L	: Path length
LMR	: Lossy mode resonance
LSPR	: Localized surface plasmon resonance
l_d	: Electromagnetic field decay length
m	: Diffraction order
MB	: Methylene blue
MLWA	: Modified long wavelength approximation
N	: Avogadro's number
n_{p}	: Refractive index of prism
n_{s}	: Refractive index of sensing medium
Λ	: Periodicity of grating
PD	: Penetration depth
PMMA	: Polymethyl methacrylate

p-NA : p-nitroaniline (p-NA)
P_{RS} : Laser power from the Raman system
R : Radius
R_{min} : Minimum reflectance
R6G : Rhodamine 6G
S : Sensitivity
SERS : Surface-enhanced Raman scattering
SPM : Surface plasmon mode
SPR : Surface plasmon resonance
TMM : Transfer Matrix Method
w : Grating line width
θ_C : Critical angle
ε : Dielectric constant of material
λ : Wavelength
λ_{LMR} : LMR wavelength
λ_{LSPR} : LSPR wavelength or LSPR peak
λ_{RS} : Incident wavelength of the Raman
λ_{SPR} : SPR wavelength
$\Delta\lambda_{LSPR}$: Shift in resonance wavelength
Δn : The change in refractive index induced by the adsorbate
1D : One-dimensional
2D : Two-dimensional
3WJ : Multi-functional DNA 3 way-junction
4-MBA : 4-mercaptobenzoic acid

Chapter 1

Introduction

1.1 Background

Biosensors are devices designed to detect and measure the presence of specific biological substances and molecular compounds in biological samples (Mostufa et al., 2024)(Y. Kim et al., 2021). These devices consist of a molecular recognition element (receptor) such as an antibody, enzyme, or DNA that interacts with a molecular target (analyte), and a transducer that converts the interaction into a physical signal that can be analyzed (Damborský et al., 2016).

In addition, optical biosensors are not only capable of measuring bioassay concentrations but also provide in-depth information about binding kinetics such as association, dissociation and affinity constants (Khansili et al., 2018). The primary purpose of an optical biosensor is to generate a signal that is directly proportional to the concentration of the target substance (analyte). As illustrated in the scheme in Figure 1. 1, optical biosensors can be implemented using optical transducers based on SPR, LSPR, resonators, gratings, or refractometers. The interaction between the receptor and the target induces changes in the optical properties of the transducer, which can be observed through shifts in wavelength (K. Liu et al., 2020), variations

in light intensity (transmission, reflection, or absorption) (Mostufa et al., 2024), or changes in resonance angles (Meza-Sánchez & Maravillas-Montero, 2019).

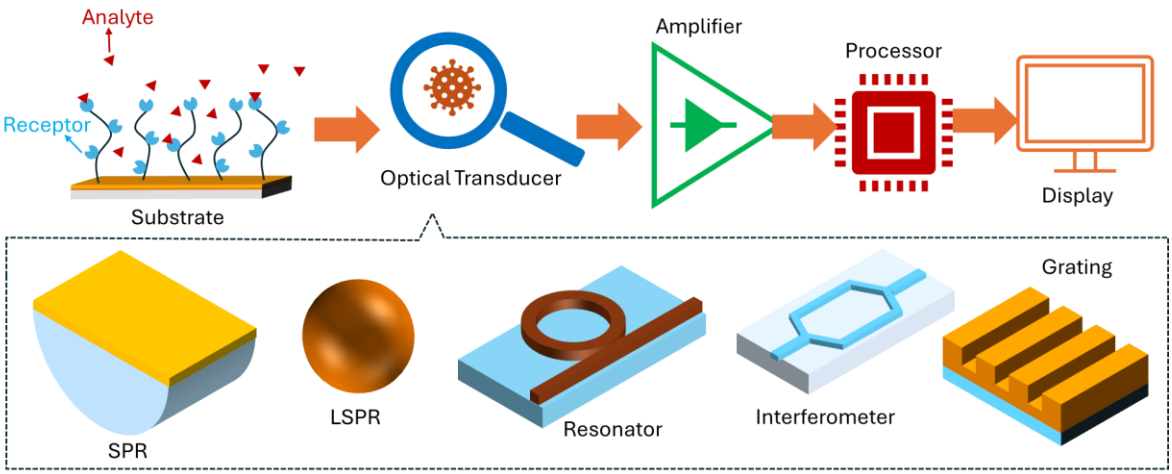

Figure 1. 1 Working principle of optical biosensor.

LSPR sensors operate by leveraging the collective oscillation of electrons on the surface of metal nanoparticles, which are highly sensitive to changes in the surrounding refractive index. The interaction between the target and the immobilized receptor on the nanoparticle surface influences the LSPR wavelength position. A comprehensive study of LSPR signal interactions through both computational and experimental approaches is crucial for ensuring the accuracy and validity of experimental results. Computational methods offer deeper theoretical insights that may be challenging to observe experimentally, while experiments serve to validate theoretical models. By integrating these two approaches, researchers can gain a more profound understanding of LSPR interactions, ensuring signal validity and identifying unusual experimental signals.

In addition to LSPR, SPR technology has long been used in optical sensors due to its high sensitivity to refractive index changes. However, SPR still has limitations in terms of selectivity and specific analyte identification capabilities. One way to improve the performance of SPR sensors is to integrate them with Raman spectroscopy in the same system. This integration allows the sensor to not only detect changes in analyte concentration in real time but also provide analyte fingerprint information through Raman spectra. Thus, combining SPR and Raman in one sensor platform can produce a more comprehensive and accurate device for various analytical applications.

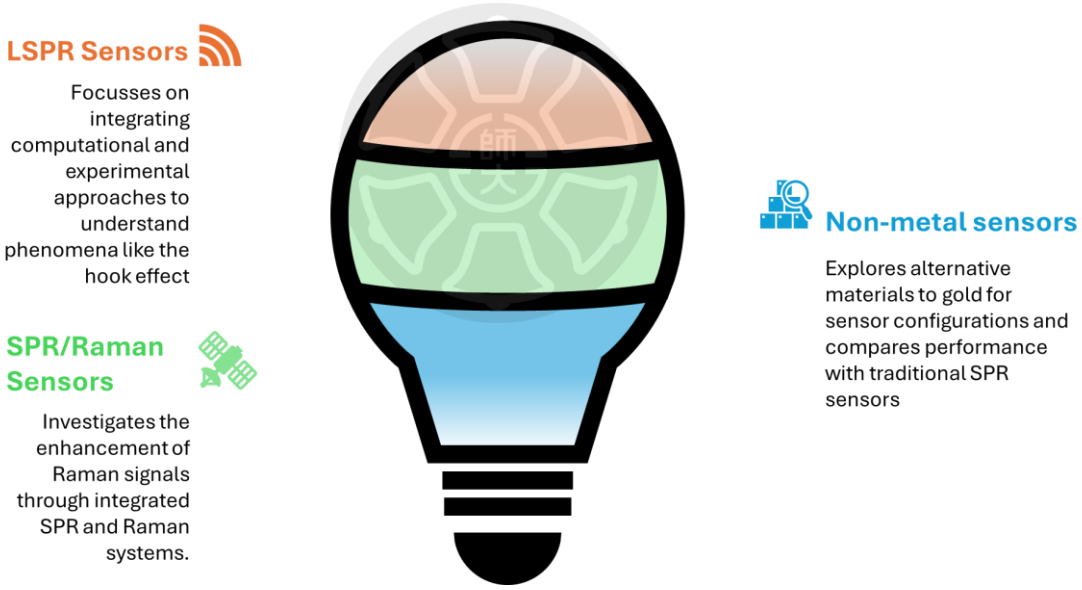

Figure 1. 2 Schematic diagram to provide a brief overview of the focus of the investigation in this study.

Although SPR-based sensors offer many advantages, the use of metallic materials in these sensors can limit their efficiency and flexibility. In most SPR biosensors, gold remains the primary transducer material, which limits the sensor

performance and hinders the development of cost-effective alternatives. In addition, the addition of 2D materials such as graphene on the metal surface results in a broader SPR curve, reducing the sharpness of the SPR curve and this has a critical impact on sensor precision (Tene et al., 2024). Recent research has increasingly focused on metal-free optical sensors as a promising replacement for SPR-based systems. One such approach involves 1D photonic crystal-based sensors, which have been investigated by Maurya et al., utilizing alternating layers of 2D materials and PMMA or silicon (Maurya et al., 2018). Another alternative is surface plasmon-coupled emission, as explored by Bhaskar et al. in 2021 (Bhaskar et al., 2021). In addition, optical sensors based on lossy materials have also attracted attention. These sensors offer greater flexibility with a wider range of transducer materials, presenting innovative solutions for low-cost, high-performance optical detection.

Building on this background, this study focuses on optical sensors that operate based on resonance mechanisms. The key aspects under investigation are illustrated in Figure 1. 2. The first study is related to LSPR sensors and will focus on understanding the characteristics of LSPR sensor signals through computational and experimental approaches. After that, the study will continue to develop the integration of SPR and Raman in one system to improve sensor performance and also explore metal-free optical sensors as alternative sensors to replace SPR sensors. The metal-free sensors investigated will focus on optical sensors coupled with prisms. The results of this study are expected to provide significant contributions to the development of more accurate, sensitive, and low-cost optical sensors.

1.2 Thesis Structure

The data presented in this thesis has been published in *IEEE Sensors Journal*, *Optics Express*, *Advanced Theory and Simulations*, and *ECS Journal of Solid State Science and Technology*. Accordingly, each subtopic is organized into separate chapters, which are outlined as follows:

Chapter 1 is an introduction that contains three main subtopics, namely the research background and thesis structure.

Chapter 2 discusses the first type of biosensor, namely the LSPR biosensor. In each subtopic, it will begin by explaining the working principle of each biosensor and continue by reviewing some literature to show the research gap. After that, the study continues by explaining the research method and the results obtained.

Chapter 3 discusses the results of research related to the integration of SPR and Raman biosensors. The contents of this section are similar to the previous section. In simple terms, this section includes working principle of the sensor, literature review, research methods and findings.

Chapter 4 discusses the third type of sensor which is a resonance-based sensor that does not use metal as its transducer. In this section, the performance of LMR-based metal-free sensors and SPR-based metal-based sensors are compared in terms of sensitivity, signal quality, detection range and penetration depth (PD) of the sensor.

Chapter 5 presents a summary of the research results from each subtopic studied. This chapter also includes proposed improvements and recommendations for the development of optical biosensors in the future.

This thesis integrates numerical simulations using the FDTD method with experimental studies to analyze LSPR signal characteristics and the integration of SPR and Raman biosensors. For metal-free optical sensors, the research remains focused on numerical studies. Specifically, sensors with thin-film transducers are analyzed using the transfer matrix method, considering variations in film thickness, excitation wavelength, and polarization type. Key aspects investigated include the sensor's dynamic range and penetration depth. The findings on metal-free sensors with wide dynamic ranges and deep penetration depths contribute to advancing optical biosensor technology, expanding its potential applications.

Chapter 2

Exploring Interaction Phenomena in AuNPs-Based LSPR Immunosensors: Experimental and Computational Insights

2.1 Introduction

2.1.1 Working principle of LSPR biosensor

LSPR biosensors have become widely used to detect various analytes such as cortisol (Jeon et al., 2018), alanine aminotransferase (Singh et al., 2023), and fipronil (Yoo et al., 2022). This type of sensor works by utilizing LSPR phenomenon which is generated by metal nanoparticles such as gold and silver. When metal nanoparticles are exposed to light of a certain wavelength, free electrons on the metal surface begin to oscillate collectively at a certain resonance frequency as shown in Figure 2. 1 (a). This resonance is characterized by dominant light absorption at a certain frequency and its position depends on the size, shape, material, and environment around the nanoparticle.

LSPR phenomenon is very sensitive to the interaction phenomenon that occurs on the surface of nanoparticles. The interaction that occurs can be easily identified by analyzing the change in the resonance position of the LSPR sensor. In the LSPR biosensor, the surface of the nanoparticle is coated with a functional layer

that can bind the target analyte. The target that binds to the functional layer will change the local refractive index around the nanoparticle and the position of the resonance frequency of the LSPR biosensor as shown in Figure 2. 1 (b). The evanescent field length of the LSPR Biosensor is in the order of 6 nm and this characteristic makes the LSPR biosensor very sensitive and an ideal platform for detecting small-sized target analytes such as ions, peptides and proteins (Hammond et al., 2014).

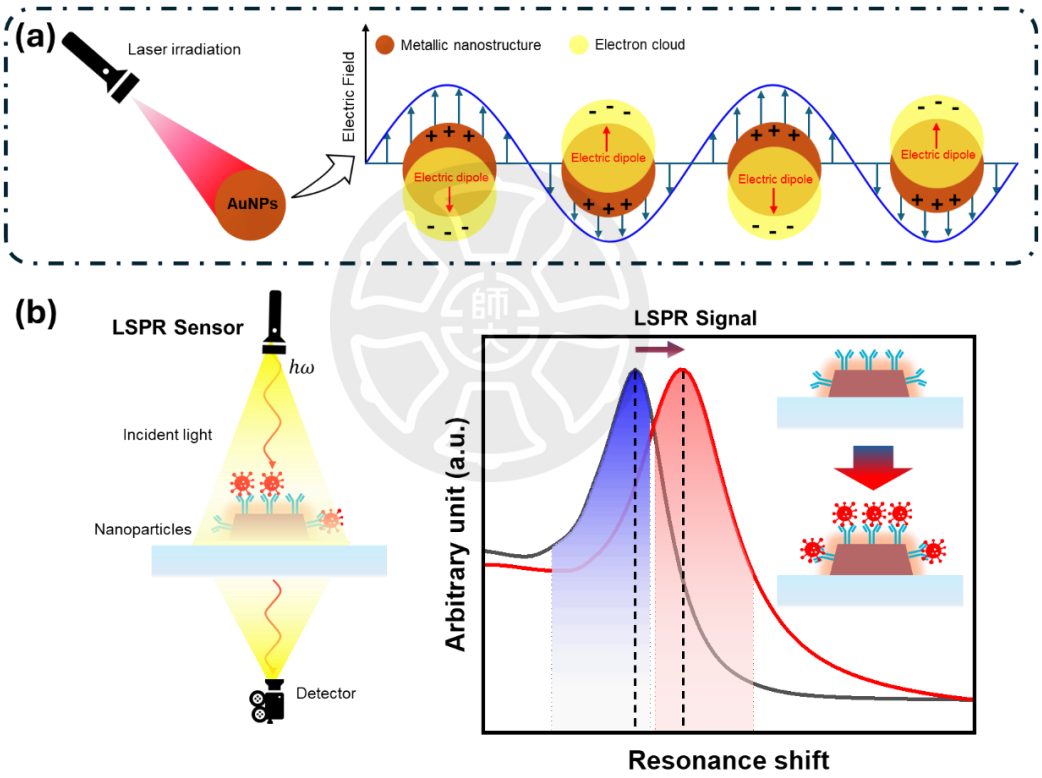

Figure 2. 1 (a) Illustration of localized plasmon oscillation of metal nanoparticles under incident light radiation, (b) LSPR biosensor and its working principle.

Optical parameters that can be measured in LSPR biosensors include extinction (Farooq et al., 2018), absorbance (Yoo et al., 2022), transmission (T. Liu et al., 2021), and reflection signals (Lin et al., 2011). In the simplest LSPR sensors,

extinction and absorbance measurements are generally performed using a UV-Vis spectrometer. In addition, LSPR sensors can also be designed based on optical fibers, where the parameters measured are usually transmission and reflectance, as shown in Figure 2. 2.

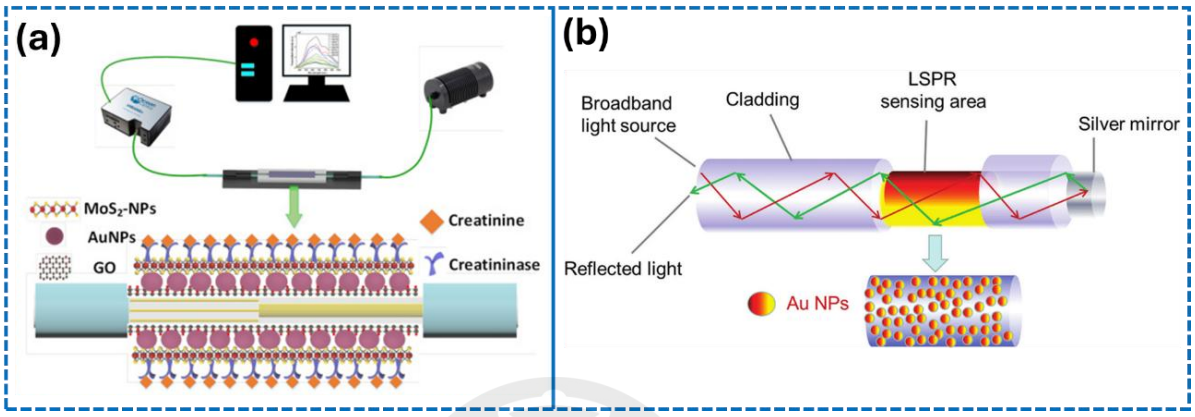

Figure 2. 2 LSPR sensors which utilize (a) transmission and (b) reflection signals in their work. Figure adapted from Ref. (M. Li et al., 2021)(Qian et al., 2020)*, licensed under CC BY 4.0.*

There are several investigation modes that are commonly used in LSPR biosensors. One that is widely used is using the wavelength investigation mode. This investigation mode utilizes the shift in the resonance wavelength ($\Delta\lambda_{LSPR}$) that is directly correlated with the concentration of target molecules bound to the nanoparticle surface. Analytically, these two parameters are related by the following equation (H. Zhang et al., 2023):

$$\lambda_{LSPR} = \lambda_p\sqrt{2n_s^2 + 1} \qquad \textit{Eq. 2. 1}$$

Here, λ_{LSPR} represents the LSPR peak wavelength, while λ_p denotes the wavelength corresponding to the plasmon frequency of the bulk metal. From Equation (2.1), it can be concluded that the LSPR peak wavelength shows a positive correlation with

the refractive index of the surrounding medium (n_s), which means that a higher n_s results in a higher $\Delta\lambda_{LSPR}$.

2.1.2 Literature review related to LSPR sensors

In the previous section, it was explained that the wavelength investigation mode is widely used in LSPR biosensors. Another commonly employed investigation mode is based on absorbance intensity measurement and intensity ratio. In LSPR sensors utilizing the absorbance intensity measurement mode, the absorbance intensity at the resonance wavelength is recorded at different analyte concentrations.

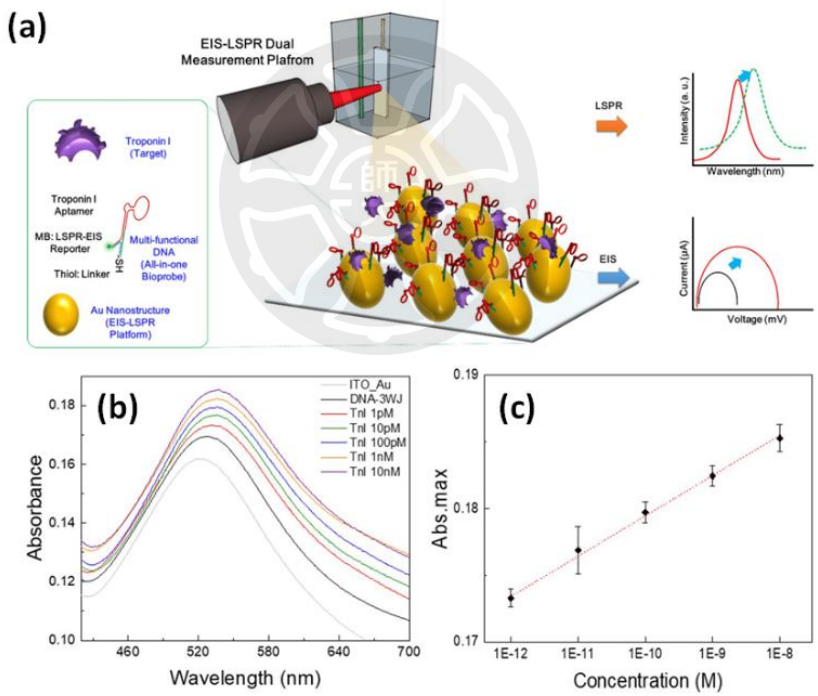

Figure 2. 3 (a) Schematic diagram of dual mode sensor for cardiac troponin I detection (b) Sensor response before and after target presence (b) Linear response of sensor based on changes in peak absorbance at 550 nm wavelength. Figure adapted from Ref. (Lee et al., 2019)*, licensed under CC BY 4.0.*

One of the researchers who used absorbance intensity mode is Lee et al. in 2019 (Lee et al., 2019). The sensor developed was a dual-mode sensor based on

LSPR and EIS, as shown in Figure 2. 3 (a). In this study, an Indium tin oxide (ITO) substrate modified with gold nanoclusters was immobilized with multi-functional DNA 3 way-junction (3WJ)-based bioprobe. This bioprobe consists of several main elements, namely: (1) thiol, which functions to immobilize the probe on the surface of the gold nanocluster; (2) methylene blue (MB), which is used to enhance the plasmonic effect of the nanoparticle; and (3) aptamer at the end of the bio-probe fragment as a recognition element to detect cardiac troponin I. The difference in LSPR signals before and after target detection is shown in Figure 2. 3 (b). Meanwhile, the sensor response to the variation of target concentration is shown in Figure 2. 3 (c), which shows that the absorbance intensity increases with the increase of target concentration. The linear range of this sensor system is in the range of 1 pM to 10 nM.

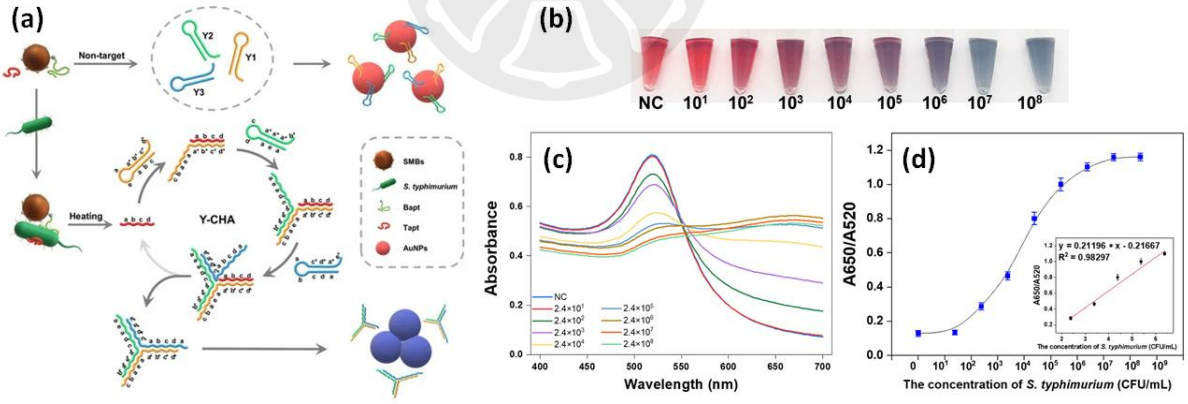

Figure 2. 4 (a) LSPR sensor detection mechanism (b) Color changes in the sample before and after adding the analyte (c) Absorbance profiles of samples with different analyte concentrations (d) Sensor response based on intensity ratio. Figure adapted from Ref. (J. Chen et al., 2015)*, licensed under CC BY 4.0.*

One of the weaknesses of the intensity-based investigation mode is the presence of noise caused by light source fluctuations. To overcome this issue, some researchers use the absorbance ratio-based investigation mode in analyte

quantification. This mode utilizes the absorbance ratio at two wavelengths, as done by Chen et al., who used the absorbance ratio at 520 nm and 650 nm wavelengths (A_{650}/A_{520}) to detect *Salmonella typhimurium* (S. Chen et al., 2021).

In Chen et al.' study, the developed LSPR sensor utilized the catalytic hairpin assembly (CHA) strategy for signal amplification. This amplification is based on the self-assembly and disassembly reaction of nucleic acid hairpins, as shown in Figure 2. 4 (a). The presence of the target triggers the formation of a complex layer consisting of streptavidin magnetic beads (SMBs)-Bapt-*S. typhimurium*-Tapt. Upon heating, Tapt is released and hybridized with the sticky ends of Y1, Y2, and Y3, forming the Y-CHA structure. As a result, the hairpin probe is released from the AuNP surface, so that the AuNPs lose the hairpin protection and aggregate in the salt solution. This causes the color change of the solution from red to blue-gray. The absorbance profile shown in Figure 2. 4 (c) shows that the peak intensity at 520 nm wavelength decreases with increasing concentration of *S. typhimurium*. In contrast, the emergence of a new peak at 650 nm wavelength indicates that the nanoparticles undergo aggregation. By comparing the absorbance intensity at 650 nm and 520 nm wavelengths, the LSPR sensor with this detection strategy has a linear range at a concentration of 10^2 to 10^6 CFU/mL.

In conclusion, to provide a more comprehensive picture of the utilization of LSPR sensors for various detection purposes, we present Table 2. 1. This table summarizes recent publications related to LSPR biosensors by highlighting several key parameters, such as the material on the LSPR chip, the investigation mode used, the analytes detected, the dynamic range, and the LOD. Based on the data

presented, various types of analytes have been successfully detected such as melamine, fipronil and clenbuterol, with one of the commonly used investigation modes is utilizing wavelength shift.

Table 2. 1 LSPR sensor and its investigation mode

Materials	Analytes	Dynamic range	LOD
Investigation mode: Wavelength			
AuNPs/peptide (Yoo et al., 2022)	fipronil	1 ppt - 1 ppm	0.01 ppb
AgNT/ACE2 (Y. Yang et al., 2022)	spike RBD protein	2.03 - 9420 pM	0.83 pM
Au core-satellite (Y. B. Liu et al., 2019)	glutathione	0.1 to 10 μM	0.1 μM
AuNR/aptamer (Jo et al., 2021)	25-hydroxyvitamin D3	0.1–10^5 ng/mL	0.1 ng/mL
AuNR/aptamer (J. H. Park et al., 2017)	ochratoxin A	10 pM - 10 μM	0.56 pM
AuNPs/DNA conjugates (S. Jia et al., 2018)	mercury(II) ion	1 – 50 nM	0.7 nM
Investigation mode: Intensity			
AuNPs/anti-CRP (Oh et al., 2019)	C-reactive protein	0.01–10 μg/mL	0.01μg/mL
AuNPs/MoS_2-NPs (S. Kumar et al., 2021)	Shigella	1 - 10^9 CFU/mL	1.56 CFU/mL
AuNPs/aptamer (Oh et al., 2017)	S. typhimurium	10^4-10^6 cfu/mL	10^4 cfu/mL
AuNPs/GO (N. F. Chiu et al., 2018)	BSA	145 fM - 1.45 nM	145 fM
AuNPs (Chang et al., 2017)	melamine	0 to 0.9 μM	33 nM
AuNPs/cholesterol oxidase (S. Kumar et al., 2019)	cholesterol	10 nM - 1 μM	53.1 nM
Investigation mode: Intensity ratio			
AuNPs/cysteamine (Liang et al., 2011)	melamine	1–200 mg/L	1 mg/L
AuNPs/OTA aptamer (B. Liu et al., 2018)	Ochratoxin A	0.0316–316 ng/mL	0.0316 ng/mL
AuNPs/cysteamine (Kang et al., 2016)	Clenbuterol	-	50 nM
AuNPs/cysteamine (Y. Ma et al., 2013)	melamine	0.08 - 1.6 mM	80 nM

2.1.3 Research Gap and Objectives

Based on the information shown in Table 2. 1, the approach that is widely used in analyte quantification in LSPR biosensors is by using the wavelength shift

investigation mode. From the relationship in Equation (2.1), the LSPR peak wavelength is directly proportional to the refractive index of the medium around the nanoparticle. An increase in the refractive index on the nanoparticle surface results in a redshift of the LSPR peak wavelength.

Although theoretically the refractive index of the sensing medium has a proportional relationship with the shift in the resonance wavelength, several researchers such as Minopoli et al. (Minopoli et al., 2020), and Iarossi et al. (Iarossi et al., 2018) found a decrease in the LSPR sensor response at higher analyte concentrations in their experiments.

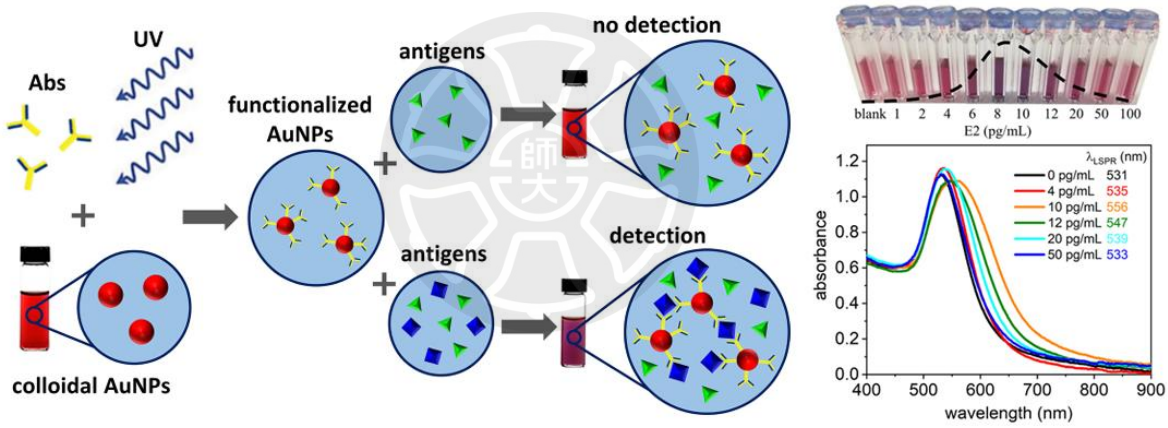

Figure 2. 5 (a). Fabrication of LSPR sensor chip (b). Absorbance spectra of functionalized AuNPs with different 17β estradiol (E2) target concentrations. Figure adapted with permission from Ref. (Minopoli et al., 2020)*, copyright Elsevier.*

Minopoli et al utilized AuNPs with a diameter of 35 nm and functionalized them with polyclonal sheep anti-17β-estradiol IgG antibodies (anti-E2) to bind the 17β estradiol (E2) target (Minopoli et al., 2020). The sensor response to different concentrations of estradiol is shown in Figure 2. 5. The LSPR peak data indicated a redshift in the LSPR peak wavelength as the estradiol concentration increased to 10

pg/mL. However, at higher concentrations of estradiol, the LSPR peak decreased from 556 nm at a concentration of 10 pg/mL to 547 nm at a concentration of 12 pg/mL.

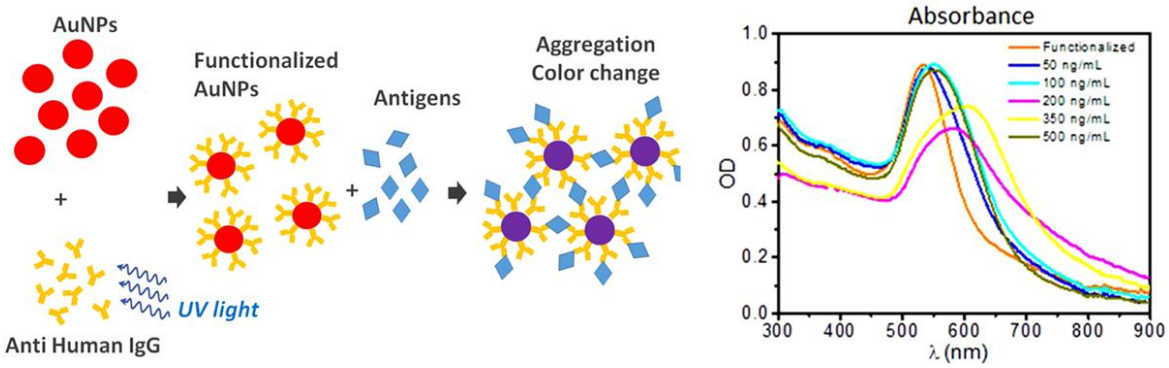

Figure 2. 6 (a). Fabrication of LSPR sensor chip (b). Absorbance spectra of functionalized AuNPs with different human immunoglobulin G target concentrations. Figure adapted from Ref. (Iarossi et al., 2018)*, licensed under CC BY 4.0.*

A similar finding was also found in a study conducted by Iarossi et al in 2018 (Iarossi et al., 2018). In this study, AuNPs with different sizes of around 40 nm were used to detect human immunoglobulin G (IgG). The sensor system developed is shown in Figure 2. 6. Initially, AuNPs were functionalized with 50 µg/mL antihuman IgG to recognize the target, and 1 mg/mL BSA was added to the functional colloid to block the AuNP surface from nonspecific adsorption. Based on the LSPR peak data, the absorption peak red-shifted with increasing concentration until it reached a maximum at 350 ng/mL. However, at a higher concentration of 500 ng/mL, the LSPR peak exhibited a blueshift to a shorter wavelength.

In addition to the two studies mentioned above, LSPR signals with similar characteristics have also been reported by Kasetner et al. (Kastner et al., 2022), Gao et al. (Gao et al., 2019), Chen et al. (W. Chen et al., 2020), Ma et al. (Z. Ma et al., 2022), and Cavalera et al (Cavalera et al., 2022). This phenomenon is known as the Hook effect, where the concentration that causes the maximum redshift is referred to

as the Hook point. It should be noted that all the studies related to LSPR sensors cited in the previous paragraph were conducted from an experimental perspective. To gain a deeper understanding of the interaction phenomena in LSPR sensors, such as the size changes due to increasing target size, computational approaches are crucial. These approaches can provide insights often unavailable through experimental methods, including detailed electromagnetic field distributions due to the presence of additional materials on the nanoparticle surface. A thorough understanding of these interaction phenomena is essential before sensors can be used to detect more complex targets and environments.

Based on this context, the purpose of this study was to investigate the interaction studies of the LSPR sensor through experimental and computational approaches. From the experimental side, the sensor system used consisted of AuNP as an optical transducer, which was modified with anti-BSA antibody to specifically recognize the target protein BSA. The LSPR sensor studied belongs to the category of solution-phase colloidal nanoparticles, as classified by Kim et al (D. M. Kim et al., 2021). BSA was selected as the model protein due to its widespread use in biosensor research, particularly in early-stage studies to evaluate interaction mechanisms. Its stable structure under various conditions, high commercial purity, and relatively low cost make it an ideal candidate for fundamental investigation prior to applications involving more complex targets or clinical biomarkers (Bhakta et al., 2015).

Literature has reported that the Hook effect (a nonlinear optical response) has been observed in colloidal AuNP-based LSPR systems with nanoparticle sizes around 35–40 nm. In contrast, this study uses smaller 15 nm AuNPs, which offer

absorption-dominated optical signals rather than scattering (Jain et al., 2006), making them well-suited for absorbance-based detection systems as employed here. From the computational side, the FDTD approach was used to model the sensor system, by representing the antibody and antigen as a dielectric layer around the AuNP surface. The analysis focused on the optical characteristics, including scattering, absorption, and extinction cross sections, as well as the electric field distribution around the nanoparticles.

2.2 Research Methodology

2.2.1 Synthesis of AuNPs and their functionalization

To determine the characteristics of the LSPR signal, AuNPs have been fabricated using a chemical reduction method. In simple terms, the experimental steps to synthesize AuNPs are shown in Figure 2. 7 (a). The synthesis of nanoparticles began by preparing two solutions: 0.01969 g of Hydrogen tetrachloroaurate (III) trihydrate ($HAuCl_4 \cdot 3H_2O$), ACS, 99.99% (metal basis) was dissolved in 50 mL of deionized water to obtain a 1 mM solution, while 0.0575 g of Sodium citrate dihydrate ($C_6H_9Na_3O_9$) was dissolved in 5 mL of deionized water to create a 38.8 mM solution.

The $HAuCl_4 \cdot 3H_2O$ solution was then heated to boiling using a magnetic stirrer set to 550°C. Once boiling, the temperature was reduced to 405°C, and a magnetic stir bar was activated at a speed of 1150 rpm. The $C_6H_9Na_3O_9$ solution was subsequently added to a three-necked flask and maintained at an elevated temperature for 10 min. During this process, AuNPs were naturally formed, as indicated by a visible color

change from pale yellow to red. At this stage, the following chemical reactions took place:

$$HAuCl_4 + C_6H_9Na_3O_9 \xrightarrow{\Delta} Au + CO_2 + HCl + NaCl \qquad \text{Eq. 2. 2}$$

After the nanoparticles were successfully fabricated, the heater on the magnetic stirrer was turned off and the solution was left to cool to room temperature. After that, membrane filter paper with a pore size of 0.45 µm was used to filter the solution so that the nanoparticles obtained had a more uniform size. After the solution was put into a bottle, the AuNPs were stored in a refrigerator at 4°C before further use.

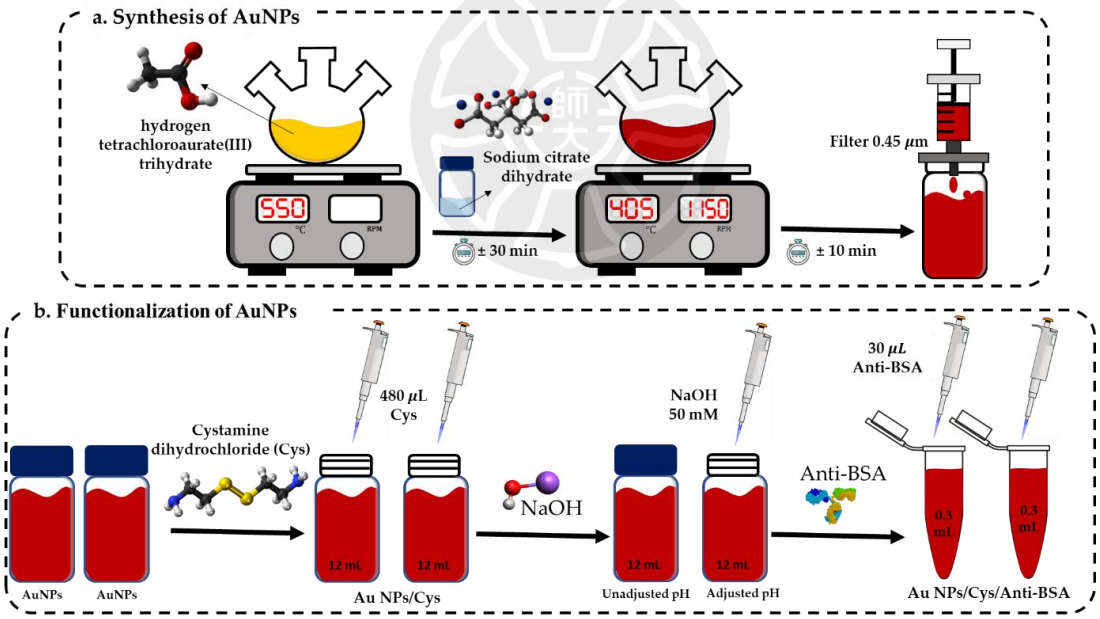

Figure 2. 7 Illustration related to the (a) AuNPs fabrication process and (b) its surface modification. Figure adapted with permission from Ref. (Nurrohman & Chiu, 2023)*, copyright IEEE.*

The immunosensor developed in this study was used to detect BSA. Therefore, anti-BSA was used as the molecular recognition element and this

material was immobilized on the surface of AuNPs by utilizing Cystamine dihydrochloride (Cys, 98%) as its linker. All the experimental steps in this section are shown in Figure 2. 7 (b). A solution of 480 µL Cys dissolved in deionized water was combined with 12 mL of AuNPs, gently mixed, and allowed to react for 2 hours at room temperature. The surface of the nanoparticles will be covered by Cys due to the ligand exchange and the sample with this condition is called Au/Cys.

In this experiment, anti-BSA immobilization was performed under two conditions: one with pH adjustment using NaOH, and the other without any pH adjustment. One of the factors that affect the refractive index is temperature (Nisar et al., 2020). Therefore, to reduce errors caused by temperature fluctuations, all samples to be functionalized with anti-BSA and used to detect BSA were placed in a dry bath incubator with a controlled temperature of 25°C. To ensure that the sample temperature has been successfully conditioned, the AuNPs/Cys sample was left in the incubator for 30 min and then mixed with 30 µL of anti-BSA. Absorbance measurements were carried out after 15 min and the success of the functionalization process was indicated by a shift in the LSPR wavelength. To simplify, AuNPs that have been functionalized are called AuNPs/Cys/Anti-BSA.

2.2.2 Equations used and FDTD simulation settings

The LSPR signal in this study was characterized using a dual-beam UV-Vis spectrophotometer (U-2900, Hitachi High-Technologies Corporation, Tokyo, Japan). The obtained LSPR signal reflects the absorbance dependence of the sample across different wavelengths. Theoretically, absorbance (A) at varying nanoparticle concentrations (c_m) follows the Beer-Lambert equation, as shown below:

$$A = c_m \bar{e} L \quad \text{Eq. 2. 3}$$

Where $\bar{e}$ represents the molar extinction coefficient (in m^2 mol^{-1} in SI units, typically expressed as cm^{-1} mol^{-1} and L denotes the path length (in m), which is usually 1 cm in most experimental setups. The molar extinction coefficient is also related to the extinction cross-section (σ_{ext}), with the two quantities connected by the following equation:

$$\bar{e} = \frac{N \sigma_{ext}}{\ln 10} \quad \text{Eq. 2. 4}$$

Where N denotes Avogadro's number (≈ 6.022 x 10^{23} particle/mol).

In Equation (2.4) above, extinction cross-section is a factor influenced by wavelength. This quantity is related to both scattering cross section (σ_{scat}) and absorption cross section (σ_{abs}) through the following relationship (Cheng et al., 2020):

$$\sigma_{ext}(\omega) = \sigma_{abs}(\omega) + \sigma_{scat}(\omega) \quad \text{Eq. 2. 5}$$

For molecules, scattering cross section is minimal in comparison to absorption cross section. As a result, extinction is essentially equal to absorption ($\sigma_{ext} \approx \sigma_{abs}$). This is why UV-Vis spectroscopy is commonly referred to as absorption spectroscopy, even though it would be more accurate to call it extinction spectroscopy.

To investigate the optical properties of the nanoparticles studied, the FDTD method was chosen for the computational simulations, with the setup briefly depicted in Figure 2. 8. In this study, the simulation was conducted in 3D mode, with the nanoparticle area enclosed by a Perfectly Matched Layer (PML) boundary on all axes. A Total Field Scattered Field (TFSF) source was selected as the light source,

and monitors were placed both inside and outside the TFSF region to calculate the absorption and scattering cross-sections.

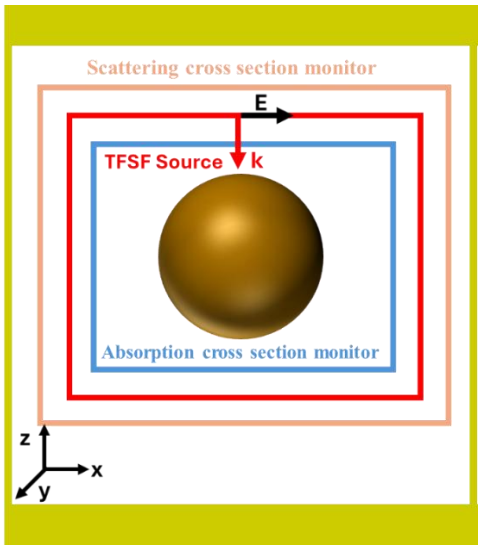

Figure 2. 8 FDTD simulation setup is depicted schematically.

2.3 Results and Discussion

2.3.1 LSPR signal quality at different AuNPs concentrations

After AuNPs were successfully fabricated, several characterizations were performed to determine the size and morphology of the nanoparticles. The size of AuNPs can be estimated based on the position of the LSPR peak. From the UV-Vis spectra shown in Figure 2. 9 (a), the LSPR peak was detected at a wavelength of ~520 nm for five different concentrations of AuNPs, indicating that the solution was dominated by AuNPs with a size of around ~15 nm, as supported by related references (N. F. Chiu et al., 2018). To verify this estimation, characterization was performed using Transmission Electron Microscopy (TEM) and zeta potential. The characterization results are shown in Figure A1 in Appendix A. The TEM image shows that AuNPs have an almost spherical shape with an average size of around ~15 nm. Meanwhile,

the results of the zeta potential measurement showed a particle size distribution of 16.05 ± 4.94 nm, which is still within a consistent range with a size of 15 nm.

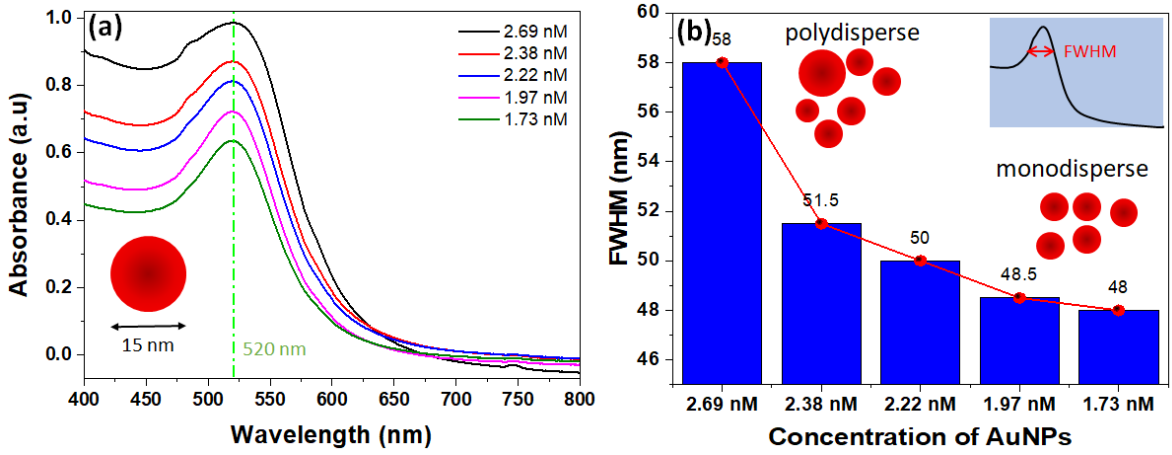

Figure 2. 9 (a) UV-Vis spectra illustrating the absorbance profiles and (b) FWHM of AuNPs at varying concentrations. Figure adapted with permission from Ref. (Nurrohman & Chiu, 2023)*, copyright IEEE.*

After the AuNP size is known, the analysis is continued by evaluating the effect of AuNP concentration variations on the FWHM value of the LSPR signal. The FWHM parameter plays an important role in determining signal quality, where a smaller FWHM value indicates a sharper resonance peak and better sensor quality. FWHM also contributes to the Figure of Merit (FoM) value, which is mathematically expressed as follows (Farooq et al., 2022):

$$FoM = \frac{S}{FWHM} \qquad \text{Eq. 2. 6}$$

where S represents the sensor sensitivity. In this analysis, the FWHM value is determined based on the procedure described in the following reference (Orbaek et al., 2015).

Figure 2. 9 (a) presents the absorbance spectra of five different concentrations of AuNPs. As the concentration decreases, a reduction in absorbance intensity is

observed. Further analysis of the FWHM for each concentration is shown in Figure 2. 9 (b). The data indicate that lower concentrations of AuNPs result in narrower FWHM values in the absorbance spectra. A narrower FWHM is associated with a higher FoM, as it reflects improved signal sharpness and thus better sensor accuracy. Moreover, the FWHM of the absorbance spectrum provides insight into the dispersibility and size distribution of nanoparticles in solutions. A smaller FWHM suggests a more uniform particle size, indicating a monodisperse suspension (Oliveira et al., 2020)(Dheyab et al., 2022). Based on these results, the lowest concentration tested in this study demonstrates the best dispersibility characteristics among the five. Therefore, this concentration was selected for subsequent steps involving surface functionalization and BSA detection.

2.3.2 Immobilization Steps of Cys Linker on AuNPs Surface

In this study, anti-BSA was used as a ligand to recognize BSA. To immobilize anti-BSA on the surface of AuNPs, we used a Cys linker. AuNPs are very susceptible to aggregate when Cys is added due to the ligand exchange phenomenon. Too high Cys concentration will make the LSPR peak difficult to identify. Therefore, we consider the aggregation level in the AuNPs surface modification process and based on the following references (C. H. Lu et al., 2012), the aggregation level can be assessed based on the ratio of the absorbance intensity at 650 nm and 520 nm wavelengths (A_{650}/A_{520}).

There are 4 different concentrations of Cys used in the AuNPs surface modification process and the volume of Cys added to the AuNPs solution has a

volume ratio of 1:100 (10 µL Cys and 1000 µL AuNPs). From the data shown in Figure 2. 10 (a), the LSPR peak decreased significantly after Cys was added. If the aggregation level is calculated, AuNPs functionalized with 10 µM Cys have a smaller aggregation level compared to the other 3 concentrations (Figure 2. 10(b)). However, the LSPR peak did not shift significantly at Cys concentration of 10 µM. Therefore, we performed optimization at the same Cys concentration but with a higher volume ratio of 1:50 (1000 µL AuNPs : 20 µL Cys) and 1:25 (1000 µL AuNPs : 40 µL Cys).

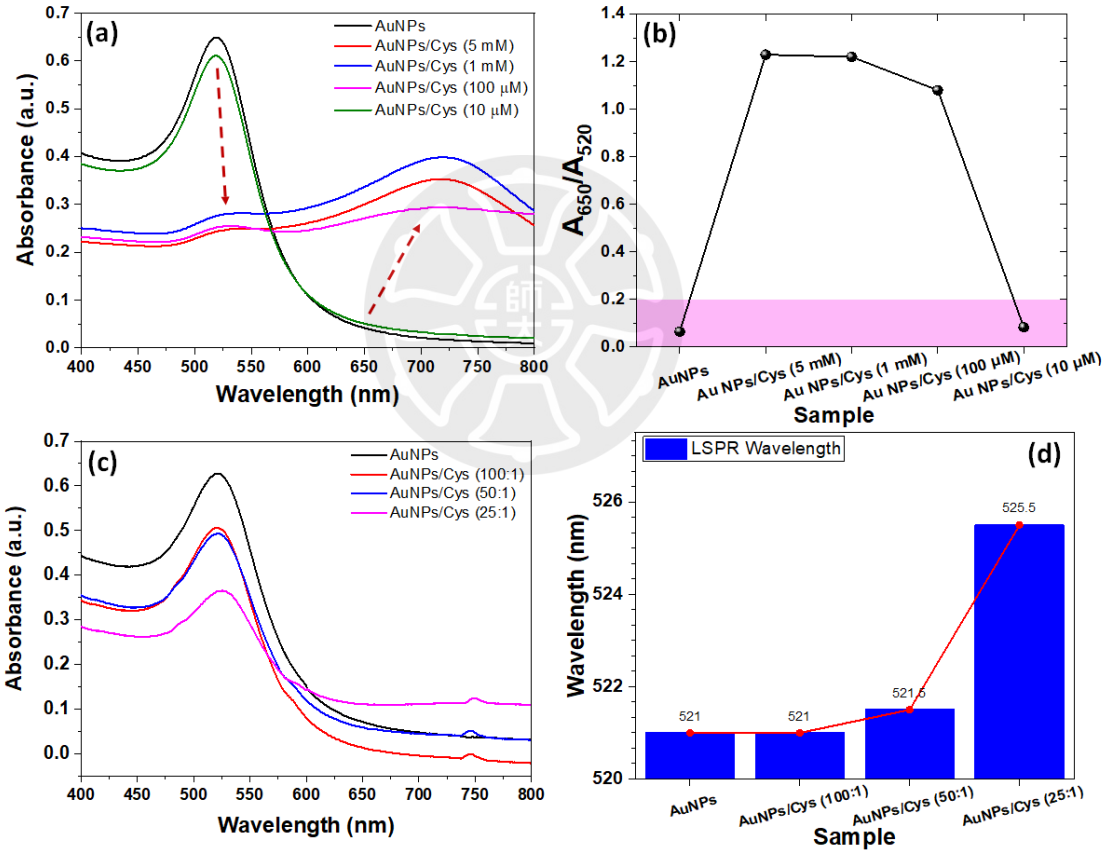

Figure 2. 10 (a) UV-Vis spectra and (b) aggregation level of AuNPs with varying Cys concentrations. (c) UV-Vis spectra and (d) LSPR peak of AuNPs/Cys10 µM at varying volume ratios. Figure adapted with permission from Ref. (Nurrohman & Chiu, 2023)*, copyright IEEE.*

The absorbance spectra of AuNPs with different Cys volume ratios are presented in Figure 2. 10 (c), and the corresponding LSPR peak positions are shown

in Figure 2. 10 (d). The data reveals that the LSPR peak began to shift when the volume ratio reached 1:50, with the most significant shift occurring at a 1:25 ratio. Since the amount of anti-BSA that can be immobilized is closely related to the number of linkers on the nanoparticle surface, a 10 μM Cys concentration and a 1:25 volume ratio was selected for further investigation.

2.3.3 Aggregation phenomenon based on computational prospective.

To evaluate the phenomenon of nanoparticle aggregation computationally, simulations of extinction and scattering cross sections were performed using the FDTD method. Two scenarios were analyzed: unaggregated and aggregated conditions. In unaggregated conditions, the optical properties of nanoparticles are assumed to be unaffected by the presence of other nanoparticles around them. Therefore, the most representative model for this scenario is a single isolated nanoparticle.

In contrast, in the aggregated condition, the optical properties of nanoparticles are significantly affected by the electromagnetic field of neighboring nanoparticles, leading to plasmonic coupling between particles. In this research, aggregation occurred during the surface modification process of AuNPs using Cys linkers. At this stage, the citrate ligand that initially stabilized the nanoparticle surface was replaced by Cys linkers, which is known to trigger aggregation through decreasing colloidal stability and potential bridging between particles.

Based on the results reported by Park and Parry, the thickness of the citrate layer from the TEM image was around 0.8–1 nm (J.-W. Park & Shumaker-Parry,

2014). Meanwhile, Shukri et al. reported that the thickness of the cystamine layer on the AuNPs surface is in the range of 1 nm (Shukri et al., 2016). Therefore, the minimum distance between nanoparticles in the aggregation state is estimated to be around 2 nm. Considering these physical conditions and to capture the relevant plasmonic coupling regime, the range of interparticle distances in this simulation is set to 0 - 6 nm. This range is considered to be able to represent realistic variations that can occur during the surface functionalization process of nanoparticles.

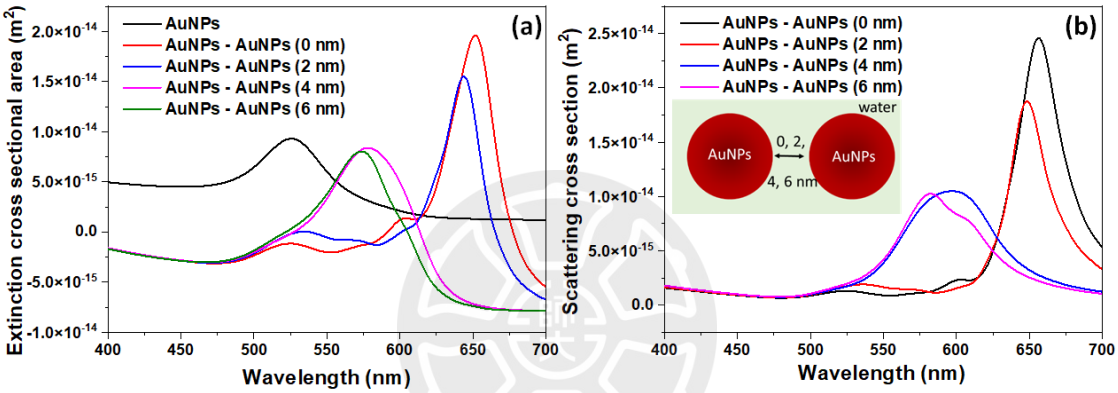

Figure 2. 11 (a) σ_{ext} spectra of single and dimer AuNPs. (b) σ_{scat} spectra of AuNP dimers at varying interparticle distances. Figure adapted with permission from Ref. (Nurrohman & Chiu, 2023)*, copyright IEEE.*

The extinction cross-section spectrum shown in Figure 2. 11 (a) reveals that the LSPR peak for a single AuNP occurs at a wavelength of 521 nm. This is consistent with the experimental results, where the LSPR peak for nanoparticles of 15 nm in size is observed at a wavelength of 520 nm. The slight difference between the experimental and simulated results is likely due to the non-uniform size distribution of the nanoparticles, as well as variations in the refractive index of the AuNPs used in the simulation compared to the actual refractive index.

The computational simulation results show that increasing the number of nanoparticles significantly affects the extinction cross-section spectrum. When two

nanoparticles are simulated, there is a shift in the peak position that is sensitive to the distance between the particles. At a distance between particles of 6 nm, the peak position shifts from 521 nm (for a single nanoparticle) to 573 nm. The smaller the distance between the nanoparticles, the peak shift towards a higher wavelength (red shift) becomes more obvious. This shift is also accompanied by an increase in spectral intensity. Of the four simulated distances, the configuration of two nanoparticles in contact with each other produces a peak at the highest wavelength and maximum intensity, indicating the strongest plasmonic coupling in the system.

The same characteristics are also shown by scattering cross section spectra data. The scattering wavelength peak shifts to a higher wavelength and is followed by its intensity. Nanoparticle aggregation is a process in which nanoparticles interact with each other and combine into groups or clusters, either permanently or temporarily. The computational results reveal that, in the aggregated state, the scattering effect becomes significantly more dominant, leading to the emergence of new peaks at higher wavelengths. This finding highlights the impact of nanoparticle aggregation on optical properties, particularly the scattering behavior.

2.3.4 Optical properties of nanoparticles after functionalization

After the AuNPs surface was modified using Cys, sensor functionalization was carried out by adding 30 µL of anti-BSA with a concentration of 100 µg/mL into AuNPs/Cys solution. The amine group in Cys will bind to the carboxyl group in the antibody. The reaction time required in this stage is 15 min. We display the

absorbance spectra at all stages starting from the modification of the AuNPs surface with Cys to functionalization using anti-BSA in Figure 2. 12 .

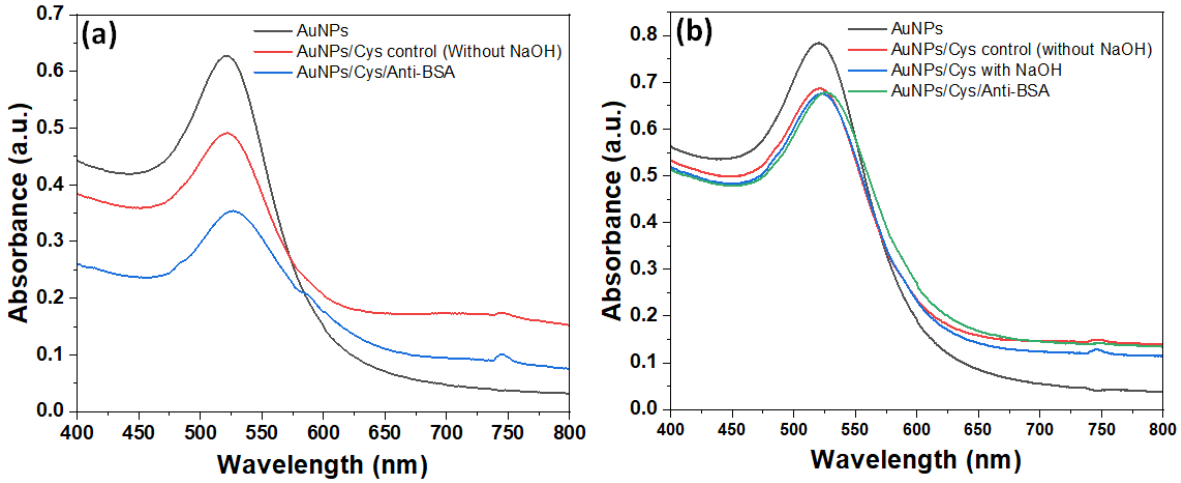

Figure 2. 12 UV-Vis spectra during functionalization process with anti-BSA: (a) without and (b) with NaOH addition. Figure adapted with permission from Ref. (Nurrohman & Chiu, 2023)*, copyright IEEE.*

For sensor functionalization carried out using the original pH (around ~6), the LSPR peak has been identified to shift to a higher wavelength due to the bigger size of the nanoparticles. The LSPR wavelengths for AuNPs, AuNPs/Cys, and AuNPs/Cys/anti-BSA were 521 nm, 522 nm, and 526.5 nm, respectively. When calculating the aggregation levels for the three samples, the values obtained were 0.113 for AuNPs, 0.353 for AuNPs/Cys, and 0.318 for AuNPs/Cys/anti-BSA. Experimental data show that the addition of anti-BSA reduces the aggregation level of the nanoparticles. The absorbance intensity at a wavelength of 650 nm decreases compared to the AuNPs/Cys spectra and this indicates better dispersibility of the nanoparticles (J. Zhang et al., 2012).

To explore the effect of pH on the quality of LSPR signals during the nanoparticle functionalization process, we performed pH adjustments on the AuNPs/Cys sample. Initially, the pH of the sample was at a neutral value of around pH 6. The pH was decreased by adding different volume of 0.5 mM HCl, which decreased the pH to pH ~2. Conversely, the pH was increased by adding 50 mM NaOH solution in different volumes, so that the pH of the sample increased to pH ~12.

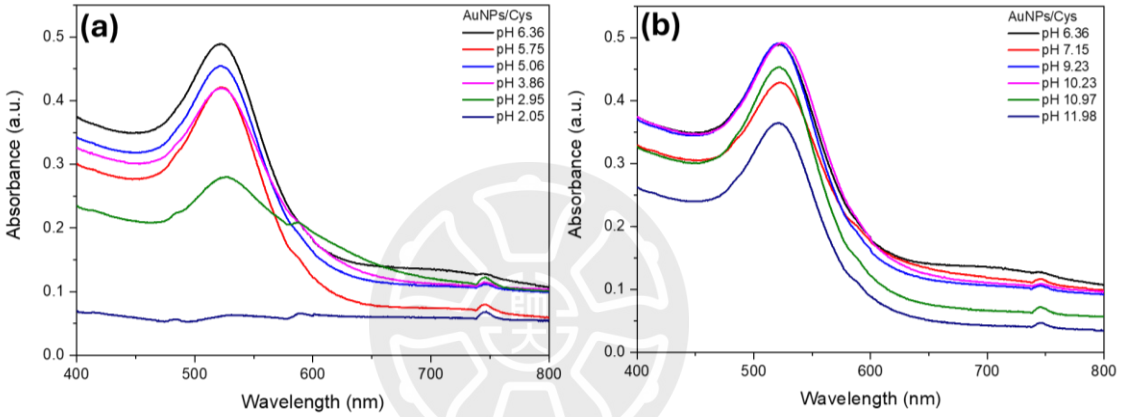

Figure 2. 13 Absorbance spectra of AuNPs/Cys samples (a) when pH is lowered with 0.5 mM HCl (b) when pH is increased with 50 mM NaOH.

The measurement results shown in Figure 2. 13 indicate that the sample with pH 9 - 10 showed the lowest nanoparticle aggregation, and the most stable LSPR signal quality compared to other pHs. Based on these results, a comparison was made between functionalization at the original pH and the increased pH. The addition of 20 µL of NaOH (50 mM) to the sample resulted in an increase in pH to 8.97.

From the experimental results shown in Figure 2. 12 (b), it can be seen that the peak absorbance intensity of the AuNPs/Cys sample that had been added with anti-BSA increased significantly, even exceeding the peak intensity of AuNPs/Cys

after the addition of NaOH. The peak absorbance value of the LSPR increased from 0.676 (before the addition of anti-BSA) to 0.678 (after the addition of anti-BSA), indicating that the slightly alkaline pH conditions contributed to the increase in nanoparticle stability. In addition, the FWHM parameter also showed improvement. For the AuNPs/Cys/anti-BSA sample without the addition of NaOH, the FWHM was recorded at 57 nm. After the addition of NaOH, the FWHM value decreased to 53 nm. This decrease in FWHM indicates an increase in the uniformity and dispersibility of the nanoparticles, which has implications for increasing the FoM and sensor accuracy. Thus, the treatment of increasing pH using NaOH not only improves the quality of the LSPR signal but also improves the overall performance of the AuNPs-based sensor.

2.3.5 Electric field profile due to the presence of a dielectric layer

After sensor functionalization, we explored the effect of the dielectric layer on the AuNPs surface on the electric field distribution using a computational approach. The resulting structure is assumed to be a core/shell configuration, where AuNPs act as the core, while Cys and anti-BSA form the first and second dielectric layers, respectively. For ease of reference, the dielectric layer formed by Cys will be called L_1, while the layer formed by anti-BSA will be called L_2. Regarding the refractive index of the dielectric layer, the refractive index of L_1 is 1.5 and L_2 is 1.6 and these values are based on the following references (Krivosudský et al., 2017).

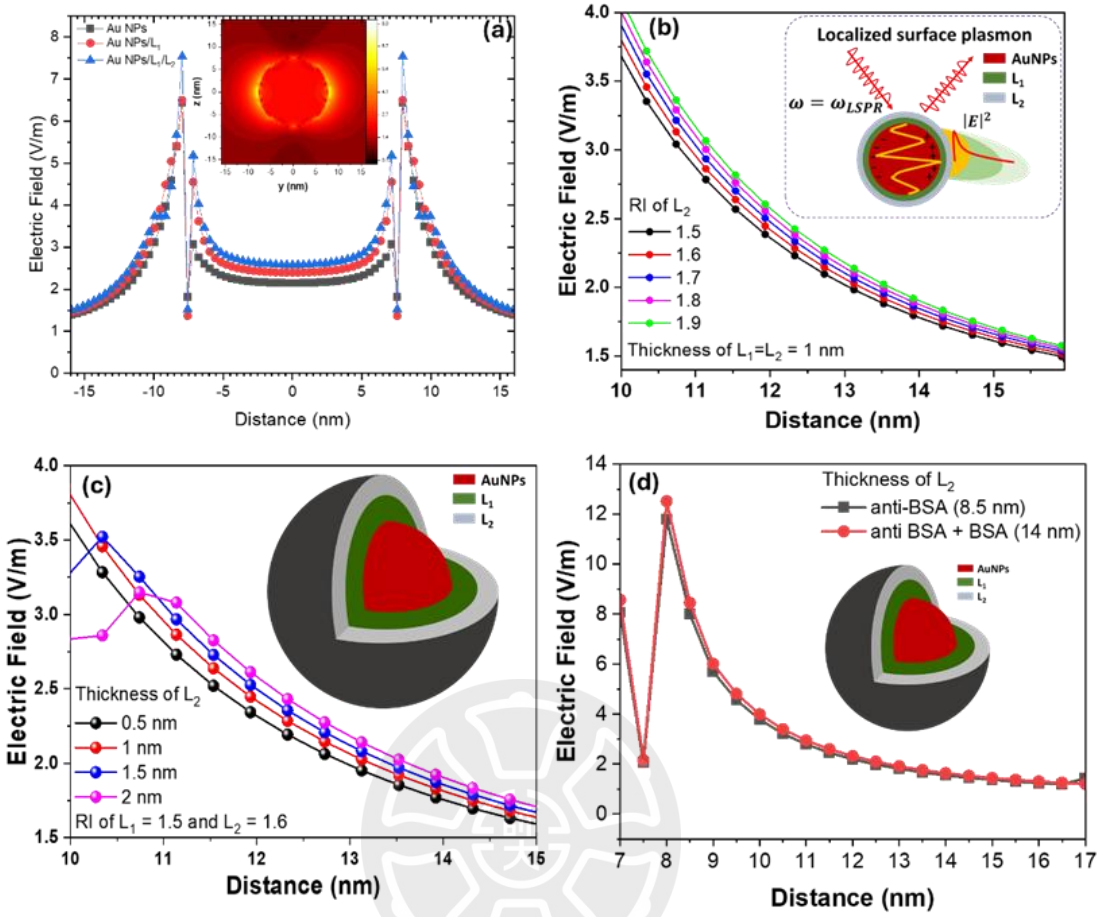

Figure 2. 14 (a) Electric field profiles for bare AuNPs, Au with dielectric layer L_1 (AuNPs/L_1) and Au with dielectric layers L_1 and L_2 (AuNPs/L_1/L_2). Changes in the electric field due to variations in (b) refractive index and (c) thickness of L_2. (d) Electric field on the surface of AuNPs caused by the presence of anti-BSA and BSA. Figure adapted with permission from Ref. (Nurrohman & Chiu, 2023)*, copyright IEEE.*

To investigate the effect of dielectric layers L_1 and L_2 on the electric field distribution, three nanoparticle structures were analyzed: bare AuNPs, AuNPs coated with a single dielectric layer (L_1), and AuNPs with two dielectric layers (L_1 and L_2). The thickness of each dielectric layer was assumed to be 1 nm. The electric field distribution for the bare AuNPs is presented in the inset of Figure 2. 14 (a), while the comparison of field distributions for all three structures in along z = 0 is shown in the main panel of Figure 2. 14 (a). All electric field data were obtained at the respective LSPR wavelengths: 521 nm for bare AuNPs, 525 nm for AuNPs/L_1, and 527 nm for

AuNPs/L_1/L_2. When comparing the electric field magnitudes across the three structures, the presence of L_1 and L_2 clearly enhances the electric field surrounding the nanoparticles. This enhancement is most prominent at the nanoparticle surface, approximately ±7.5 nm from the center. At this radial distance, the electric field intensities are 2.15 V/m for bare AuNPs, 2.39 V/m for AuNPs/L_1, and 2.58 V/m for AuNPs/L_1/L_2.

The change of LSPR signal is mainly caused by the interaction at the sensing surface that changes both the refractive index and the thickness of the surrounding layer. Therefore, in this study we investigated the effect of the variation of refractive index and the thickness of the second dielectric layer (L_2) on the electric field distribution around AuNPs. The simulation results are shown in Figure 2. 14, where the effect of the change of refractive index L_2 is shown in panel (b), while the effect of L_2 thickness is shown in panel (c). From these results, it can be concluded that both the increase of refractive index and L_2 thickness lead to a more significant increase in the electric field intensity around the nanoparticles. To approach the experimental conditions, we also evaluated the thickness of the dielectric layer based on the molecular dimensions of anti-BSA and BSA. The first layer (L_1) represents the Cys layer, with a thickness of about 1 nm (Shukri et al., 2016). Meanwhile, the thickness of the anti-BSA and BSA layers are assumed to be 8.5 nm and 5.5 nm, respectively, referring to the Dynamic Light Scattering (DLS) characterization data available in the literature (Hampitak et al., 2020)(Waghmare et al., 2018). The impact of the presence of anti-BSA and BSA layers on the electric field distribution is presented in Figure 2. 14 (d). The results of this simulation show a trend that is

consistent with the results in Figure 2. 14 (a), namely that increasing the thickness of the dielectric layer around the AuNPs significantly strengthens the local electric field intensity at the nanoparticle surface.

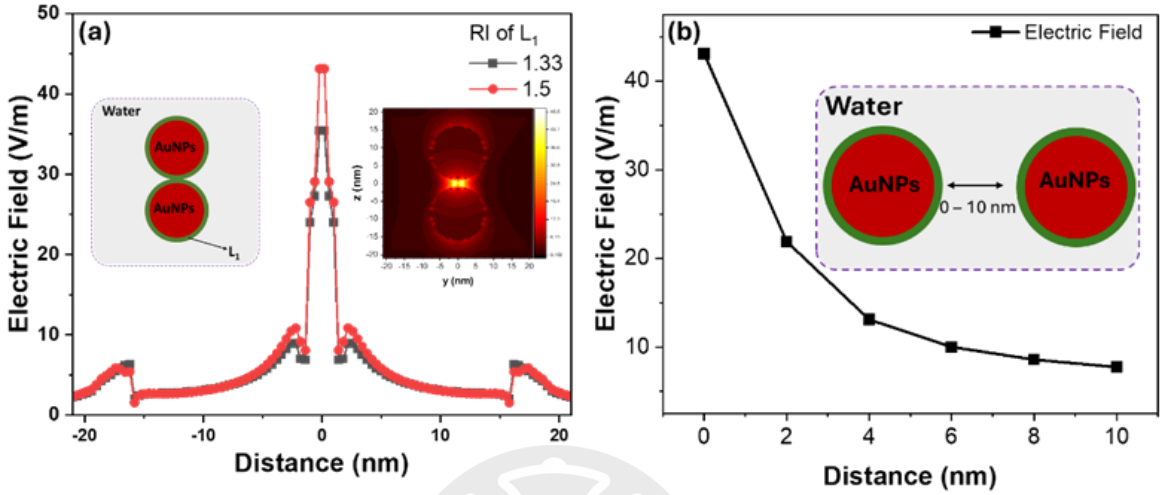

Figure 2. 15 (a). Electric field distribution for dimer nanoparticles (AuNPs/L_1) with two different refractive indices of L_1 (b). Dependence of the maximum electric field between two nanoparticles on varying interparticle distances. Figure adapted with permission from Ref. (Nurrohman & Chiu, 2023)*, copyright IEEE.*

To strengthen the previous findings, simulations were carried out on pairs of nanoparticles forming an aggregate structure (dimer). Figure 2. 15 (a) shows the electric field distribution in the dimer structure, both with and without the presence of the L_1 dielectric layer. In this simulation, the nanoparticles without a dielectric layer are modeled as AuNPs located in a homogeneous medium with a refractive index of 1.33. Compared with the single AuNP configuration, the dimer structure shows a significant increase in electric field intensity, especially in the gap region between the two nanoparticles. The simulation results show that the maximum electric field in this aggregate structure can reach up to 17 times greater than the electric field generated by a single nanoparticle. When the refractive index of L_1 layer is increased from 1.33 to 1.5, the electric field intensity increases further, reaching up to 20 times compared

to the single AuNP case. This indicates that the presence of a dielectric layer with a high refractive index enhances the electric field strengthening effect.

Furthermore, Figure 2. 15 (b) shows the electric field distribution for the dimer structure with varying distance between nanoparticles. The simulation results show that the smaller the distance between particles, the higher the electric field intensity formed between them. This phenomenon indicates a strong plasmonic coupling effect when the nanoparticles are in very close proximity. In contrast, this effect decreases significantly as the distance between nanoparticles increases, indicating that the plasmonic interaction becomes weak at larger distances.

FDTD-based simulations performed show that the electric field around nanoparticles is strongly influenced by the presence of a dielectric layer such as antibodies or antigens. As the refractive index of the dielectric layer increases and its thickness increases, the electric field intensity also increases significantly at the AuNPs surface. However, this increase has a limit, because the evanescent field has a limited penetration depth, usually only a few tens of nanometers. If the target layer is too thick, part of the target is no longer within the field range, causing field saturation, where the addition of layers no longer produces a significant spectral response.

In addition, simulations of two AuNPs show that the interparticle distance plays an important role in determining the strength of the plasmonic coupling. When the two particles are at an optimal distance, the electric field between them is strengthened. However, if the distance is greater, for example due to steric repulsion from excess targets such as antibodies, this coupling weakens, causing the redshift

to become non-linear, even decreasing. This pattern is consistent with what is known as the Hook effect, where the relationship between the interparticle distance and the wavelength shift experiences non-linearity due to field limitations and optical distributions.

2.3.6 Detection of BSA at Varying Concentrations and Selectivity Assessment

Given that pH-adjusted AuNPs produced better signal quality, these nanoparticles were employed to detect BSA within a concentration range of 1 ng/mL to 100 μg/mL. A total volume of 30 μL BSA solution was added to the AuNPs/Cys/anti-BSA mixture. As shown in Figure 2. 16 (a), the LSPR peak gradually redshifted with increasing BSA concentration from 1 ng/mL to 10 μg/mL, shifting from 524.5 nm to 530.83 nm. This observation indicates that the LSPR sensor is highly sensitive to changes in the local environment near the nanoparticle surface within this concentration range. However, an anomalous response was observed at a BSA concentration of 100 μg/mL, where the LSPR peak decreased to 526.17 nm, indicating a non-linear sensor behavior at high antigen concentrations.

This decrease can be explained from some perspectives. Simulation results previously demonstrated that increasing the thickness and refractive index of the dielectric layer surrounding the AuNPs enhances the local electric field. Therefore, higher BSA concentrations are expected to form thicker dielectric layers due to the accumulation of antigen molecules. However, at very high concentrations, BSA may not fully bind to the anti-BSA on the AuNP surface and instead remain freely dispersed in the surrounding medium. This can broaden the penetration depth of the

electric field, causing the sensor to detect both bound and unbound molecules, a phenomenon referred to as bulk sensitivity.

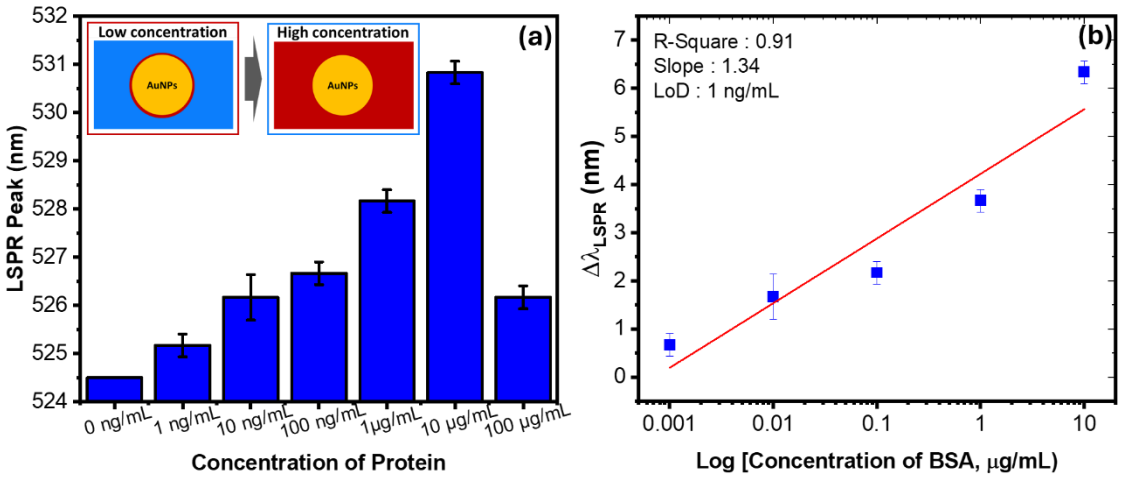

Figure 2. 16 (a) Sensor response at different BSA concentrations. (b) Sensor linearity over a concentration range up to 10 μg/mL. Figure adapted with permission from Ref. (Nurrohman & Chiu, 2023)*, copyright IEEE.*

Additionally, the reduction in the LSPR signal at high BSA concentrations may also be explained by changes in the distance between nanoparticles, which directly affect plasmonic coupling. Simulation results have shown that the strongest enhancement of the electric field occurs when nanoparticles are positioned very close to each other. At higher BSA concentrations, steric hindrance caused by the accumulation of large antigen molecules can prevent nanoparticles from approaching each other closely or can disrupt their optimal aggregation (Minopoli et al., 2020). As a result, the plasmonic coupling effect is weakened, leading to a decrease in local electric field intensity and, consequently, a lower sensor response.

To further illustrate this phenomenon, the inset of Figure 2. 16 (a) depicts the penetration depth of the electric field. When the sensor responds only to target molecules bound to the AuNP surface (represented by the red layer), it exhibits

surface sensitivity, which is an ideal condition where the signal originates exclusively from specific binding events (J. Li et al., 2015). In contrast, when the electric field penetrates deeper into the surrounding medium and captures signals from freely dispersed molecules, the sensor is operating under bulk sensitivity (Wangüemert-Pérez et al., 2019). In complex biological samples, excessive bulk sensitivity can reduce selectivity and produce signals that do not accurately represent specific antigen and antibody interactions.

The observed decrease in the LSPR peak at very high BSA concentrations is also consistent with the well-known Hook effect (Cavalera et al., 2022). This phenomenon occurs when antigen levels exceed the antibody binding capacity, resulting in non-specific binding, aggregate formation, or surface saturation that interferes with accurate detection. In this study, the Hook point was identified at a BSA concentration of approximately 10 μg/mL. Overall, the diminished sensor response at 100 μg/mL is not indicative of poor sensor performance but rather reflects the limitations of the LSPR-based sensing system in conditions of excessive field penetration, antigen excess, and surface saturation. The Hook point marks the upper threshold of effective sensor performance and should be carefully considered in the quantitative application of nanoparticle-based biosensors.

In addition to being used to detect the main target, namely BSA, the sensor was also tested against two non-target proteins, namely cytokeratin 19 (CK19, NBP2-23164, Novus Biologicals, USA) and pregnancy-associated plasma protein A2 (PAPPA2, APREST73992, Sigma-Aldrich, USA). All three samples were tested at

the same concentration, namely 100 ng/mL, using AuNPs-based sensor that had been functionalized with Cys and anti-BSA antibodies.

The measurement results shown in Figure 2. 17 show that exposure to BSA resulted in a significant shift in the LSPR peak of ~3.67 nm, indicating a specific interaction between BSA and antibodies immobilized on the sensor surface. In contrast, the sensor response to CK19 and PAPP-A2 was very low, only ~0.5 nm and ~0.67 nm, respectively. These results indicate that the interaction between the sensor and the two non-target antigens is very weak or does not occur, thus proving that the sensor has high selectivity towards BSA and is able to avoid false signals due to the presence of other interfering biomarkers.

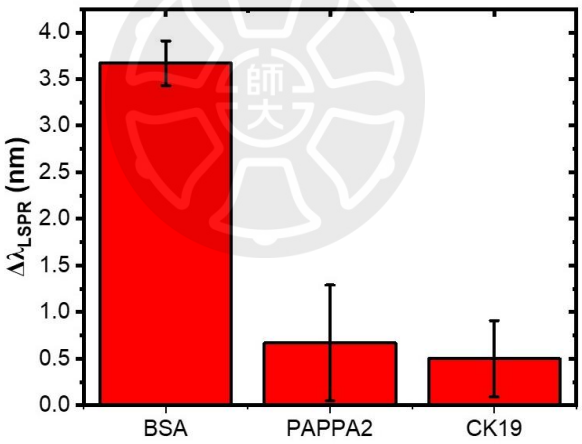

Figure 2. 17 Comparison of LSPR sensor response to BSA target, and non-target (PAPP-A2 and CK19) at a concentration of 100 ng/mL. Note: Data were taken with 3 repetitions.

At the end of this research, we compare the performance of the sensor developed in this research with other sensors that have been developed previously. The highlighted parameters are the detection limit and linear range. Related to the linear range, the sensor developed in this research has a good linear range in the

concentration range of 1 ng/mL to 10 µg/mL. Based on the fitting results in Figure 2. 16 (b), the coefficient of determination (R^2) in this range is 0.91. Furthermore, using Equation: $LOD = 3.3\sigma/k_{slope}$ where σ represents the standard deviation of the response and k_{slope} is the slope of the calibration curve, the detection limit achieved in this study is 1 ng/mL.

Table 2. 2 Linear range and detection limit of different sensors used to detect BSA

Detection mechanism	LOD	Ref.
fiber optics SPR -based sensor which is functionalized with anti-BSA	0.45 µg/mL	(Kaushik et al., 2019)
AuNR-based fluorescence biosensor with intensity investigation mode	1.3 µg/mL	(Shajari et al., 2018)
BSA was detected by an indirect immunoassay utilizing FRET and quenching of AuNPs.	0.5 nM	(P. Yang et al., 2011)
Electrochemical Impedance Spectroscopy (EIS) with gold electrodes modified with 2D silica networks, citrate-capped AuNPs and poly(diallyldimethylammonium chloride	0.84 pmol/L	(Yari & Saeidikhah, 2015)
turn-on fluorescence probe based on cationic amphiphile with diketopyrrolopyrrole decorated with methoxy- lated tetraphenylethylene	0.08 µmol/L	(Y. Chen et al., 2022)
Fluorescence biosensor utilizing aggregation and release of CdS quantum dots on carboxymethyl cellulose	0.01 μM	(Cui et al., 2020)
LSPR sensor based on AuNPs functionalized with Cys and anti-BSA	1 ng/mL	This work

Compared with other research results with the same detection case in Table 2. 2, Kaushik et al. developed FOSPR to detect BSA (Kaushik et al., 2019). In this study, the linear range of the sensor was still too narrow ranging from 10 µg/mL to 50 µg/mL. The same results were also shown by Yang et al (Shajari et al., 2018). By using the fluorescence energy transfer resonance (FRET) sensor, the linear range of the sensor was only in the range of 0.0013 mg/mL to 6.25 mg/mL. The results of this

study indicate that the LSPR sensor has quite good sensitivity with low cost and fast detection time.

2.4 Conclusions

The signal characteristics of the AuNP-based LSPR immunosensor were analyzed through computational and experimental approaches. Using the FDTD method, the optical behavior and electric field distribution around the AuNPs were studied in detail. Simulation results showed that the interparticle distance and the presence of a dielectric layer on the nanoparticle surface significantly affect the extinction and scattering cross-section spectra, as well as the resulting electric field distribution. The addition of a dielectric layer increases the electric field intensity and modifies the field distribution, allowing the field to extend slightly into the surrounding medium. This condition has the potential to increase detection sensitivity, but can also reduce the sensor's selectivity at high analyte concentrations, because the measured signal originates not only from the target bound to the receptor on the surface but also from the free target in solution. However, the evanescence wave range remains limited, so it is possible that some of the targets bound to the receptor is not fully reached by the electric field, especially if the target size is quite large. In this study, the LSPR sensor showed a linear response to the LSPR wavelength shift in the concentration range of 1 ng/mL to 10 µg/mL BSA. However, at a higher concentration of 100 ug/mL, the sensor response decreased, indicating the occurrence of the Hook effect phenomenon due to the excess amount of target interfering with the specific binding mechanism.

Chapter 3

Towards Dual-Mode Integrated Sensors: Initial Study on Resonance Modes, Performance Metrics, and Raman Signal Amplification in 1D Gold Grating Chips

3.1 Introduction

3.1.1 Theoretical backgrounds of SPR

LSPR and SPR are two plasmonic phenomena involving collective oscillations of electrons on a metal surface. The fundamental difference that distinguishes the two lies in the transducer used. For the LSPR phenomenon, this phenomenon occurs in nano-sized metal nanoparticles and this size effect causes surface plasmons to be localized on the nanoparticles. The electromagnetic field is more focused, and this phenomenon is more suitable for application for sensing based on local field intensity. Unlike the LSPR phenomenon, the SPR phenomenon occurs at the interface of metal and dielectric with a planar structure such as a thin film. The surface plasmons that are formed will propagate along the interface of the metal and dielectric. If the decay length of the two phenomena is compared, the surface plasmon wave in a thin layer

has a longer radius reaching 200 nm than the LSPR phenomenon which only has a decay length of the order of 6 nm (Hammond et al., 2014).

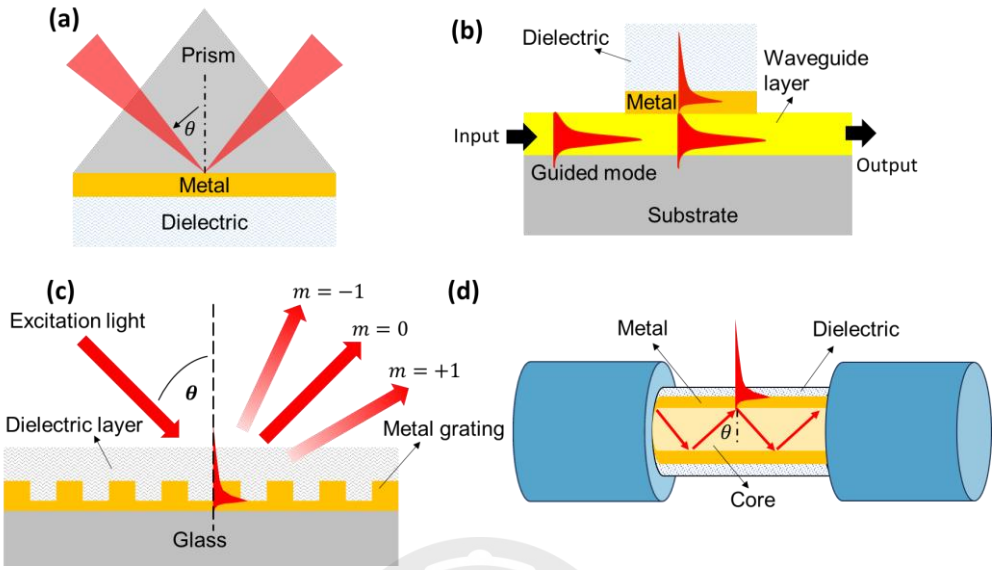

Figure 3. 1 Common configurations for achieving SPR: (a) Prism-based setup using the Kretschmann configuration, (b) Waveguide-based design, (c) Grating-based structure, and (d) Optical fiber-based system. Figure adapted from Ref. (Nurrohman et al., 2024)*, licensed under CC BY 4.0.*

To implement SPR sensor, a coupling medium is needed to achieve matching conditions. Among the many coupling methods, we classify them into four different categories as shown in Figure 3. 1. For SPR biosensors coupled with a prism, the sensor can be implemented by the attenuated total reflection (ATR) method with the Otto or Kretschmann configuration. A prism is used to focus light at the metal-dielectric interface and the incident light uses p-polarized light so that the electric field is parallel to the metal surface which is needed to create plasmon oscillations. Resonance condition occurs when the momentum of the incident light matches the momentum of the surface plasmon at the metal-dielectric interface. The energy transfer from the incident light to the plasmon causes the reflected light to be drastically reduced at certain angles or wavelengths. The change in refractive index

that occurs near the metal surface will change the resonance condition of the sensor and by measuring the shift in the resonance angle, wavelength, or reflectance intensity, small changes in the surface near the metal surface can be detected.

The second SPR system is an SPR sensor which uses a waveguide. The existence of a prism is replaced by a waveguide and light is transmitted from the source through the waveguide area that has been deposited with a metal thin film. Resonance is generated when the propagation constant of the guide mode matches the propagation constant of the surface plasmon wave. In addition to waveguides, optical fibers can also be used to implement SPR sensors. Based on the SPR sensor illustrated by Figure 3. 1 (d), the surface of the fiber core is coated with a metal film with a thickness of generally about 30-50 nm. By controlling the polarization of the incident light, some of the energy in the fiber core leaks into the fiber layer so that resonance conditions can be obtained.

In addition to the three coupling methods described above, SPR excitation can also be done by utilizing gratings. This sensor system takes advantage of the additional momentum provided by the grating effect, enabling the incident light to match the surface plasmon momentum without the need for a prism. The grating provides additional momentum through light diffraction and the resonance condition is met when:

$$k_{photon} \pm \frac{2\pi m}{\Lambda} = k_{sp} \qquad \text{Eq. 3. 1}$$

Where Λ denotes the grating period and m denotes the diffraction order. When these conditions are met, light energy is absorbed by the plasmons, resulting in a plasmonic

resonance characterized by a decrease in reflectance at a specific angle or wavelength (Pandey & Sharma, 2021). This system is also very sensitive to refractive index changes near the grating surface, making it also ideal for biosensing and spectroscopy applications.

3.1.2 Theoretical Background of Raman

Raman is a light scattering phenomenon involving the interaction between photons and molecules, resulting in changes in the energy of the scattered light (Geraldes, 2020). As shown in Figure 3. 2, when monochromatic laser light is directed at a sample molecule, most of the light is scattered with the same energy as the incident light and a small part of it will experience a change in energy. When the scattered energy is the same as the energy of the light that hits the sample, this phenomenon is called Rayleigh scattering. However, if the scattered energy is different from the energy of the incident light, this scattering is called Raman scattering which is divided into two, namely Stokes scattering (energy decreases) and anti-Stokes scattering (energy increases). The energy difference between the incoming photon and the outgoing one is called “Raman shift” (Orlando et al., 2021).

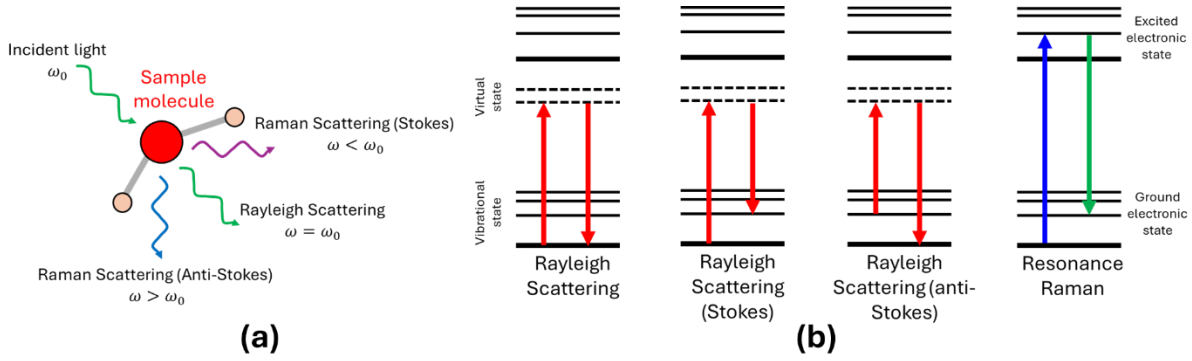

Figure 3. 2. (a) Schematic representation of the scattering mechanism. (b) Jablonski energy diagram depicting the transitions associated with different types of scattering.

Resonance Raman Scattering is a special form of Raman scattering in which the incident photon interact not only with molecular vibrations but also with electronic transitions, which increases the scattering probability and produces a more intense Raman signal (Serebrennikova et al., 2021). The intensity enhancement of this type of Raman signal can reach up to 10^6 (Orlando et al., 2021). To make it easier to understand the different scatterings explained previously, a Jablonski energy diagram has been attached as shown in Figure 3. 2 (b).

Compared with Rayleigh scattering, Raman scattering is a very weak phenomenon where only one out of 10^8 scattered photons undergo Raman scattering. Therefore, the Raman spectrometer is equipped with several tools such as notch filters to block Rayleigh scattering. Theoretically, the intensity of Raman scattering (I_R) is influenced by several factors, namely intensity and the frequency of the incident light (υ), number of scattering molecules in a given state (N), polarizability (α) and amplitude of the vibrational coordinate (Q). All of which are related by the following equation (Colthup et al., 1990):

$$I_R \propto I_0 \upsilon^4 N \left(\frac{\partial \alpha}{\partial Q}\right)^2 \qquad \text{Eq. 3. 2}$$

Where I_0 indicates the intensity of the incoming light. Theoretically, Equation (3.2) explains that Raman scattering occurs when there is a change in polarization resulting from the interaction between the sample and the incoming photon.

3.1.3 Literature Review Related to Dual-Mode Biosensors

In SPR biosensors, one of the main challenges is ensuring sensor specificity (J. Zhang et al., 2023). Because these sensors detect refractive index changes near the

sensor surface, they are highly susceptible to interference from nonspecific signals, such as temperature fluctuations and sample matrix variations, which are unrelated to target-receptor interactions. To enhance reliability, recent studies have explored a dual-mode approach that integrates multiple sensing mechanisms to detect the same analyte.

Among the various dual-mode sensors studied, the SPR sensor combined with Raman technology is an interesting one. Raman spectroscopy is widely used in chemistry, biology, and material physics due to its ability to provide molecular fingerprint information (S. Zhang et al., 2023)(D. Wang et al., 2020). Researchers such as Song et al. (2021) (Song et al., 2021), Zheng et al. (2023) (Zheng et al., 2023) and Cao et al. (2024) (Cao et al., 2024) have explored this SPR/Raman based dual-mode approach. Their research developed a sensing method that integrates SPR for analyte quantification with Raman spectroscopy which can be utilized not only for analyte quantification but also for spectral verification of targets, thereby improving accuracy and specificity.

A dual-mode sensor developed by Song et al. utilized AuNPs to detect cancer-related miRNA-652 (Song et al., 2021). As shown in Figure 3. 3, the detection mechanism in this study was based on the formation of AuNPs network induced by the presence of miRNA-652 target. Signal detection was performed through two approaches: SPR signal was obtained from dark-field microscopy (DFM) images, while SERS signal was obtained based on the ratio of Raman intensity at Raman shifts of 1500 cm^{-1} and 1580 cm^{-1} ($I_R=I_{1500}/I_{1580}$), which depended on the target concentration. This sensor had a detection limit of 42.5 fM for SPR and 2.91 fM for

SERS. Experimental results showed that this dual-mode sensor has complementary advantages. The combination of SPR and SERS not only increases detection options but also allows for re-verification of results, thereby improving the accuracy and reliability of the assay.

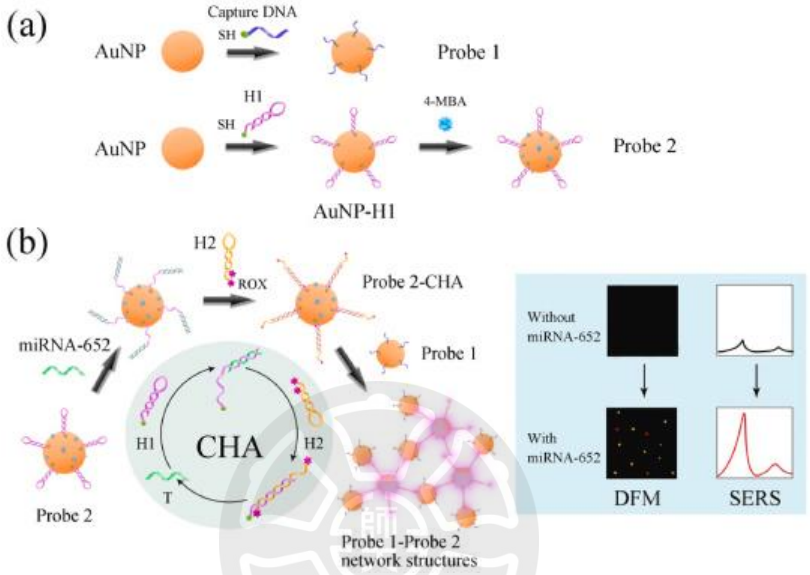

Figure 3. 3 Schematic illustration of an SPR/SERS dual-mode plasmonic biosensor designed for miRNA-652 detection, based on a CHA-induced AuNP network. (a). Nanoparticle functionalization (b) detection mechanisms. Figure adapted with permission from Ref. (Song et al., 2021)*, copyright Elsevier.*

Another study that developed dual-mode biosensors was conducted by Cao et al. (Cao et al., 2024). They designed an SPR/SERS-based dual-mode biosensor on a 1D grating chip to detect human Immunoglobulin (h-IgG). The grating chip was fabricated using wet etching-assisted direct laser interference patterning (DLIP), and the SPR investigation method was based on wavelength interrogation. As shown in Figure 3. 4, the sensor chip fabrication consists of three main steps. First, a shallow nanograting is formed on a silicon substrate using single-pulse nanosecond DLIP (Nd:YAG nanosecond laser, Continuum Surelite II-10, 355 nm wavelength, 5 ns

pulse duration, 10 Hz repetition rate). Next, the laser-treated silicon substrate is etched with a KOH solution to achieve a nanograting with controlled depth. Finally, a thin Au layer is deposited onto the silicon substrate through evaporation, forming an Au-silicon grating. Among the three grating periods investigated (490 nm, 566 nm, and 765 nm), the grating chip with a 765 nm period was selected for h-IgG detection. The study results indicate that the SPR mode exhibits better linearity; however, its detection limit remains relatively high at 23.5 nM. In contrast, the SERS mode achieves a lower detection limit of 1.176 nM.

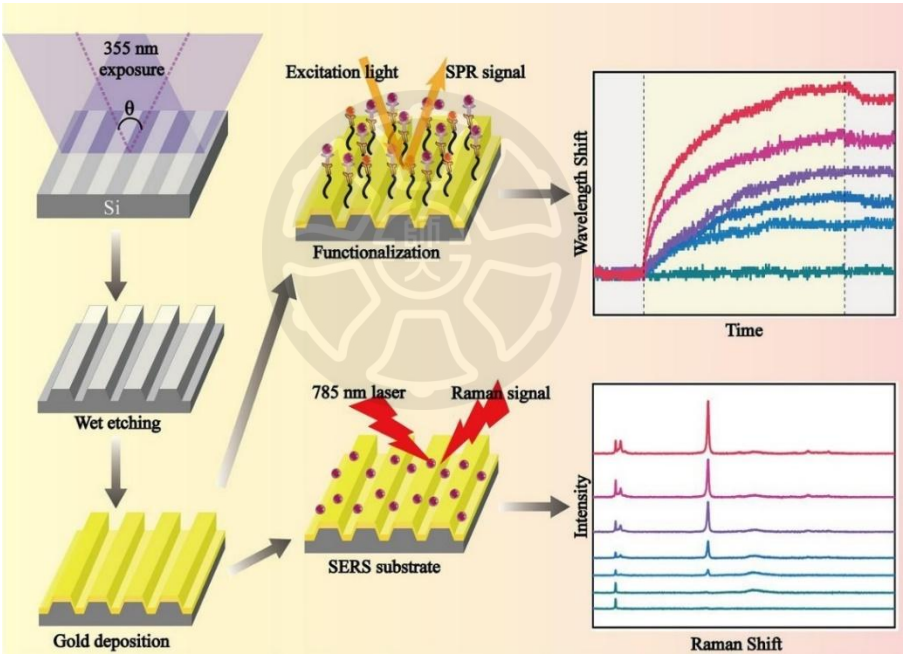

Figure 3. 4 Illustration of a dual-mode sensor based on SPR/SERS developed by Cao et al. for H-IgG detection. Figure adapted with permission from Ref. (Cao et al., 2024)*, copyright Elsevier.*

The previous section reviewed two studies on SPR/Raman dual-mode sensors utilizing AuNPs and 1D Au gratings as optical transducers. Other more complex transducers, such as silver nanohole arrays with silver nanorods (Ag NR-NH) and Au film - AuNPs sandwich structures, have also been explored (Song et al., 2020)(Y. Li

et al., 2024). These two types of optical transducers have been utilized for the detection of nucleic acids and miRNA-21. To provide a brief overview of the various dual-mode SPR/Raman sensors, we present Table 3. 1 to compare the performance of each sensor highlighted by its detection limit value.

Table 3. 1 Summary of SPR/Raman-based dual-mode sensor developments and their applications

Optical transducer	Analyte	LOD	
		SPR	Raman
AuNPs (Song et al., 2021)	miRNA-652	42.5 fM	2.91 fM
Sandwich structure of Au film and AuNPs (Y. Li et al., 2024)	miRNA-21	6.3 fM	1 fM
1D Au grating (Cao et al., 2024)	H-IgG	23.5 nM	1.176 nM
Ag Nanorod-Covered Ag Nanohole Array (Song et al., 2020)	Nucleic Acid	0.51 pM	0.77 fM
Au/GO composite membrane with AuNPs linked by double-stranded DNA (L. Li et al., 2025)	Mercury	1.82 pM	39.4 pM

3.1.4 Research Gap and Objectives

Based on all the references reviewed in Table 3. 1, the developed dual-mode sensor system has not been integrated into one sensor device. Until now, target quantification has been carried out using the same sample, but the measurements are still carried out separately in SPR and Raman devices independently. This condition causes the experimental process to become more complex and less efficient, especially for large-scale measurements. Therefore, integrating the two detection methods is essential to enhance the practicality and scalability of the sensor system for large-scale applications.

Among the various optical transducers available, grating is one of the most attractive ones to be applied in SPR/Raman dual-mode sensors because its optical

response can be easily controlled by adjusting parameters such as grating shape, thickness, and period (Bijalwan & Rastogi, 2017). In addition, smaller and more compact SPR sensors can be fabricated by utilizing this type of transducer. Munoz et al. have developed a 1 cm^2 integrated grating chip, which was then mounted on a prototype with an overall size of only 10 cm × 10 cm optical components (López-Muñoz et al., 2017). With a wavelength shift-based interrogation method, this sensor system is able to achieve a detection limit in the picomolar order. In the context of Raman sensors, grating-based optical transducers can also provide hotspots that play a role in amplifying Raman signals, thereby increasing detection sensitivity.

Based on the above facts, this study proposes the development of a SPR/Raman dual-mode sensor in an integrated sensor system. In the initial stage of the investigation, the resonance modes on a 1D grating chip with grating periods varying from 400 nm to 800 nm were analyzed using the FDTD computational method. In this stage, the optical response and signal quality of the grating chip were evaluated at three different SPR excitation wavelengths, namely 633 nm, 670 nm, and 700 nm. To validate the computational results, the grating chip was then fabricated using electron beam lithography system. Furthermore, the potential for enhancing Raman signal amplification through electric field induction due to SPR excitation was also investigated using R6G as the test material. In the future, a SPR/Raman dual-mode sensor system based on a 1D grating with an integrated system can be a sensor that is not only sensitive and accurate but also more compact.

3.2 Research Methodology

3.2.1 Simulation Details

In the initial stage of the investigation, two 1D grating chips with different periods of 400 nm and 800 nm were investigated based on computational studies using the FDTD method. Other grating parameters such as fill factor, grating thickness (h), and width of grating (w) have constant values. In detail, the dimensions of each parameter are shown in Figure 3. 5. Regarding the refractive index of the material, the refractive index of ITO was taken from a study conducted by König et al., while the refractive index of chromium (Cr) and gold (Au) were taken from the results of Johnson and Christy's study (König et al., 2014)(Johnson & Christy, 1974).

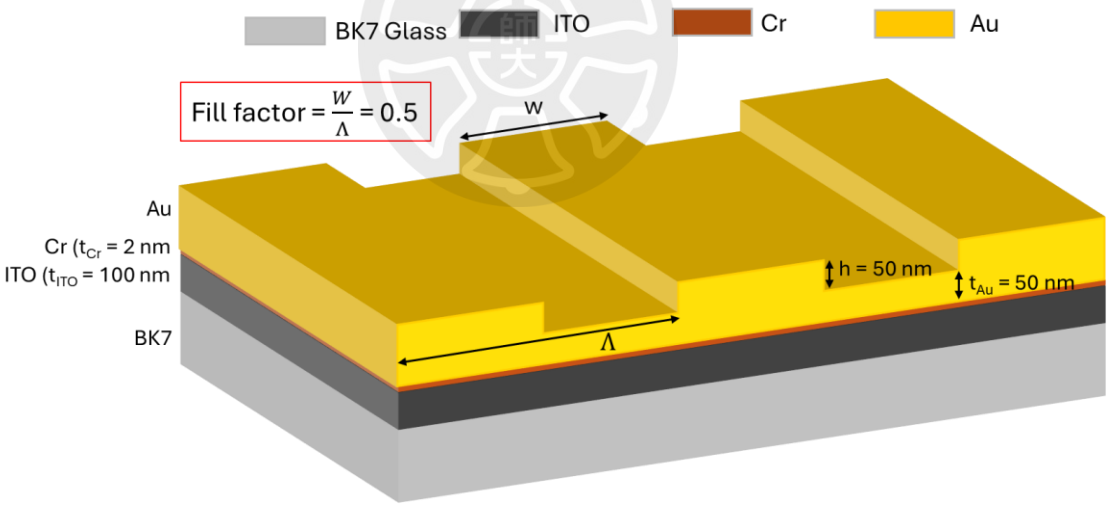

Figure 3. 5 The investigated 1D grating chip and its dimensions

The investigation mode used in this study uses the angle investigation mode and the optical properties of the 1D chip grating investigated in the computational study includes the reflectance curve and the resulting electric field profile. These two parameters are investigated at different incident light wavelengths, namely 633 nm,

670 nm and 700 nm. By using the two-dimensional FDTD computational method, the setting on the boundary along the x-axis is Bloch boundary condition while along the y-axis is the perfect matching layer (PML).

3.2.2 Fabrication of 1D nanograting

The grating chip used in this study was fabricated based on a previously established protocol with slight modifications (N.-F. Chiu, Yu, et al., 2007)(N.-F. Chiu, Lin, et al., 2007)(N.-F. Chiu et al., 2006). 1D linear gold gratings were patterned using an electron beam lithography (EBL) system (ELS-7500EX, Elionix Inc., Japan). A schematic overview of the fabrication process is shown in Figure 3. 6.

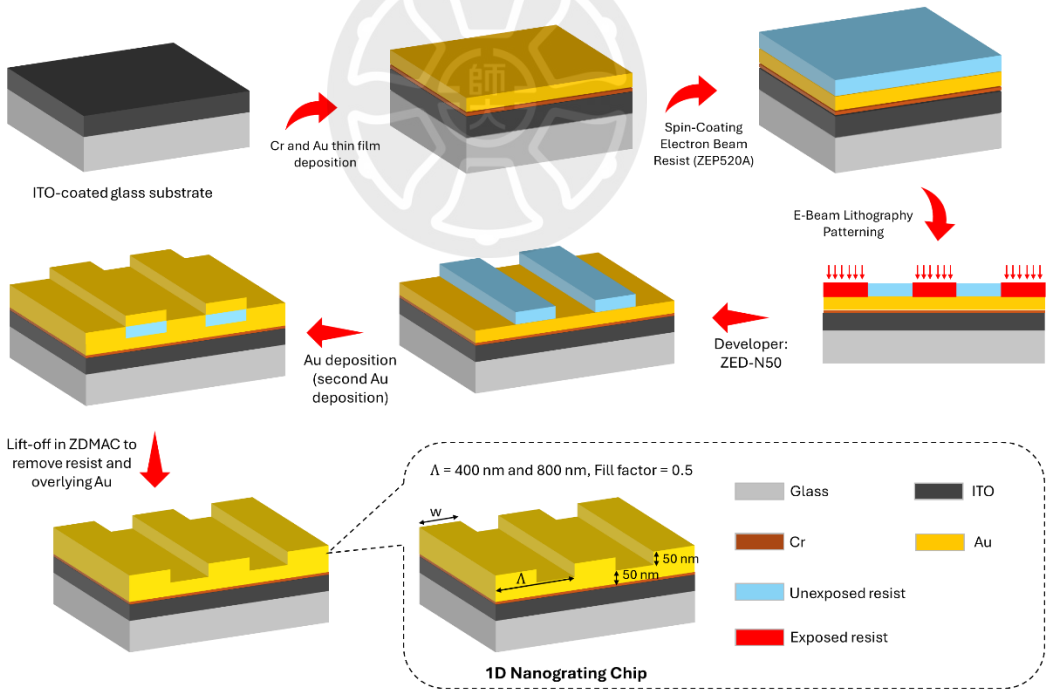

Figure 3. 6 Outline of the fabrication process of 1D nanograting chip

The fabrication process began by cleaning ITO-coated glass substrates (Product No: LT-G001, Luminescence Technology Corp.) sequentially with acetone, isopropyl alcohol (IPA), and deionized water, followed by N_2 gas drying.

Subsequently, a 2 nm chromium (Cr) adhesion layer and a 50 nm gold film were deposited sequentially via thermal evaporation. The substrates were then coated with a positive e-beam resist, ZEP520A (Zeon Co., Japan), by spin-coating at a controlled speed to achieve a uniform resist thickness of ~50 nm. The coated substrates were soft baked on a hotplate at 180 °C for 2 min to remove residual solvents and moisture.

Next, nanograting patterns with designed periods of 400 nm and 800 nm were defined using electron beam lithography with an acceleration voltage of 50 kV. The exposure was performed using a pixel map of 60,000 × 60,000 dots, resulting in a total patterned area of approximately 1.2 × 1.2 mm². Each dot was exposed for 2 μs, forming elongated 1D line gratings with a period of 400 nm and 800 nm. After exposure, the samples were developed using ZED-N50 developer (Zeon Co., Japan) for 90 seconds to selectively remove the exposed resist areas, followed by rinsing with IPA and drying.

Gold was then deposited again by thermal evaporation under a base pressure of ~2 × 10^{-6} Torr at a deposition rate of 0.2 Å/s to form the nanograting structures. Finally, a lift-off process was performed by immersing the samples in N,N Dimethylacetamide (ZDMAC, To-Nippon Zeon Co.) solution to dissolve the remaining resist and remove the unwanted gold on top of it. This resulted in well-defined periodic gold nanostructures on the substrate. The final patterned area of the gold nanograting covered approximately 1.2 × 1.2 mm² on each chip.

3.2.3 SPR-Raman Experimental Set-up

SPR-Raman set-up in this study is briefly shown by the scheme in Figure 3. 7. A white light source with Model 7ISW151 from Optics Focus has been used to excite

the SPR sensor. This light source is equipped with Czerny-Turner optic configuration and different wavelengths of light source can be obtained by controlling the 71SWS spectrometer software. The light source with controlled wavelength will pass through the polarizer to obtain p-polarized light. We use a convex lens and a pin hole to control the shape and size of the beam that hits the surface of the grating chip. Finally, the light reflected by the grating chip is measured for its intensity using a mono CCD camera. At this stage, the reflectance intensity at each different incident angle is measured automatically using the LABVIEW program on Computer 1.

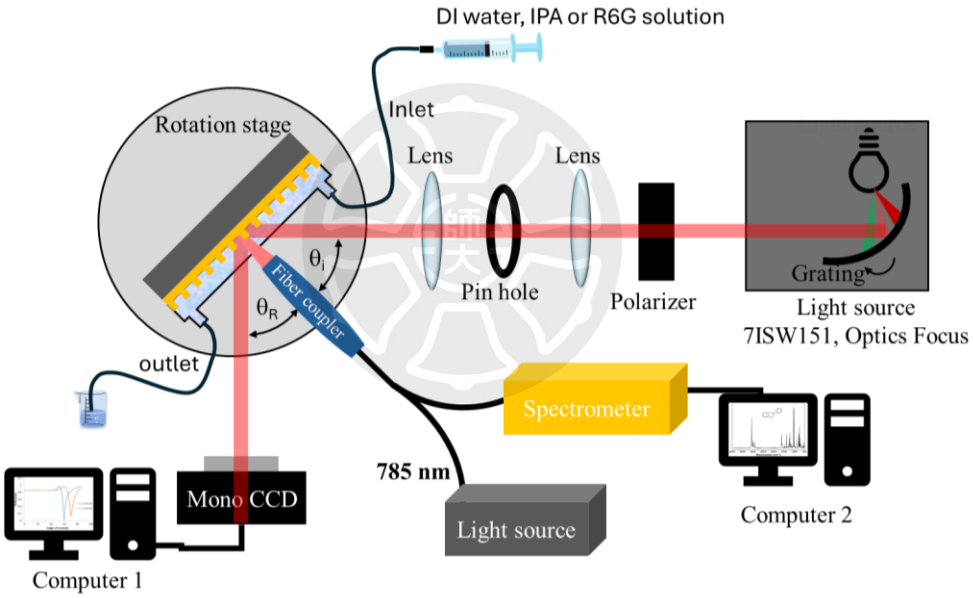

Figure 3. 7 Schematic diagram of the dual-mode SPR-Raman optical set-up. Figure adapted from Ref. (Nurrohman et al., 2025)*, licensed under CC BY 4.0.*

The Raman system used in this study uses a pre-configured Raman Spectrometer System developed by StellarNet.Inc with a default wavelength of 785 nm. The probe in the Raman measurement is installed perpendicular to the grating plane. The light scattered by the grating passes through the fiber coupler and the

light with Raman scattering will be forwarded to the spectrometer and the data is displayed by Computer 2. To experimentally explore the possibility of Raman signal enhancement through SPR excitation, R6G was chosen as the test material. Measurements will be performed under two different conditions: dry and in aqueous (aq) conditions.

3.3 Results and Discussions

3.3.1 Reflectance curve and electric field distribution

The discussion in this part will begin by presenting the results of the investigation viewed from a computational perspective. Two grating chips have been calculated the reflectance curves and electric field profiles taken at 3 different wavelengths. The sensing surface is air with a refractive index of n_s=1. From the reflectance curves shown in Figure 3. 8 (a) and Figure 3. 8 (b), the wavelength of the incident light has a very significant effect on the resonance produced. For a chip with a grating period of 400 nm (called S1 chip), the resonance angle shifts to a higher angle when the wavelength of the incident light is increased to 700 nm.

A different phenomenon is shown by a chip with a grating period of 800 nm (called S2 chip) where the resonance angle shifts to the opposite direction. What is interesting is the presence of a minor resonance on S2 chip which has the same position as the resonance angle on S1 chip (marked by the colored area). This minor resonance in S2 reflectance spectra is increasingly clearly visible when the wavelength of the incident light is 670 nm and 700 nm. From the results of the

reflectance curve analysis, we suspect that there are two different types of resonances generated by the grating chip.

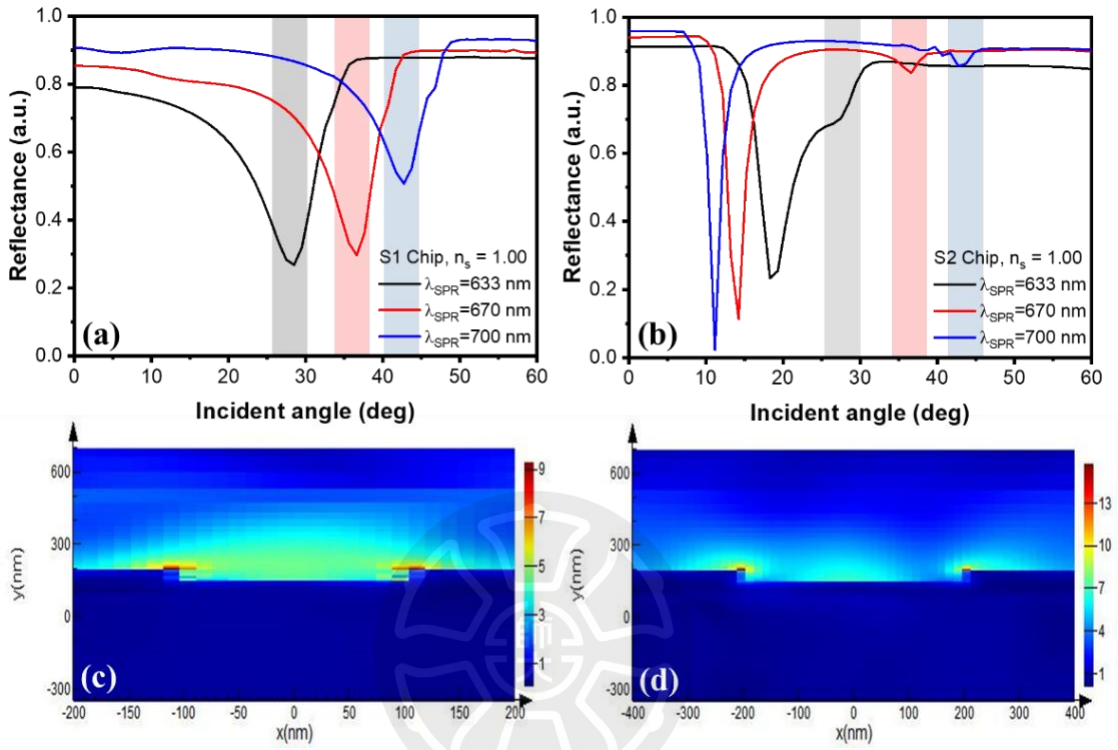

Figure 3. 8 SPR curves of (a) S1 and (b) S2 chips at different wavelengths. Electric field distributions of (a) S1 and (b) S2 chips taken at resonance angles when excited with a wavelength of 670 nm. Figure adapted from Ref. (Nurrohman et al., 2025)*, licensed under CC BY 4.0.*

To understand the physics phenomenon behind it, we study the resonance that occurs from the analysis of the electric field distribution. Figure 3. 8 (c) and Figure 3. 8 (d) show the electric field distribution of both chips taken at their main resonance angles. These two data were taken when the wavelength of the incident light was 670 nm. From the data shown, both display the same characteristics related to the position of their highest electric fields. The highest electric fields on both chips are at the grating corner. However, the S2 chip has a higher intensity which is > 13 V/m. In addition, a new source of electric fields was found originating from the grating valley.

On the S2 chip, the intensity is not too high. However, for the S1 chip, the electric field originating from the grating valley spreads even its radius passes through the grating corner. This field is predicted to be the main factor causing resonance on S1 chip. For S2 chip, the electric field originating from the grating valley is not too dominant so that the resulting resonance is only a minor resonance. The high field in the grating valley is predicted to cause cavity resonance. The shorter cavity width in S1 chip has caused repeated reflections in the grating cavity and created a trapped electromagnetic field. This effect becomes less pronounced when the valley width is increased as is the case with the S2 chip.

3.3.2 Dispersion Curve Analysis and Reflectance Map

If in the previous study the resonance mode was analyzed based on the study of the electric field, in this section we want to analyze it based on the SPR dispersion curve. Resonance due to the SPR effect can occur when:

$$k_0 n_s \sin\theta + \left(\frac{2\pi}{\Lambda}\right) m = \pm k_0 \sqrt{\frac{Re\ (\varepsilon_m)\varepsilon_s}{Re\ (\varepsilon_m) + \varepsilon_s}} \qquad \text{Eq. 3. 3}$$

where k_0 is the wave vector of the free space, ε_m is the permittivity of the metal, and ε_s is the permittivity of the sensing surface. Since the type of sensor investigated in this study uses the angle of incidence interrogation method, in the dispersion analysis we calculate the wave vector at various angles which are 15°, 30°, and 45°.

Figure 3. 9 (a) and Figure 3. 9 (b) show the dispersion curves for S1 chip and S2 chip. In both figures, the surface plasmon wave vector is shown by the black data. From the four selected angles, in the case of S1 chip, the incident light wave vector

never intersects with the surface plasmon wave vector. That means the resonance phenomenon due to the SPR effect never occurs for a chip with this dimension.

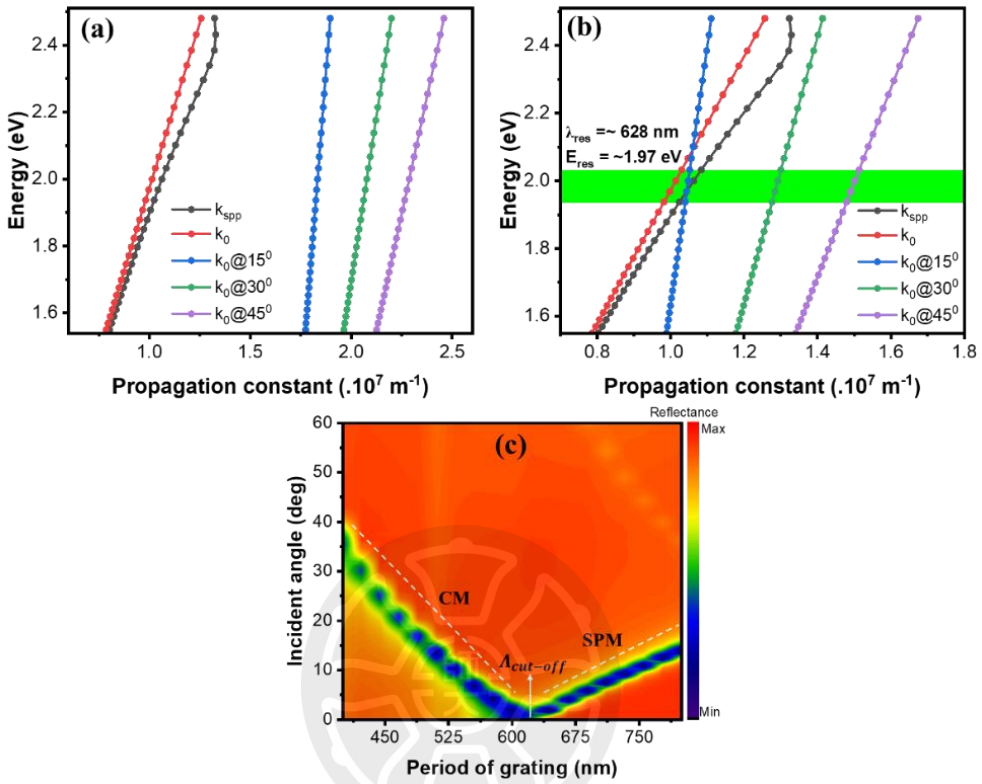

Figure 3. 9 Dispersion curves of (a) S1 and (b) S2 chips. (c) Reflectance map of 1D nanograting chips excited with 670 nm wavelength and different grating periods. Figure adapted from Ref. (Nurrohman et al., 2025)*, licensed under CC BY 4.0.*

This is different from S2 chip where the incident light wave vector intersects with the surface plasmon wave vector at an incident angle of 15°. At this angle, the excitation energy is ~1.97 eV or a wavelength of ~628 nm. The results of this dispersion analysis prove that the resonance that occurs in the S2 chip is caused by the SPR effect. The resonance equation above can be simplified as:

$$\theta = sin^{-1}\left(\frac{1}{n_s}\left(\sqrt{\frac{Re\,(\varepsilon_m)\varepsilon_s}{Re\,(\varepsilon_m)+\varepsilon_s}} - m\frac{\lambda}{\Lambda}\right)\right) \quad \text{Eq. 3. 4}$$

By utilizing this equation, the diffraction order (m) can be determined by entering the SPR angle, excitation wavelength, grating period, dielectric constant of the metal and sensing surface. The calculation results show that the diffraction order at this resonance angle is $m = +1$.

The analysis in the previous section shows that there are two different resonances displayed by the grating chip. Therefore, the reflectance curves in the range of grating period from 400 nm to 800 nm are calculated and we display the results in the form of reflectance maps. In this study, the wavelength of the incident light is 670 nm. The resonance angle in Figure 3. 9 (c) shows that the resonance angle shifts to a smaller angle until finally at an angle of 0° when the grating period is increased from 400 nm to about ~640 nm. In this period, a transition occurs which initially has a cavity mode (CM) to a surface plasmon mode (SPM). This region is called the cut-off period ($\Lambda_{cut-off}$) and can be analytically determined by the equation (W. Chen et al., 2014):

$$\Lambda_{cut-off} = \frac{2\pi m}{k_{spp} - k_x} \qquad \text{Eq. 3. 5}$$

The cut-off period obtained is 644 nm. When compared, this value is smaller than the excitation wavelength used, which is 670 nm. Therefore, the resonance observed on the S1 chip can be identified as the cavity resonance mode (CM), while the resonance on the S2 chip is the surface plasmon mode (SPM).

3.3.3 Grating characterization and resulting performance

Before the grating is measured for its SPR and Raman signals, characterization is carried out to determine the surface profile and dimensions of the fabricated grating.

To determine the surface profile of the grating, SEM characterization is carried out and the SEM images for chips S1 and S2 in this study are shown in Figure 3. 10.

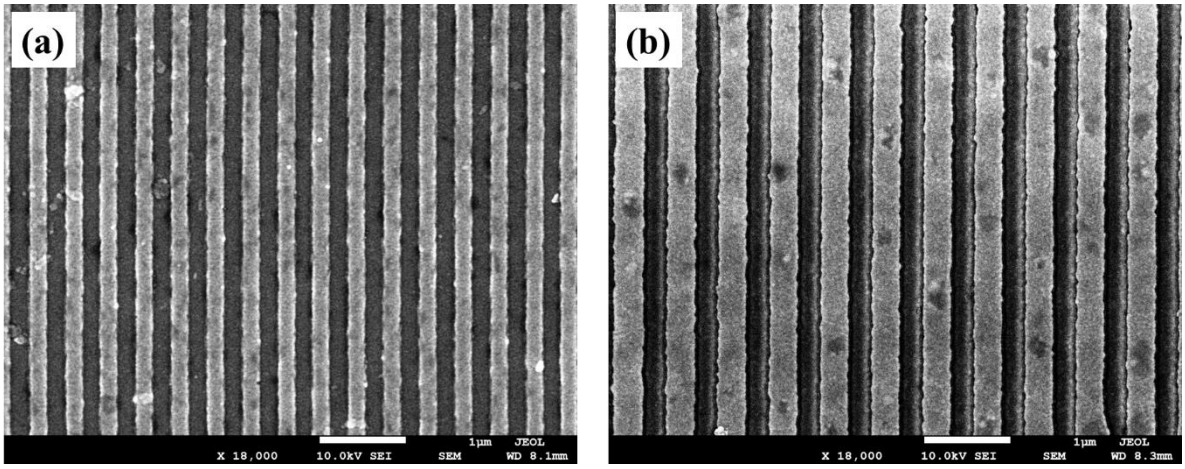

Figure 3. 10 SEM image of (a) S1 chip and (b) S2 chip. Figure adapted from Ref. (Nurrohman et al., 2025)*, licensed under CC BY 4.0.*

After the grating chips were characterized, their reflectance spectra were measured at various incident angles and wavelengths. The optical responses of S1 and S2 chips, which differ due to the variation of the incident wavelength, are presented in Figure 3. 11. Both chips show a shift in the resonance angles consistent with computational predictions. Specifically, S1 chip shows a shift to a higher angle as the incident wavelength increases, while S2 chip shows a shift to a lower angle. This trend confirms that the experimental results are in good agreement with the simulation results.

However, there are still differences in the absolute positions of the resonance angles between the experimental and simulation data for S1 and S2 chips. This difference is mainly due to the differences in the actual refractive index values of the chips and the refractive indices used in the simulations. Furthermore, the simulated

gratings exhibit ideal and defect-free structures, while imperfections are inevitable in the fabricated chips due to practical limitations in the fabrication process.

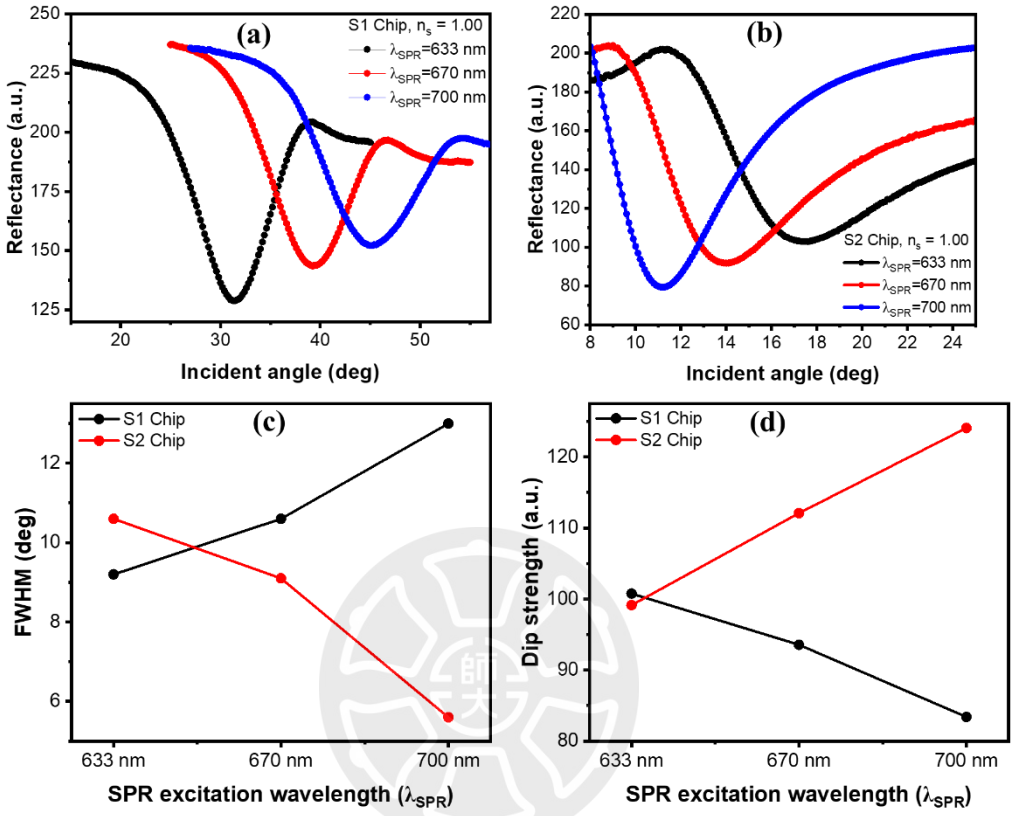

Figure 3. 11 SPR curves of (a) S1 and (b) S2 chips from the experimental results. Comparison of (a) FWHM and (b) dip strength of S1 chip and S2 chips at different wavelengths. Figure adapted from Ref. (Nurrohman et al., 2025)*, licensed under CC BY 4.0.*

The data in Figure 3. 11 (c) and Figure 3. 11 (d) are made to assess the quality of the signal produced at each wavelength. There are two quantities used, namely FWHM and dip strength. For S1 chip, a higher incident light wavelength results in a wider FWHM of the reflectance curve. This indicates a degradation of the sensor signal which means that the sensor accuracy is reduced. A different phenomenon is shown by S2 chip where the sensor accuracy becomes better when the incident light

wavelength is increased. If the signal quality is assessed from the dip strength, S2 chip which is excited with a wavelength of 700 nm also shows better quality.

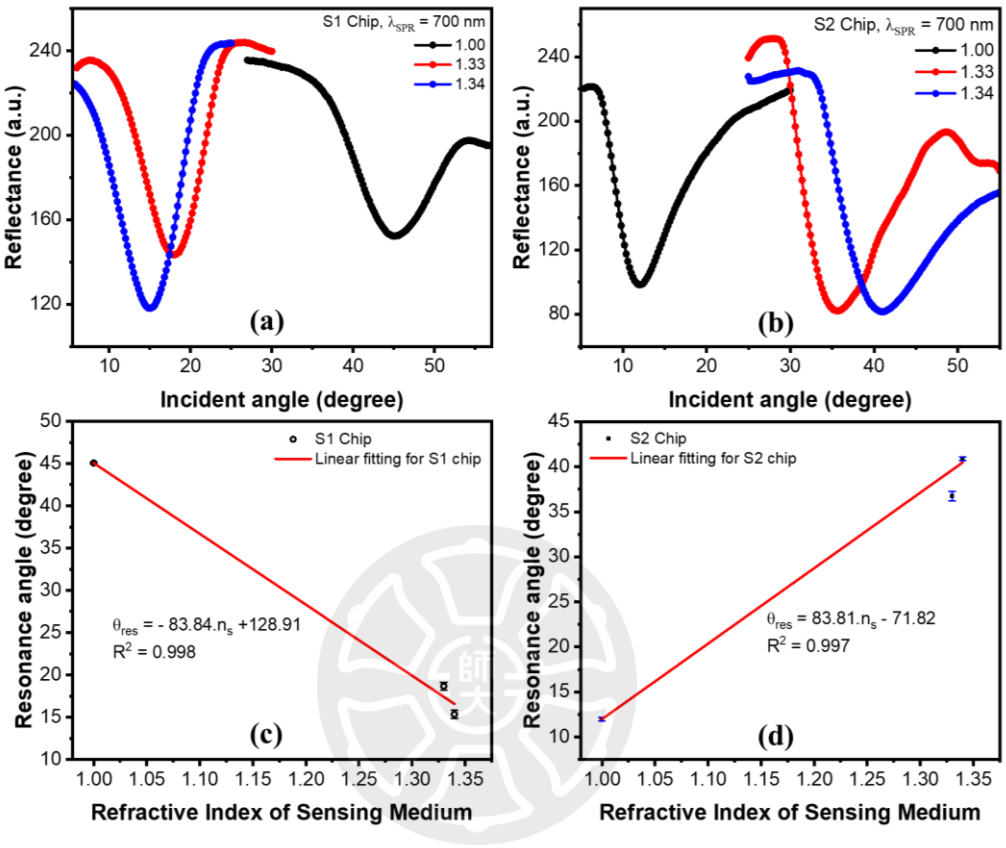

Figure 3. 12 The response of (a) S1 chip and (b) S2 chip when the sensor is excited with 700 nm incident wavelength and a different refractive index of the sensing surface. Linear fitting curves of SPR resonance angle (c) S1 Chip (d) S2 Chip. Figure adapted from Ref. (Nurrohman et al., 2025)*, licensed under CC BY 4.0.*

To complete the study, the Figure of merit of the sensor is calculated by considering the sensitivity (S) of each grating. The Figure of merit (FoM) can be determined using the following relationship:

$$FoM = \left(\frac{S}{FWHM}\right) x\ dip\ strength \qquad \text{Eq. 3. 6}$$

The sensitivity of the sensor in this study was obtained by testing the sensor on different refractive indices of the sensing medium, namely air ($n_s = 1$), water ($n_s =$

1.33) and IPA ($n_s = 1.34$). The sensitivity was obtained from the gradient value of the linear fitting results with the x-axis indicating the refractive index of the sensing medium and the resonance angle of the sensor indicated by the y-axis (X. Wang et al., 2021).

The data in Figure 3. 12 shows the sensor response when excited with a wavelength of 700 nm. Both chips, both S1 and S2 chips, show a linear response. Where the higher the refractive index of the sensing surface, the higher the angle shift that occurs. However, there is a difference in the direction of the resonance angle shift. For S1 chip, the higher refractive index of the sensing surface causes the resonance angle to shift to a smaller angle. Therefore, when the S1 chip is measured at a lower wavelength, the resonance angle cannot be obtained. The smallest angle that can be measured in this study is 5°. A smaller angle causes the light to be blocked by the mono CCD so that it cannot hit the grating surface.

When comparing the same 700 nm wavelength, the fitting results indicate that the sensor exhibits strong linearity. The sensitivity of the S1 chip is -83.84°/RIU with a coefficient of determination (R^2) of 0.998. In this context, the negative sign on the sensitivity value indicates the direction of the resonance angle shift to a smaller angle. For the S2 chip, the sensitivity is smaller, which is 83.81°/RIU with a coefficient of determination (R^2) of 0.997. However, when the Figure of Merit values are compared, the S2 chip has a performance which is 3.23 times higher than the S1 chip. Considering the Figure of Merit of the sensor, the S2 chip has been selected for further investigation in Raman measurements.

3.3.4 Effect of surface plasmon excitation on Raman signal enhancement

The reflectance curve of the grating chip and its resonance modes have been discussed in the previous section. In this section, the effect of surface plasmon excitation on the Raman signal enhancement is investigated experimentally. To determine the Raman signal enhancement that occurs, R6G has been chosen as a standard material. This material is dissolved in deionized water to obtain R6G solution with a concentration of 1 μM. The measurements were carried out in two states, namely dry and aqueous (aq) states. For the Raman signal measured in a dry state, the 10 μL of R6G solution was dropped on the grating surface and left to dry naturally at room temperature.

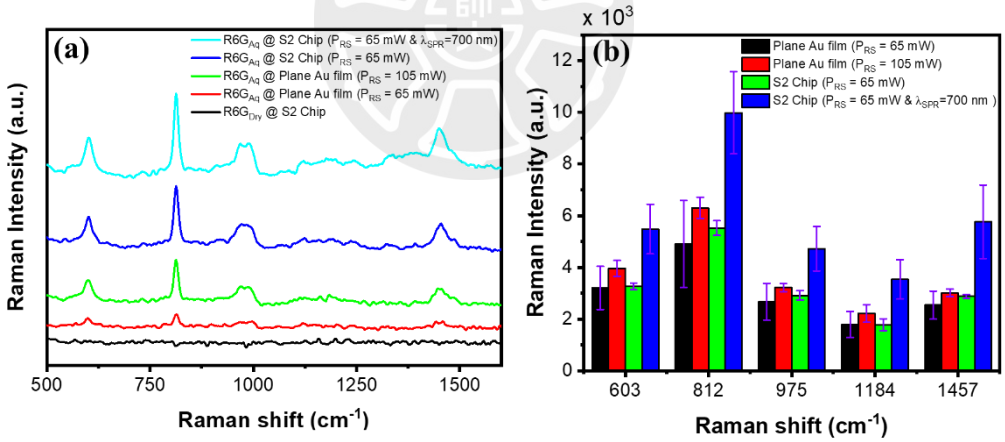

Figure 3. 13 (a) Raman signals on different substrates and treatments. (b) Comparison of Raman peak intensity on Plane Au film with S2 chip with and without SPR system. Figure adapted from Ref. (Nurrohman et al., 2025)*, licensed under CC BY 4.0.*

Based on the experimental data shown in Figure 3. 13, the Raman signal of R6G cannot be detected when the measurement was carried out under dry conditions. The resulting spectrum is dominated by high noise without the appearance of identifiable characteristic peaks of R6G. In contrast, under aqueous

conditions, the spectrum shows distinct peaks of R6G, and the vibrational modes of each peak have been summarized in Table B2 in Appendix B. In this study, the Raman spectrum of R6G obtained using a fiber optic Raman system showed different results compared to the R6G spectrum widely reported in the literature. This difference is mainly due to the type of Raman system used and the experimental conditions applied. A more detailed explanation of this can be found in Appendix B.

Raman measurements in this study were performed using a fiber probe-based Raman system developed by StellarNet Inc. Unlike the micro-Raman system which has a very small focal spot (~1 μm diameter) (Foucher, 2022)(Novák et al., 2016)(Jung et al., 2022), the fiber-based system developed by StellarNet Inc has a much larger focal spot, around 250 μm (Artemyev & Shatskaya, 2022), with a focal depth of around 1 mm (StellarNet, 2025). This large focal volume allows the excitation of a much larger number of molecules in solutions, even at low concentrations, thereby significantly increasing the Raman signal intensity. Based on the relationship in Eq. 3. 2 below, the Raman intensity and the number of molecules (N) involved in the focal volume can be described by the basic Raman intensity equation:

$$I_R \propto I_0 \upsilon^4 N \left(\frac{\partial \alpha}{\partial Q}\right)^2$$

From this equation, the number of molecules (N) excited by the laser light is an important factor in determining the strength of the detected Raman signal. Therefore, when the measurement is carried out in a liquid medium, where the molecules are homogeneously distributed and fill the focal volume, the Raman signal tends to be stronger. On the contrary, in dry conditions, the number of R6G molecules attached

to the surface becomes very limited and uneven. This causes a decrease in the number of N in the large focal volume of the fiber system, so that the signal intensity becomes very low or even undetectable.

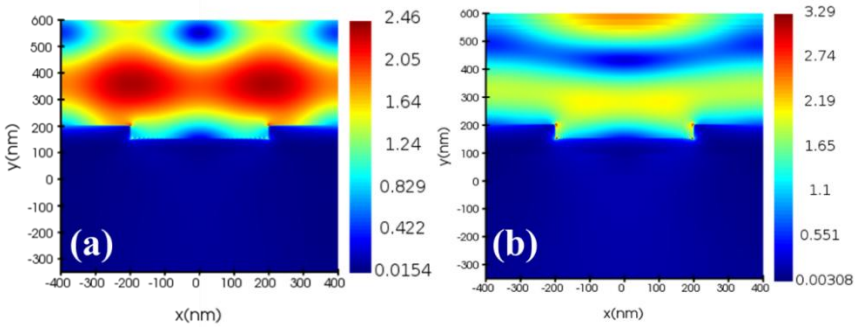

Figure 3. 14 Electric field distribution on the S2 grating chip under 785 nm excitation, comparing two sensing media: (a) air and (b) water. The presence of water enhances the local electric field intensity near the grating surface compared to air.

In addition to the above factors, the optical properties of the sensing medium also affect the efficiency of Raman excitation. Based on the results of the electric field simulation on the grating chip, it was obtained that the sensing medium in the form of water produces a higher local electric field intensity compared to air (Figure 3. 14). On the grating chip excited by a laser with a wavelength of 785 nm, the highest fields when the sensing media were air and water were 2.46 V/m and 3.29 V/m, respectively. This stronger local field supports the enhancement of molecular excitation and contributes directly to the enhancement of Raman intensity in liquid conditions.

To determine the effect of grating on Raman signal enhancement, Raman spectra of planar Au chips were also measured in this study. In aqueous conditions, the R6G peak can be identified on the planar Au chip when the Raman power (P_{RS}) used is 65 mW. The R6G peak becomes more clearly visible when the Raman power is increased to 105 mW. The presence of grating has also been shown to significantly

enhance the Raman signal. For the S2 chip with a Raman power of 65 mW, its Raman intensity has an intensity that exceeds the Raman signal intensity of the planar Au chip with a power of 105 mW. These experimental data indicate that the presence of grating has a positive contribution to Raman signal enhancement. In fact, the Raman signal can still be further enhanced when measurements are made at the SPR resonance angle. We summarize the comparison of Raman intensity in each different measurement mode in Figure 3. 13 (b)**.**

Furthermore, it is important to note that despite using laser powers up to 105 mW, no thermal damage or burning of the sample was observed during the measurements. To confirm this, repeated measurements were performed and no Raman signal instability was encountered during the experiments. This is because the macro-Raman system used in this study has a relatively large spot size (~250 μm) and a deep penetration depth (~1 mm), which significantly reduces the power density on the sample. Furthermore, the measurements were performed under aqueous conditions within the microchannel, allowing the surrounding liquid medium to act as an effective heat sink and efficiently remove heat from the irradiated area. These factors together minimize the risk of burning and ensure stable Raman measurements even at higher laser powers.

To explore the effect of SPR excitation on Raman signal enhancement, Raman measurements were performed simultaneously at three different SPR excitation wavelengths. At each wavelength, the measurements were performed exactly at its resonance angle. The measurement results are shown in Figure 3. 15, which shows the Raman spectrum and the intensity of its dominant peaks. Based on the Raman

intensity data in Figure 3. 15 (b), most of the Raman peaks increase with increasing SPR excitation wavelength. This increase is most obvious in the Raman peak at 812 cm^{-1}, which shows the highest intensity when excitation is performed at a wavelength of 700 nm. This phenomenon is thought to be closely related to the enhancement of the local electric field generated by the SPR resonance mode at higher wavelengths.

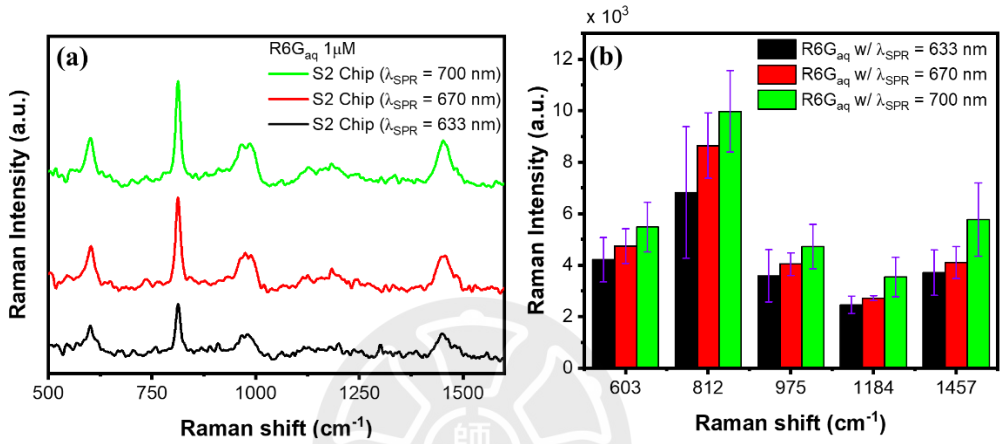

Figure 3. 15 (a) Raman signal enhanced by SPR phenomenon with different excitation wavelengths (b). Comparison of Raman peak intensities of chips excited with different SPR wavelengths. Figure adapted from Ref. (Nurrohman et al., 2025)*, licensed under CC BY 4.0.*

Theoretically, the Raman signal enhancement on the grating chip can be explained by a combination of electric field analysis from FDTD simulation results, diffraction phenomena, and SPR excitation mechanisms. Based on the simulation results shown in Figure 3. 16 (a), the electric field on the plane Au film (without a grating pattern) shows a relatively homogeneous distribution, with non-localized field around the surface of plane Au film chip. At a Raman excitation wavelength of 785 nm, the maximum peak electric field intensity is only ~1.97 V/m. This result indicates that the planar structure does not have an efficient coupling mechanism to enhance the electric field locally. As a result, its contribution to the Raman signal enhancement

is very limited. This limitation is caused by the failure to fulfill the momentum matching condition required to induce the surface plasmon mode, due to the absence of additional momentum components in the tangential direction as provided by the grating structure.

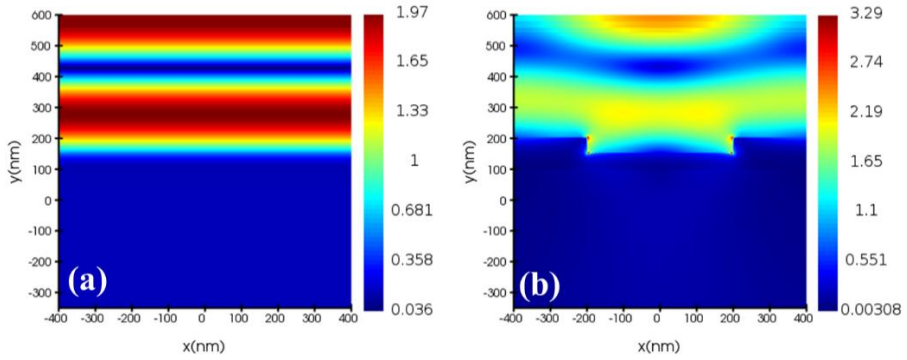

Figure 3. 16 Electric field profiles of (a) flat gold film and (b) S2 grating chip when excited at a wavelength of 785 nm with incident light perpendicular to the chip.

In contrast, in Figure 3. 16 (b), the electric field is mapped on the surface of the chip grating excited with a wavelength of 785 nm in a perpendicular or normal incidence configuration. Although there is an increase in the electric field intensity compared to the planar structure, reaching a maximum value of 3.29 V/m, the resulting electric field distribution looks uneven and forms a more complex and fluctuating pattern around the grating relief. This increase does not originate from the SPR excitation but rather is caused by the diffraction effect produced by the periodic structure of the grating. At an incident angle of $0°$, the tangential component of the light wave vector is insufficient to meet the momentum matching requirements required to induce surface plasmon polaritons. As a result, plasmon resonance cannot be formed efficiently. This is supported by the calculation results based on

the diffraction coupling model, which is described by Eq. 3. 3. By entering the refractive index of gold at the Raman excitation wavelength of 785 nm, which is 0.14891 + 4.783i, the refractive index of the medium on the grating surface is 1.33, the grating period is 800 nm, then the resonance condition is achieved when the incident angle is ~25.24° and the diffraction order m is +1. Therefore, when the excitation is performed at an angle of 0°, as in this simulation, then the momentum matching does not occur, which causes the SPR mode not to form. As a result, the intensity of the generated electric field remains at a moderate level and the formation of hotspots becomes less than optimal.

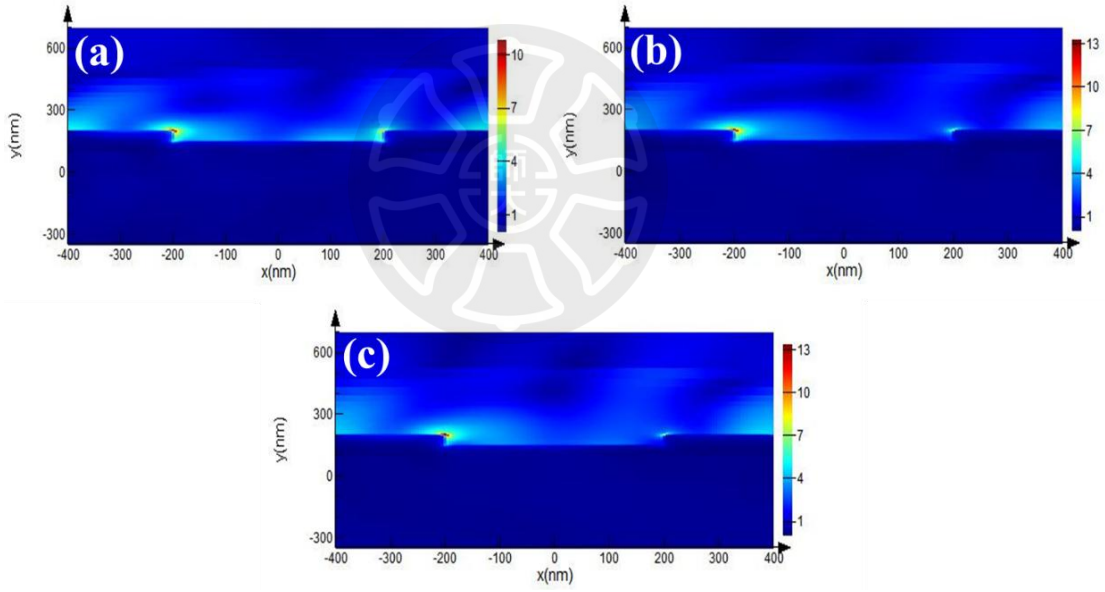

Figure 3. 17 Electric field profiles of the S2 grating chip excited at different SPR wavelengths, each at its resonance angle: (a) 633 nm, (b) 670 nm, and (c) 700 nm. Figure adapted from Ref. (Nurrohman et al., 2025)*, licensed under CC BY 4.0.*

Compared with the Raman signal without SPR excitation, the data in Figure 3. 13 (a) show that the Raman spectrum measurement carried out simultaneously with the SPR excitation results in a significant increase in the Raman signal intensity. Therefore, to further understand the effect of the SPR excitation wavelength on this

Raman enhancement phenomenon, the electric field profile analysis was carried out for three different SPR excitation conditions. The simulation results are shown in Figure 3. 17. The electric field profiles shown by the three different wavelengths show that the local electric field is concentrated on the grating corner which is very different from the electric field profile of the grating chip when excited with a wavelength of 785 nm in the previous discussion. The SPR resonance mode causes light to be effectively absorbed by the chip more optimally, reducing the diffraction effect and strengthening the local grating field. The peak values of the electric field when excited with wavelengths of 633 nm, 670 nm and 700 nm are 10.8 V/m, 13.29 V/m, and 13.40 V/m, respectively. This field enhancement is an indication of successful SPR excitation, which occurs when the tangential component of the incident wave vector satisfies the momentum matching condition with the plasmon wave at the metal-dielectric interface.

The Raman intensity enhancement can be explained by the local electric field enhancement mechanism, which is quantitatively expressed in the equation (Yamamoto et al., 2014)(Hardy & Goldberg Oppenheimer, 2024):

$$|M_{total}|^2 = \frac{|E_{loc}(\omega_L)|^2 |E_{loc}(\omega_R)|^2}{|E_{inc}|^4} \quad \text{Eq. 3. 7}$$

Here E_{loc} indicates the local electric field concentrated due to the presence of nanostructures, at the laser frequency (ω_L) and Raman band (ω_R), while E_{inc} is the incident electric field in the absence of nanostructures. In the context of this study, although the Raman excitation and SPR excitation come from two different light sources, the local electric field hotspots caused by both excitations are at the same

location, namely at the grating corner. SPR excitation plays a dual role in enhancing the Raman process: first, by increasing the excitation field $E_{loc}(\omega_L)$ because SPR produces a very strong localized field around the metal surface; and second, by enhancing the Raman emission field $E_{loc}(\omega_R)$, because the local field also affects the efficiency of the Raman signal emission. The high local field allows for increased interaction between the electromagnetic field and the target molecules adsorbed on the surface, thereby significantly increasing the probability of Raman scattering. This field is concentrated around the grating surface, amplifying both the excitation and emission processes, ultimately leading to an enhancement of the Raman signal.

If the Raman signal enhancement on different substrate and SPR excitation wavelengths are compared quantitatively where the Raman intensity of the plane Au film substrate (denoted as I_{RS}) is compared with the intensity of the 1D nanograting chip without SPR excitation (I_{SERS}) and with SPR excitation ($I_{SERS+SPR}$). At a Raman shift of 812 cm^{-1}, the 1D nanograting chip shows a Raman intensity enhancement of 2.03 times compared to the plane Au film substrate. More interestingly, when SPR excitation at a wavelength of 700 nm is used, the Raman peak intensity increases significantly to 3.03 times the initial value. This finding confirms the superiority of the 1D nanograting structure combined with SPR excitation in amplifying the Raman signal, while opening up great opportunities for the development of dual-mode biosensors that are not only able to improve the sensitivity of analyte quantification but also provide specific spectral information as a molecular fingerprint of the detected target.

3.4 Conclusions

This study investigates different resonance modes in 1D nanograting chips through both computational and experimental approaches. Among the two grating periods examined, the 400 nm period chip displays a cavity mode, while the 800 nm period chip exhibits an SPR mode. Comparing the FoM of both chips, the 1D nanograting chip with an 800 nm period shows a 3.23-fold higher FoM than the 400 nm period chip. The findings also demonstrate that the Raman signal intensity can be enhanced by adjusting the incident angle and SPR excitation wavelength. Integrating SPR and Raman techniques leverages complementary advantages, making it crucial for advancing high-performance sensor development.

Chapter 4

Computational Insights into MoS_2 and WS_2-Based Non-Metal Lossy Mode Resonance Sensors: Achieving Wider Dynamic Range and High Sensitivity

4.1 Introduction

4.1.1 Working Principle of LMR Sensors

LMR and SPR-based biosensors are two technologies that utilize optical resonance phenomena to detect refractive index changes on the sensing surface. Both types of sensors can be excited using a prism or optical fiber as a coupling medium, as shown in Figure 4. 1. In LMR sensors coupled with a prism, ATR principle with a Kretschmann configuration is used to generate resonance (Shen et al., 2024). Detection mechanism of LMR sensors with this coupling medium can be done through resonance shifts in the incident angle or wavelength (Y. Zhang et al., 2022)(Villar et al., 2017), while in LMR sensors coupled with optical fibers, the investigation mode is generally carried out by analyzing the shift in the transmission wavelength (Semwal & Gupta, 2020)(Prieto-Cortés et al., 2019).

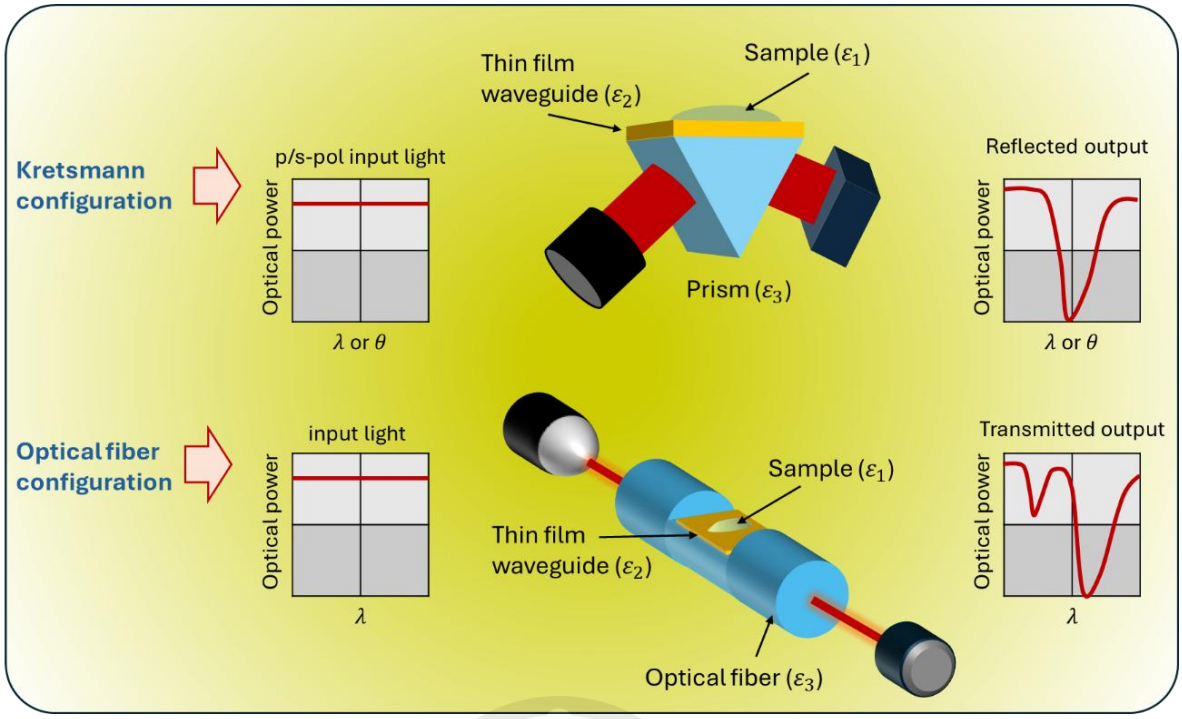

Figure 4. 1 Set-ups for LMR and SPR generation.

In principle, the main difference between LMR and SPR biosensors lies in the type of transducer material used to generate resonance. In SPR biosensors, resonance occurs due to the excitation of surface plasmon waves at the interface between the metal and the dielectric material. To trigger the SPR phenomenon, the real part of the dielectric constant of the transducer material must be negative, indicating a small real refractive index and a relatively high imaginary component (Kaur et al., 2014). These properties are generally possessed by metals such as gold, silver, and aluminum (Mishra & Mishra, 2016)(Lambert et al., 2020).

Unlike SPR sensors that can only be excited by p-polarized light, LMR sensors can be excited by p- and s-polarized light. The transducer in an LMR sensor does not require special metal properties as in SPR, thus allowing the use of various

alternative materials, such as metal oxide (Usha et al., 2018), polymers (Letko et al., 2024), and 2D materials (Qiu et al., 2021). Resonance in LMR sensors is caused by energy dissipation in the lossy layer and this type of sensor can be excited using materials that have permittivity with positive real values (Sicacha et al., 2021). Based on the parameters defined in Figure 4. 1, LMR can be generated simply if the following four conditions are met: (1) Re $(\varepsilon_2) > 0$, (2) Re $(\varepsilon_2) >$ Im (ε_2), (3) Re$(\varepsilon_2) > {n_1}^2$, (4) Re$(\varepsilon_2) > {n_3}^2$(H. Wang et al., 2022).

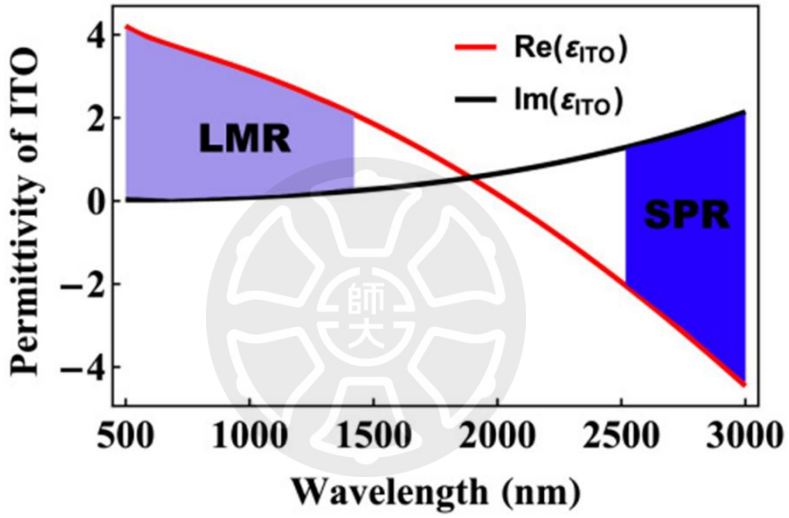

Figure 4. 2 Real and imaginary parts of dielectric constant of ITO as a function of wavelength Reprinted with permission from (H. Wang et al., 2022)*, Optical Society of America.*

To understand how SPR and LMR are excited, consider the ITO dispersion curve shown in Figure 4. 2. The SPR condition in ITO can be observed in the wavelength range of around 2500–3000 nm, depending on the ITO structure (film thickness, deposition method, and material quality) while the LMR condition can be observed in the wavelength range of around 500–1200 nm. The differences in material characteristics and excitation mechanisms open up the potential for wider

applications of LMR sensors, especially in detecting refractive index variations in complex and diverse environments.

4.1.2 Literature Review Related to LMR Sensors Development

LMR Sensor was first demonstrated by Villar et al in 2010 (Villar et al., 2010). The first investigation was conducted on fiber optic based LMR sensor with ITO as lossy layer. The LMR sensor in this study used the transmission wavelength shift investigation mode with the setup shown in Figure 4. 3. LMR signals with different ITO thicknesses of 115 nm and 220 nm were investigated in this study and from the data shown in Figure 4. 3 (b), the ITO layer with a higher thickness showed a smaller LMR sensor sensitivity. In 2015, Villar et al also investigated an LMR sensor coupled with a prism (Villar et al., 2015). This study measured the reflectance of the ITO lossy layer in the wavelength range of 500 nm to 2000 nm. The results of the investigation showed that the properties of ITO allow the acquisition of LMR and SPR using the same experimental setup.

Although LMR sensors offer greater flexibility with the use of more diverse materials, this type of sensor is still less popular compared to SPR sensors. In fiber optic-based LMR sensors, more significant developments have been achieved compared to prism-based LMR sensors, where lossy materials such as ITO (Lopez et al., 2011), In_2O_3 (Zamarreño et al., 2010), Aluminum doped zinc oxide (AZO) (Ozcariz, Piña-Azamar, et al., 2019), TiO_2 (Tien et al., 2018), indium-gallium-zinc oxide (IGZO) (Ozcariz, Dominik, et al., 2019), and Copper Oxide (CuO) (Ozcariz, 2018) have been successfully investigated experimentally. For prism-based LMR

sensors, the progress achieved so far has not been too significant because several research results show that LMR sensors coupled with prisms exhibit low sensitivity and limited dynamic range.

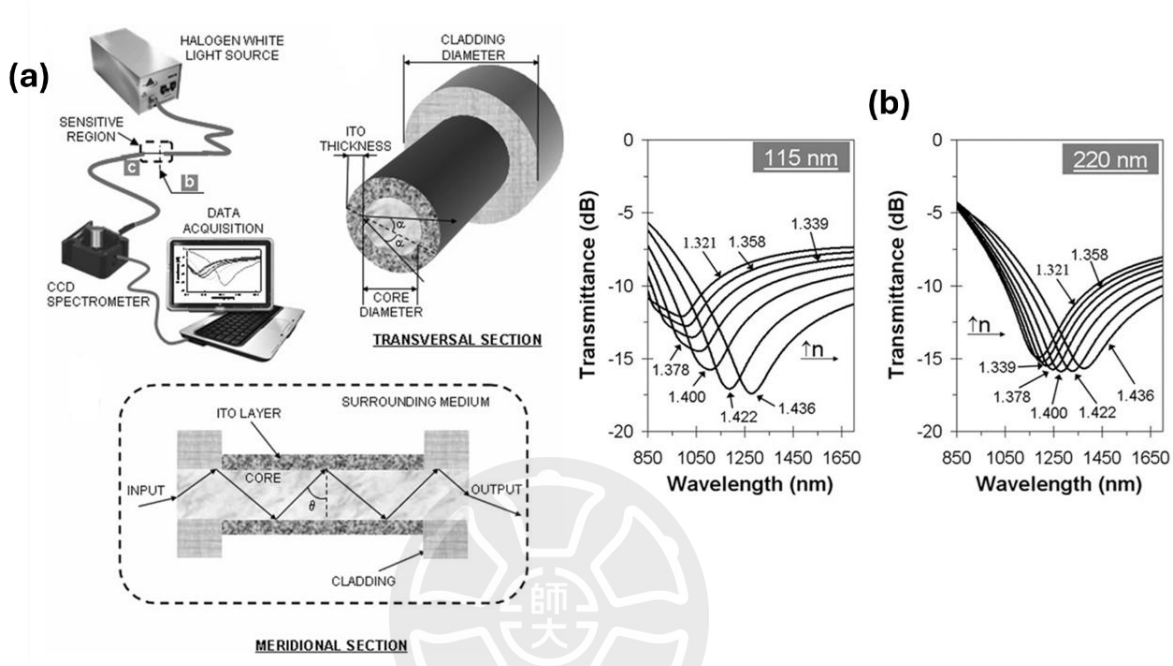

Figure 4. 3 (a) ITO-coated optical fiber sensor setup (b) LMR Experiment Results with 115 nm and 220 nm ITO. Adapted with permission from Ref. (Villar et al., 2010)*, copyright IEEE.*

One approach that can be used to optimize the performance of LMR sensors coupled to prisms is to add a matching layer placed between the lossy layer and the coupling medium. This layer is designed to match the refractive index between the core or waveguide substrate (such as BK7 glass or silicon) and the lossy layer. The refractive index and thickness of the matching layer affect the light coupling between the evanescence wave and the lossy mode in the lossy layer which will affect the quality of the resonance curve and its field distribution (Shen et al., 2024).

Saini et al. developed an LMR sensor by utilizing a transducer consisting of LiF as a matching layer and ZnO as a lossy layer to detect sucrose (R. Saini et al., 2020). The investigation mode in this study used the incident angle shift mode with the experimental setup shown in Figure 4. 4 (a). The thickness of LiF and ZnO in this study has been optimized and the highest sensitivity produced in this study was only 61.92°/RIU when excited with p-polarized light and 68.8°/RIU when excited with s-polarized light.

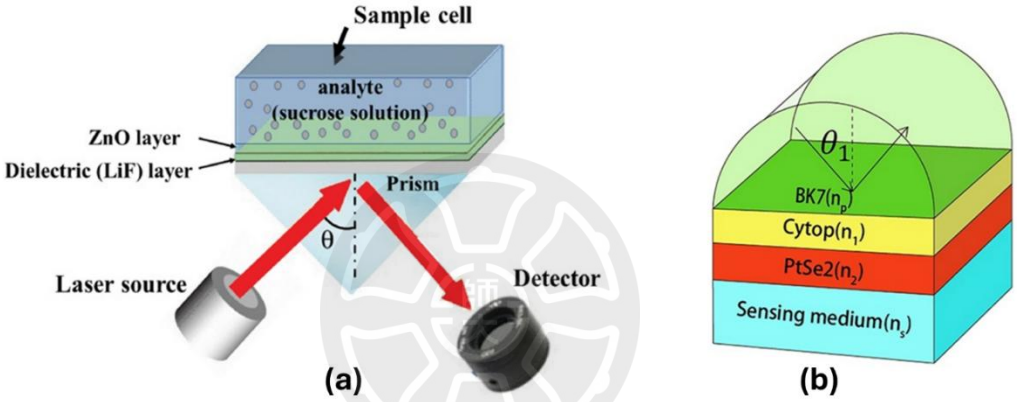

Figure 4. 4 LMR sensors investigated by (a) Saini et al. and (b) Qiu et al. Adapted with permission from Ref. (Qiu et al., 2021)(R. Saini et al., 2020)*, copyright Springer and IEEE.*

A different structure has been developed by Qiu et al. by utilizing Cytop and $PtSe_2$ (Qiu et al., 2021). The investigated structure is shown in Figure 4. 4 (b) and the optimized LMR sensor was finally tested over a refractive index range from 1.33 to 1.342. The computational results in this study indicate that the sensitivity of the LMR sensor built from Cytop and $PtSe_2$ is only 37.57°/RIU.

4.1.3 Research Gap and Objective

In SPR biosensors, gold is still considered the most suitable material due to its high resistance to oxidation and corrosion, as well as its good chemical stability. However,

the gold surface has limited biomolecule adsorption capacity, which can limit the sensitivity of the biosensor. One strategy to increase sensitivity is to add high refractive index materials such as graphene, TMDs, black phosphorus (BP), and MXene to the metal surface. These 2D materials have several advantages that are beneficial to the performance of SPR biosensors, including a high surface area to volume ratio, which allows more efficient biomolecule adsorption than gold (Szunerits et al., 2013). In addition, the presence of 2D materials in silver or copper-based SPR biosensors also functions to protect the transducer layer from oxidation (Scardamaglia et al., 2021)(Kravets et al., 2014), allowing the use of alternative metals such as silver, copper, and aluminum as plasmon-active interfaces. Another advantage is the very thin thickness of the 2D material, which allows control of the sensitivity of the SPR biosensor down to the atomic scale.

Although the incorporation of 2D materials can enhance the sensitivity of SPR biosensors, it often comes at the cost of sensor accuracy due to the broadening of the resonance curve (FWHM), which arises from the absorptive nature of these materials (Y. Wang et al., 2022)(Y. Wang et al., 2024). To address this limitation, increasing attention has been directed toward LMR-based sensor platforms, which, in contrast, exploit local electromagnetic losses to generate resonance modes (B. Li et al., 2025). In this context, materials such as MoS_2 and WS_2 are particularly promising, as they are capable of producing sharp and stable resonance modes without relying on noble metals. These materials possess high complex refractive indices, enabling strong coupling between optical modes and the material layers (Chiavaioli & Janner, 2021)(Akila et al., 2024).

The optical properties of TMDs are dominated by excitons. Therefore, these materials have high refractive indices and absorb light strongly at excitonic resonances as demonstrated in the study by Xu et al (Xu et al., 2019). According to Liu et al., MoS_2 and WS_2 exhibit high real refractive indices (n ~ 5) in the visible range (H. L. Liu et al., 2020). These high dispersion values and significant absorption characteristics are crucial for supporting resonance conditions in LMR sensors. Similar to other 2D materials, MoS_2 and WS_2 can be utilized in either monolayer or multilayer forms, allowing precise control over the thickness of the active layer, which is a critical factor in determining the position and quality of LMR resonances. Moreover, in comparison to black phosphorus (BP), which is highly reactive in ambient conditions, MoS_2 and WS_2 offer superior chemical and thermal stability, making them more suitable for long-term use in practical environments (Bahri et al., 2024). Both surfaces are also readily chemically functionalized, allowing specific adjustment to sensing targets. Functionalization strategies for these materials typically fall into two main categories: non-covalent interactions such as Van der Waals force, hydrogen bonding, and hydrophobic interactions and covalent interactions, including gold sulfhydryl bonding, sulfur vacancy engineering, and $\pi - \pi$ coordination covalent bonding (Seo et al., 2020)(Sun et al., 2022). These approaches not only enhance the specificity and sensitivity of LMR sensors but also expand the applicability of MoS_2 and WS_2 in real-world biosensing scenarios, including in harsh or oxidizing environments where stability is critical.

Although several studies have reported LMR sensor configurations with various material combinations, the performance achieved still shows limitations in

terms of dynamic range and sensitivity. In Table 4. 1, the widest dynamic range of the LMR sensor only starts from 1.33 to 1.45. In addition, cytop and TMD-based configurations with cytop thicknesses between 1000 and 2500 nm only achieve a maximum sensitivity of 50.4°/RIU, lower than the LiF/ZnO configuration which is able to reach 68.8°/RIU. Therefore, further optimization of the selection of matching and lossy layer materials, as well as appropriate adjustment of the layer thickness, is required.

Table 4. 1 Comparison of LMR sensor sensitivity with different coupling methods and structures

Structure	**Polarization**	**Dynamic range**	**Sensitivity**	**Ref.**
Coupling method: Prism				
BK7/Cytop/PtSe2	p-pol	1.33 – 1.342	37.57°/RIU	(Qiu et al., 2021)
BK7/Cytop/TMDs	s-pol	1.33 – 1.335	50.4°/RIU	(Wu et al., 2019)
BK7/Cytop/BP	s-pol	1.33 – 1.38	67°/RIU	(Wu et al., 2018)
	p-pol	1.33 – 1.38	60°/RIU	
BK7/[silicon/graphene]^{9}	p-pol	1.33 – 1.40	35.29°/RIU	(Maurya et al., 2018)
BK7/LiF/ZnO	s-pol	1.33 – 1.45	61.92°/RIU	(R. Saini et al., 2020)
	p-pol	1.33 – 1.45	68.8°/RIU	
Coupling method: FO				
SnO_2	p-pol	1.3333 -1.3525	3.40 nm/vol%	(Prasanth et al., 2021)
ITO	p-pol	1 µg/L − 500 mg/L	-	(Chiavaioli et al., 2018)
ZnO/polypyrrole	NA	0 to 10-6 g/ml	6.47 nm/gml^{-1}	(Gupta et al., 2016)
ITO	NA	50 – 700 ppb	4.40 pm/ppb	(Dominguez et al., 2023)

This research was conducted computationally to develop an LMR sensor with a wider dynamic range and higher sensitivity. The materials used include Cytop and MgF_2 as matching layers, and MoS_2 and WS_2 as lossy layers. The sensor performance evaluation was carried out numerically using the transfer matrix method

by considering various parameters, such as polarization and wavelength of incident light. Unlike previous studies that generally used matching layer thicknesses above 1000 nm, in this study the effect of matching layer thickness was analyzed in more depth through reflectance contour maps in the thickness range of 0 to 1200 nm. The optimized LMR sensor was then tested in the refractive index range of 1.331–1.5 and compared with the SPR sensor in terms of dynamic range, sensitivity, signal quality, and penetration depth. It is expected that the optimized LMR sensor can show superior performance and become an innovative alternative to replace the SPR sensor which is highly dependent on gold, thus supporting more precise, stable, and inexpensive optical detection.

4.2 Simulated LMR Chip Details

The LMR sensor investigated in this study was designed for a wide dynamic range. Initial testing was conducted at refractive indices ranging from 1.33 to 1.401, the highest values observed for cancer cells, as shown in Table 4. 2. Subsequently, the dynamic range of the LMR sensor was compared to that of the SPR sensor at an extended refractive index of up to 1.5. This refractive index is possessed by many proteins as discussed in Chapter 2. Sensors with a broad dynamic range are widely utilized in optical sensing experiments, particularly those involving various biological fluids such as plasma, serum, urine, and organic solutions (Rupert et al., 2018). This approach enhances the sensor's ability to detect a wide range of analytes with high accuracy while maintaining sensitivity at higher refractive indices.

As shown in Figure 4. 5, the LMR sensor investigated in this study consists of lossy layers, specifically MoS_2 and WS_2, and is optimized with a matching layer of either Cytop or MgF_2. This study focuses on evaluating and comparing the performance of LMR sensors using these matching layers in combination with different 2D materials as lossy layers. The investigation begins by determining the optimal thickness of both the matching layer and the 2D material to achieve a sharp resonance dip. To ensure practical feasibility, the maximum number of 2D material layers examined was set to 30, based on the fabrication results reported by Dhar et al. (2020) using the laser ablation method (Dhar et al., 2011).

Table 4. 2 Refractive Index Comparison Between Healthy and Cancerous Cells (Yasli, 2021)(Parvin et al., 2021)

Cancer Type	Cell Type	Normal Cell	Cancer affected cell
		Refractive Index	
Skin	Basal	1.360	1.380
Cervical	Hela	1.368	1.392
Blood	Jurkat	1.376	1.390
Adrenal Gland	PC12	1.381	1.395
Breast	MDA-MB-231	1.385	1.399
Breast	MCF-7	1.387	1.401

Regarding the refractive index of the material used during the computation process, the BK7 prism has been selected as the optical component of the LMR sensor with the refractive index at different wavelengths determined based on the following equation (Y. Jia et al., 2019):

$$n_{BK7} = \left(\frac{1.03961212\lambda^2}{\lambda^2 - 0.00600069867} + \frac{0.23179344\lambda^2}{\lambda^2 - 0.0200179144} + \frac{1.03961212\lambda^2}{\lambda^2 - 103.560653} + 1 \right)^{1/2} \quad \textit{Eq. 4. 1}$$

On the surface of the prism, a matching layer of Cytop or MgF_2 is applied, with refractive indices of 1.33 and 1.38, respectively (C. Chen et al., 2014)(Nurrohman & Chiu, 2024b)(Y. Lu et al., 2022). This matching layer can then be coated with MoS_2 or WS_2, whose refractive indices are referenced from the study by Hsu et al. (2019) (Hsu et al., 2019). A key advantage of these 2D materials lies in their atomic-scale thickness, allowing for precise optimization of the LMR chip's performance by adjusting the number of layers. Specifically, the monolayer thicknesses of MoS_2 and WS_2 are 0.65 nm and 0.8 nm, respectively.

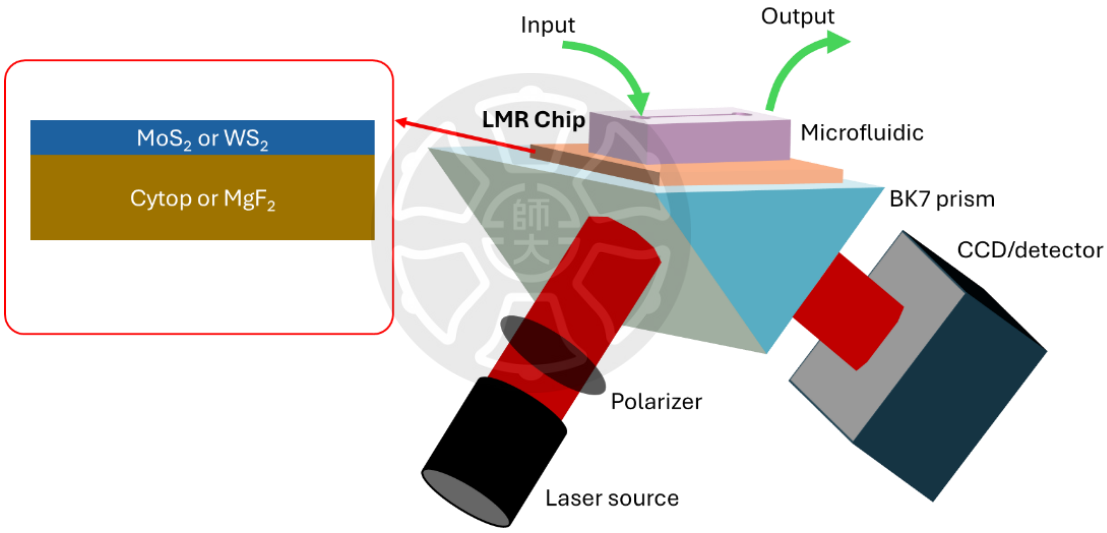

Figure 4. 5 The LMR sensor investigated in this study.

To predict the reflectance curves generated by LMR chips with different matching layer thickness, lossy layer and wavelength, the transfer matrix method has been used. Details related to the equations in the transfer matrix methods are shown in Appendix C. After optimization, the LMR signal quality is then evaluated based on several parameters, including minimum reflectance, FWHM, dip strength, sensitivity, and dynamic range of the sensor. The best performing LMR sensor is then tested in

the refractive index range of 1.33 to 1.5, and its performance is compared with the SPR sensor to assess its superiority.

4.3 Results and Discussions

4.3.1 Effect of polarization and wavelength on LMR signals

In some cases of LMR biosensors, the thickness of the matching layer is usually investigated at a thickness of ~1000 nm. Therefore, in the initial stage of our investigation we investigated the effect of different thicknesses of MoS_2 and WS_2 on the LMR chip built with 1000 nm Cytop. In addition, the resonance dip that is the focus of this paper is the resonance dip that exists after the critical angle (θ_c) which can be mathematically determined by the Snell equation, namely:

$$\theta_c = sin^{-1}\left(\frac{n_s}{n_p}\right) \quad \text{Eq. 4. 2}$$

In this case, n_s and n_p denote the refractive indices of sensing medium (water) and prism, respectively. From this equation, the critical angle is around ~61.54°.

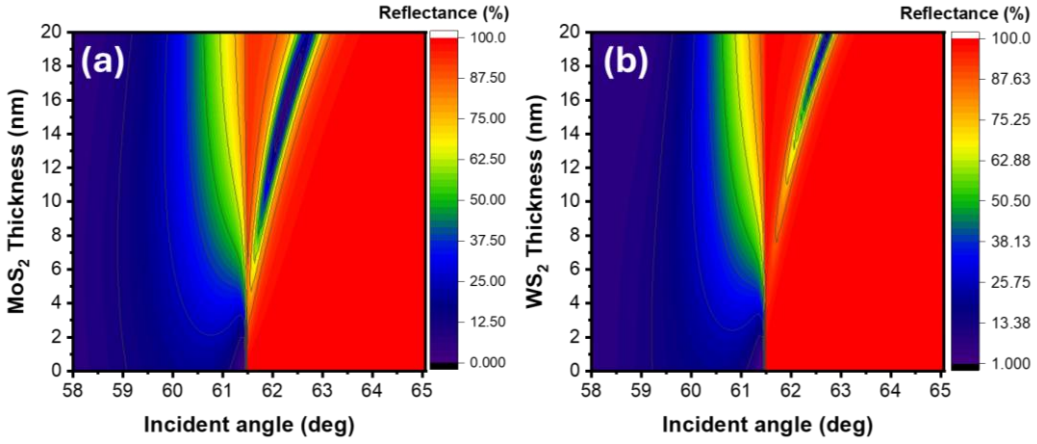

Figure 4. 6 Reflectance contour of (a) MoS_2 and (b) WS_2 based LMR sensor with 1000 nm Cytop and excited with 633 nm wavelength.

Figure 4. 6 shows the reflectance contours that illustrate how the thickness of MoS_2 and WS_2 affects the reflectance curve of the LMR biosensor. From the contours shown, it can be seen that for LMR sensors with p-polarized light, the resonance angle begins to be identified when the thickness of MoS_2 is ~6 nm. In addition, thicker MoS_2 and WS_2 layers have resulted in higher resonance angles.

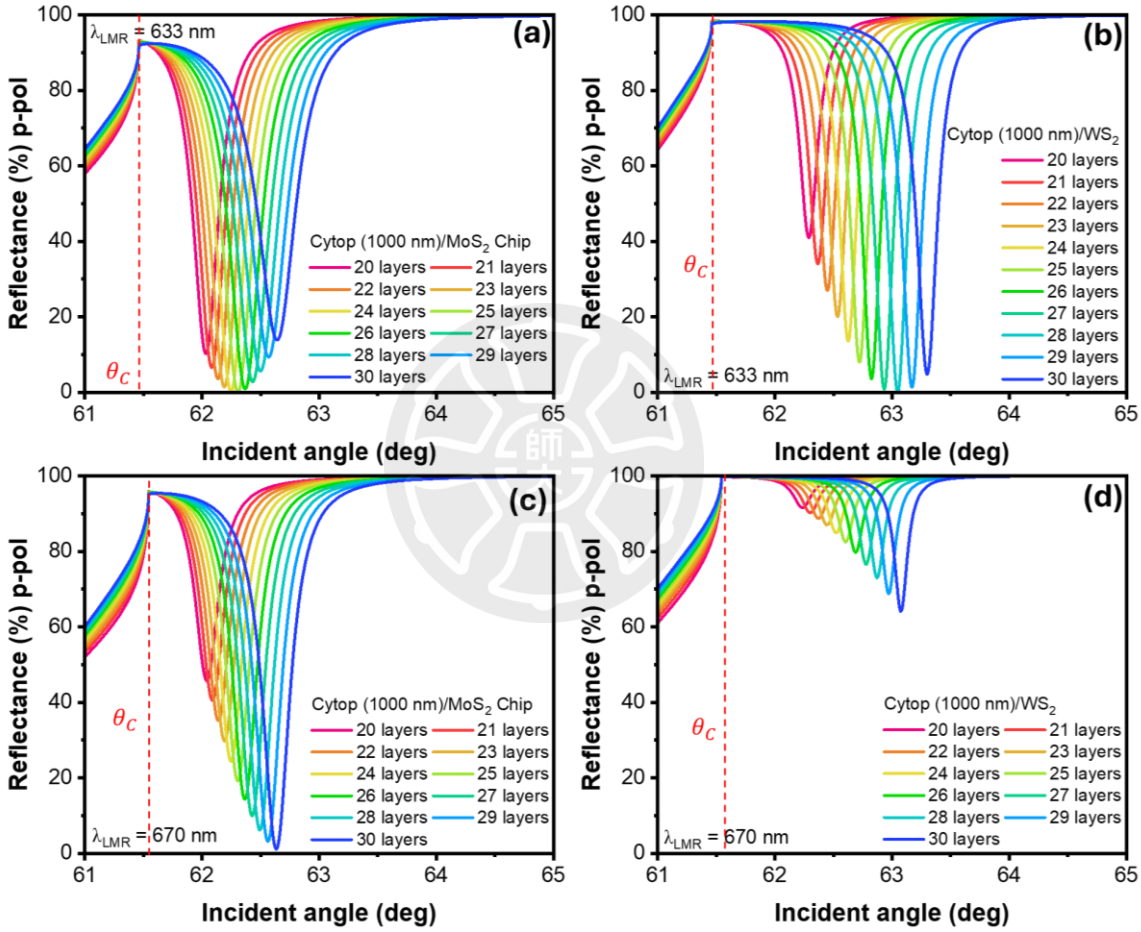

Figure 4. 7 Reflectance curves of (a) MoS_2 and (b) WS_2 based LMR sensors excited at 633 nm wavelength. Reflectance curves of (c) MoS_2 and (d) WS_2 based LMR sensors excited at 670 nm wavelength.

To prove the contour analysis above, the reflectance curve of LMR sensor with 1000 nm Cytop and different number of 2D material layers was performed. The results obtained are shown in Figure 4. 7. In this section, optimization is performed

where the minimum reflectance (R_{min}) at the resonance angle must be made as small as possible to obtain a good signal. From the data shown, for a chip excited at a wavelength of 633 nm, the chip with the smallest reflectance dip occurs when the number of MoS_2 and WS_2 layers is 25 and 28 layers, respectively. A different thing happens when the wavelength of the incident light is changed to 670 nm. More layers are needed to achieve optimum conditions. Even for WS_2 chips, the reflectance at the resonance angle is only 64.09% when the number of WS_2 layers is 30 layers.

Table 4. 3 Refractive index of 2D materials (MoS_2 and WS_2) and their n/k ratio at two different wavelengths

Materials	Wavelength	Refractive Index $\tilde{n} = n + ik$	n/k ratio
MoS_2	633 nm	$4.91 + 1.06i$	4.63
	670 nm	$5.44 + 0.572i$	9.51
WS_2	633 nm	$5.06 + 0.23i$	22.00
	670 nm	$4.72 + 0.03i$	157.33

The refractive index of a material is composed of the real part denoted by n and the imaginary part denoted by k. If the LMR properties are related to the refractive index of a 2D material then for the same thickness of the 2D material, a higher n/k ratio will produce a resonance with a higher minimum reflectance intensity. From the data shown in Table 4. 3, the optimum condition of the MoS_2-based LMR sensor with a wavelength of 633 nm is when the chip has 25 MoS_2 layers. In this condition, the n/k ratio is 4.63. When the excitation wavelength is changed to 670 nm, the reflectance intensity at the resonance angle increases from the initial 0.05% to 19.23%. This characteristic is more clearly observed in the WS_2-based LMR sensor where at a WS_2 thickness of 30 layers, the minimum reflectance increases

from the initial 4.80% at a wavelength of 633 nm to 64.09% at a wavelength of 670 nm.

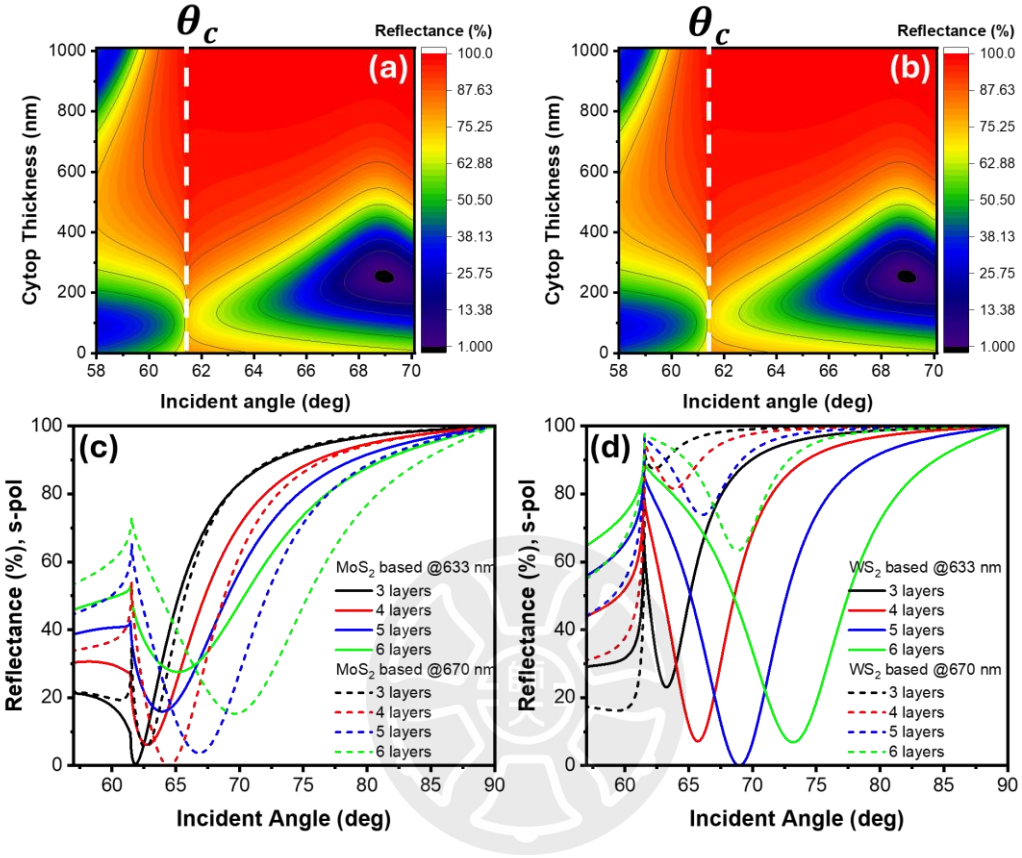

Figure 4. 8 Reflectance contour of LMR sensor with s-polarized light. (a) MoS_2 based (b) WS_2 based. Reflectance contours of (c) MoS_2 and (d) WS_2 chips excited at two different wavelengths.

With the same technique, contour analysis was performed to LMR biosensor with s-polarized light. Different thicknesses of cytop were varied up to 1000 nm thickness on LMR chip with monolayer of 2D material. The results obtained are shown in Figure 4. 8 (a) for MoS_2-based LMR sensor and Figure 4. 8 (b) for WS_2-based LMR sensor. From the contours shown, the resonance dip begins to form when the thickness of cytop is ~250 nm. If the optimization is carried out with the same criteria as the previous investigation, the optimum conditions of MoS_2-based LMR sensor with 250 nm cytop are 3 layers and 4 layers when the sensor is excited

with 633 nm and 670 nm wavelengths. For the WS_2-based LMR sensor, the optimum condition is 5 layers of WS_2 when the sensor is excited with a wavelength of 633 nm and 6 layers of WS_2 when the sensor is excited with a wavelength of 670 nm.

In short, the LMR signal excited with s-polarized light has the same characteristics as the LMR sensor excited with p-polarized light. A higher n/k ratio results in a higher damping effect and minimum reflectance. In both investigation results of LMR sensors with p- and s-polarized light, the LMR sensor chip with a smaller n/k ratio on the 2D material can produce resonance with a fewer number of 2D material layers.

MoS_2 and WS_2 are 2D transition metal dichalcogenides (TMDs) materials with extraordinary optical properties and most of their optical properties are dominated by excitons which are bound electron-hole pairs. This fact makes MoS_2 and WS_2 very interesting to be developed in various future technology products based on excitons. Therefore, to determine the contribution of excitons to the optical response of the LMR sensor, the absorbance of the LMR sensor at different wavelength and its relationship with the incident angle was carried out. For the LMR sensor with p-polarized light is represented by the LMR sensor with 1000 nm cytop and 25 layers of MoS_2 while for the LMR sensor with s-polarized light is represented by the LMR sensor with 250 nm cytop and 5 layers of WS_2.

Figure 4. 9 (a) presents two prominent absorption peaks corresponding to the wavelengths of A and B excitons in MoS_2. As the incident angle increases from 0° to 62.31°, the total absorption significantly rises, approaching near-perfect absorption. Additionally, the absorption peaks exhibit a noticeable spectral shift. A similar trend

is observed in the LMR chip with a WS_2-based lossy layer, as shown in Figure 4. 9 (b), where variations in the incident angle influence both the total absorption and the resonance position.

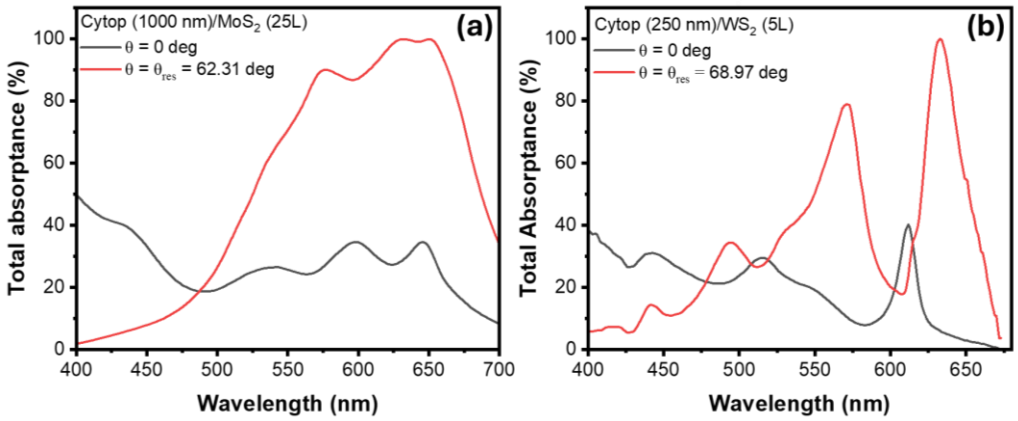

Figure 4. 9 Effect of wavelength and Incidence angle on the total absorbance of LMR sensor. (a) MoS_2-based sensor with p-polarized light (b) WS_2-based sensor with s-polarized light.

4.3.2 Signal quality of LMR biosensor

In the previous section, sensor optimization was performed based on the minimum reflectance value. In this section, the signal quality of each LMR chip is assessed based on the dip strength and FWHM. These two quantities are important parameters that reflect the performance of the sensor.

Dip strength refers to the minimum depth of the resonance curve in the reflectance spectra. This parameter refers to the difference in intensity between the off-resonance baseline (in this context, the intensity at the critical angle) and the minimum point on the resonance curve. Dip strength indicates the coupling efficiency between light and the modes supported by the lossy layer. Related to FWHM, this parameter relates to the width of the resonance curve at half the minimum dip depth.

A narrower FWHM indicates a sharp resonance and results in a sensor with better resolution and accuracy.

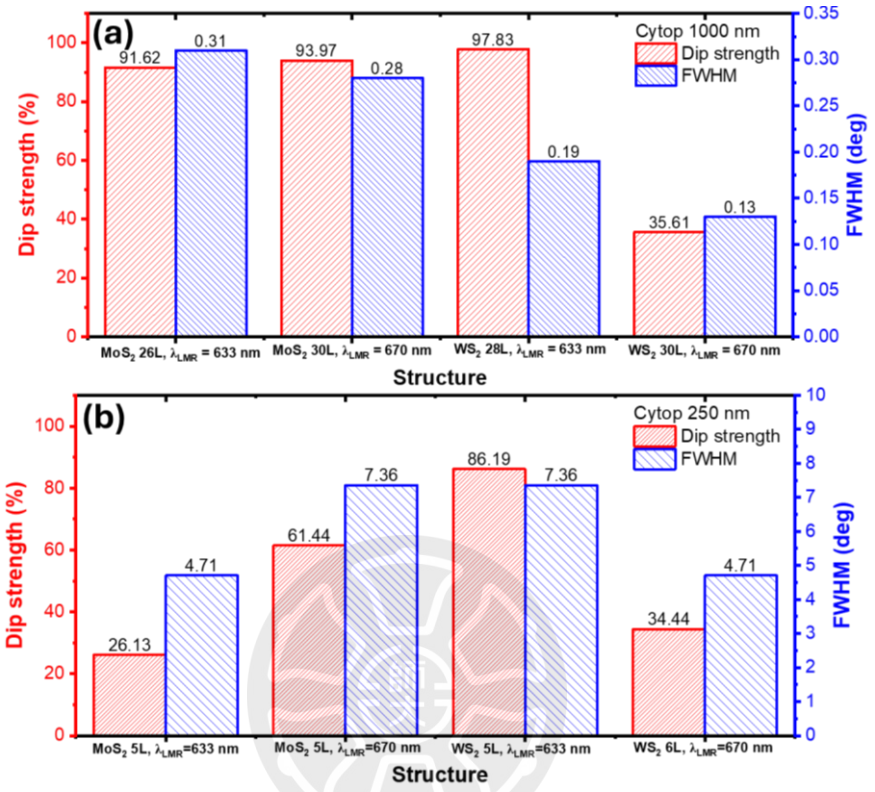

Figure 4. 10 Dip strength and FWHM of LMR sensor excited with (a) p-polarized light and (b) s-polarized light.

The data in Figure 4. 10 shows the difference in dip strength and FWHM values of the LMR sensor obtained from the optimization results in the previous section. From the data displayed by the LMR sensor with p-polarized light (top), the LMR sensor built from 1000 nm cytop and 28 layers of WS_2 displays the highest dip strength which reaches 97.83% compared to the other three configurations. This configuration also displays a narrower FWHM compared to the MoS_2-based LMR sensor. Because the WS_2-based LMR sensor excited with a wavelength of 670 nm displays too shallow a dip strength, the LMR sensor for next investigation was the WS_2-based LMR sensor with an excitation wavelength of 633 nm.

For LMR sensor with s-polarized light, the dip strength produced has a smaller intensity compared to LMR sensor with p-polarized light. It means that LMR sensor with p-polarized light shows better coupling effect. Of the four investigated structures, the highest dip strength is possessed by the chip with 250 nm cytop and 5 layers of WS_2 which reaches 86.19%. Compared with MoS_2-based chip, LMR sensor with 5 layers of WS_2 also shows a not too wide FWHM. Therefore, this structure has been selected to represent LMR sensor with s-polarized light to be tested at different refractive index of sensing medium.

4.3.3 LMR and SPR response at different refractive indices

In this study, the LMR sensor obtained from the optimization results will be tested for signal quality at different sensing medium refractive indices. Initially, the sensor will be tested at the sensing surface refractive index ranging from 1.331 to 1.401. The dynamic range of the LMR sensor is then compared with that of the SPR sensor over an extended refractive index range up to 1.5. The compared SPR sensor is a conventional chip composed of 2 nm Cr and 47 nm gold film.

Based on the sensor response shown in Figure 4. 11, the LMR sensor excited with p-polarized light shows poor stability. This is indicated by a significant increase in the minimum reflectance at the resonance angle as the refractive index of the sensing medium increases. For example, the reflection intensity at the resonance angle increases drastically from 2.17% (at a refractive index of 1.331) to 96.14% at a refractive index of 1.401. The dip strength of the LMR sensor becomes shallower

due to the higher refractive index of the sensing surface until it cannot be identified when the refractive index of the sensing surface is 1.5.

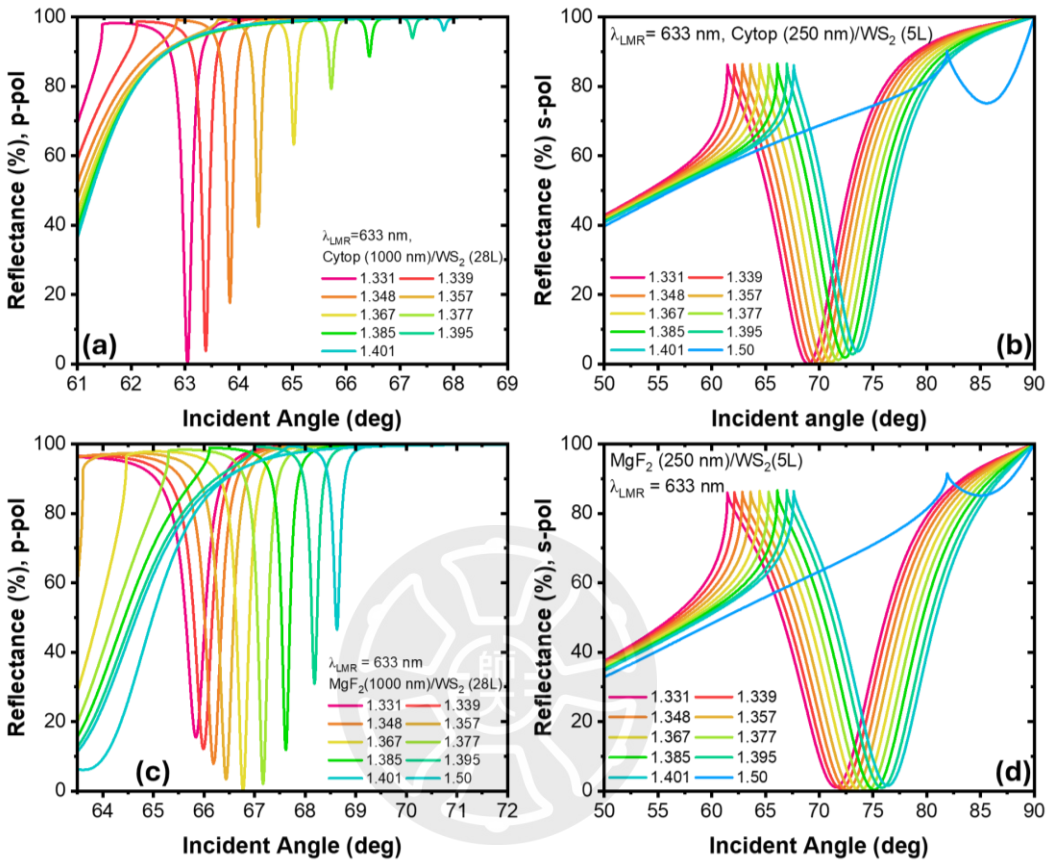

Figure 4. 11 Response of LMR sensor based on cytop as matching layer and excited with (a) p-polarized light and (b) s-polarized light. Response of LMR sensor based on MgF_2 as matching layer and excited with (c) p-polarized light and (d) s-polarized light.

Similar phenomena are also observed in sensors with varying Cytop layer thicknesses, specifically 800 nm and 1200 nm, as shown in Figures D1(a) and D1(b) in Appendix D. Notably, the dynamic range of the LMR sensor decreases with increasing Cytop thickness. This effect is particularly evident in the sensor with a 1200 nm Cytop layer, where resonance dips can only be identified when the refractive index of the sensing medium is ≤ 1.385. Comparable behavior is also found when the matching layer is replaced from Cytop to MgF_2, as illustrated in Figures D1(c) and

D1(d). In this configuration, the LMR signal still exhibits poor stability, marked by a significant increase in minimum reflectance. Overall, LMR sensors excited with p-polarized light demonstrate limited detection range and poor signal stability under these configurations. Therefore, based on the computational results, such sensor designs are not recommended for practical sensing applications.

In contrast, a different phenomenon was shown by the LMR sensor excited with s-polarized light. This sensor, with both cytop and MgF_2 matching layers, showed better signal stability. The reflectance intensity at the resonance angle could be maintained below 10%, and the resonance angle was still identifiable even though the refractive index of the sensing surface was expanded to 1.5. Signal stability was also observed in matching layers with different thicknesses, namely 200 nm and 300 nm. The optimum condition for the LMR sensor with a cytop thickness of 200 nm was 6 layers, while for a cytop thickness of 300 nm it was 4 layers, as shown in Figure D2 in Appendix D. These data indicate that the LMR sensor excited with s-polarized light has better signal stability and wider dynamic range compared with the sensor excited with p-polarized light. Therefore, the LMR sensor with this configuration is more recommended for application in analyte sensing than the LMR sensor with p-polarized light.

When compared with the quality of the SPR sensor, the data in Figure 4. 12 shows that the SPR sensor excited with a wavelength of 633 nm has poor signal stability. This is indicated by an increase in the reflectance intensity at the resonance angle when the refractive index of the sensing surface exceeds 1.377. Even at a refractive index of 1.401, the reflectance intensity at the resonance angle increases

by 50%. In contrast, the SPR sensor excited with a wavelength of 670 nm shows a more stable signal, with the reflectance intensity at the resonance angle still being maintained below 10%. However, when compared with the dynamic range of the LMR sensor, the SPR sensor has a narrower detection range. Whether excited with a wavelength of 633 nm or 670 nm, the resonance angle of the SPR sensor cannot be identified when the refractive index of the sensing surface reaches 1.5. These results indicate that the LMR sensor proposed in this study has better signal stability and a wider detection range than the SPR sensor. Therefore, this LMR sensor has great potential to be further developed in experiments as an alternative to SPR sensors which are highly dependent on gold as their main transducer material.

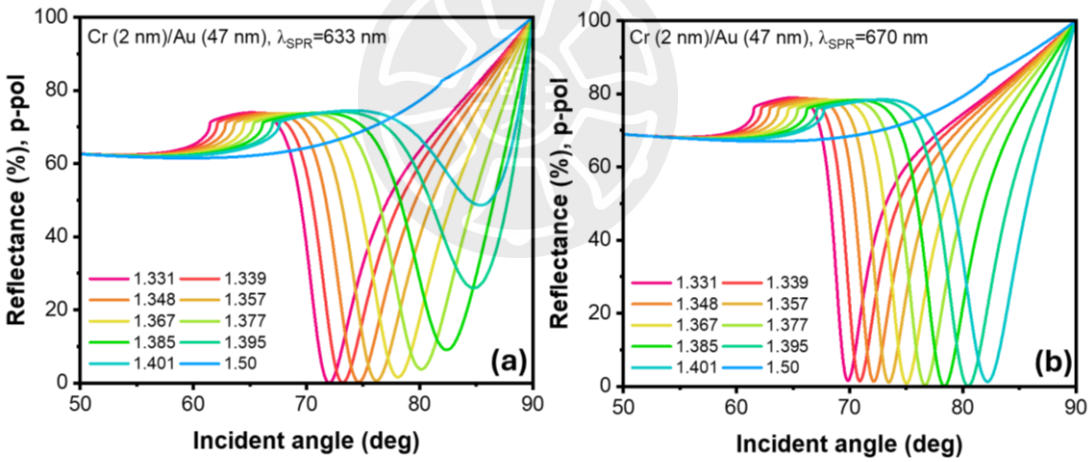

Figure 4. 12 Response of SPR sensor excited with wavelengths of (a) 633 nm and (b) 670 nm.

To complete this study, a comparison of the sensitivity and dynamic range of the various sensor structures investigated by the authors is presented, as summarized in Figure 4. 4. All compared configurations are based on the authors' own simulation results. The data indicate that the structure incorporating a graphene lossy layer exhibits both low sensitivity and a limited dynamic range. In contrast, the

structure using MoS_2 as the lossy layer shows a comparable dynamic range for both p- and s-polarized light excitation. However, it is important to note that the signal quality of the MoS_2-based LMR sensor under p-polarized excitation demonstrates poor stability. Overall, the WS_2-based LMR sensor whether paired with MgF_2 or Cytop as the matching layer exhibits a wide dynamic range, extending up to a refractive index of 1.5, along with higher sensitivity. These characteristics suggest strong potential for further development and validation through experimental implementation.

Table 4. 4 Summary of the dynamic range and sensitivity of various LMR sensors that have been investigated by author.

Structure	Polarization	Dynamic range	Sensitivity (º/RIU)	Ref
BK7/MgF_2/Graphene	s-pol	1.331 – 1.385	66.17	(Nurrohman & Chiu, 2024a)
BK7/MgF_2/MoS_2	s-pol	1.331 – 1.401	70.37	(Nurrohman & Chiu, 2024a)
BK7/Cytop/MoS_2	s-pol	1.331 – 1.401	72.13	(Nurrohman & Chiu, 2024b)
BK7/Cytop/MoS_2	p-pol	1.331 – 1.401	70.67	(Nurrohman & Chiu, 2024b)
BK7/MgF_2/WS_2	s-pol	1.331 – 1.5	106.38	This work
BK7/Cytop/WS_2	s-pol	1.331 – 1.5	98.19	This work

4.3.4 Penetration depth of LMR and SPR sensors

In addition to dip strength and FWHM, another parameter that can be used to assess the performance of the LMR sensor is the penetration depth. This parameter is very important to ensure that the electromagnetic field can reach the target without reducing the sensitivity and specificity of the sensor. The sensor penetration depth that is too shallow causes the target to not be detected perfectly and the measured signal only comes from a small part of the target (Shrivastav et al., 2021). This parameter can be calculated from the distance where the intensity of the

electromagnetic field generated by resonance (SPR or LMR) decreases exponentially to about 1/e (~37%) of its maximum value.

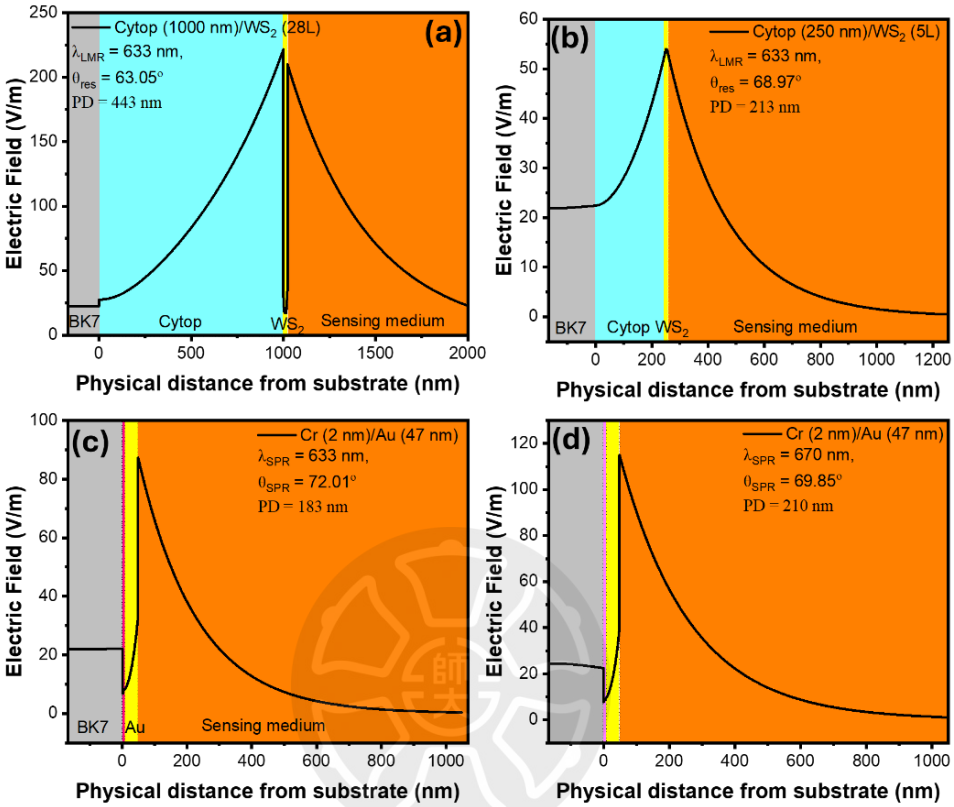

Figure 4. 13 Electromagnetic field of LMR sensor with (a) p-polarized and (b) s-polarized light. The electromagnetic field of SPR sensor excited with wavelength of (c) 633 nm and (d) 670 nm.

Figure 4. 13 shows the electromagnetic field profiles of the LMR and SPR sensors from the BK7 substrate to the sensing surface (water) taken at their resonance angles (θ_{res}). For the LMR sensor with p-polarized light is shown in Figure 4. 13 (a) where the highest electric field at the boundary between WS_2 and the sensing surface is 210 V/m. It means that 37% of the highest electric field is about 77 V/m so that the penetration depth of the LMR sensor with p-polarized light is 443 nm. Using the same steps, the penetration depth of the LMR sensor excited with s-polarized light and SPR sensor is determined. The results showed that the penetration depth for the LMR sensor with s-polarized light was 213 nm, while for the

SPR sensor at wavelengths of 633 nm and 670 nm were 183 nm and 210 nm, respectively. The LMR sensor excited by p-polarized light had the highest penetration depth compared to the other three sensors.

For the LMR sensor with s-polarized light, the penetration depth was greater than the SPR sensor at a wavelength of 633 nm, and slightly greater than the SPR sensor at a wavelength of 670 nm. These findings indicate that in addition to having a wider dynamic range, the LMR sensor also offers a higher penetration depth, so it has the potential to be applied in various types of detection ranging from nano to micro scales.

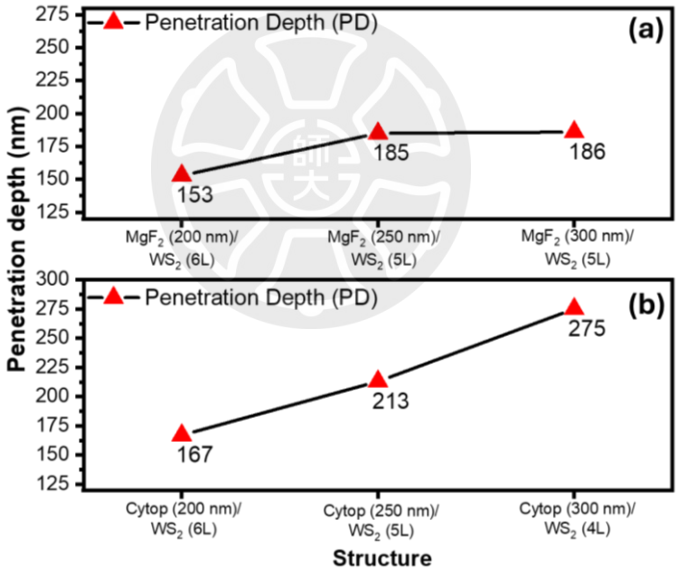

Figure 4. 14 Penetration depth of LMR sensor excited with s-polarized light on chips with different thicknesses of matching layer and lossy layer. (a) MgF_2-based chip (b) Cytop-based chip.

Since the penetration depth of the LMR sensor with s-polarized light is still comparable to that of the SPR sensor, further investigations were carried out to understand the effect of the thickness of the matching layer and the lossy layer on

the penetration depth of the LMR sensor. The three thicknesses of the matching layers analyzed were 200 nm, 250 nm, and 300 nm.

The optimization results show the thickness of each material and its penetration depth, as shown in Figure 4. 14. This study revealed that the LMR sensor with a thinner matching layer has a shallower penetration depth, while the sensor with a thicker matching layer shows a greater penetration depth. Compared with other sensors, the LMR sensor using the Cytop layer achieved the highest penetration depth of 275 nm, far exceeding the LMR sensor with a MgF_2 layer which has a depth of 186 nm, and the SPR sensor which only reached 210 nm.

4.4 Conclusions

This study has numerically investigated MoS_2 and WS_2-based LMR sensors. Two different structures, namely MoS_2 chip and WS_2 chip, are compared based on their reflectance curve quality and performance at various refractive indices of sensing media. The results show that WS_2-based LMR sensors excited with s-polarized light have better reflectance curve quality and wider detection range. Similar characteristics are also shown by LMR sensors with MgF_2 matching layer. When Cytop and MgF_2-based LMR sensors are compared, the sensitivity of the sensors is 98.19°/RIU and 106.38°/RIU, respectively. Compared with conventional SPR sensors, the proposed WS_2-based structures offer wider dynamic measurement range up to refractive index 1.5 and better penetration depth. This finding makes LMR sensors a potential candidate to replace SPR biosensors, which rely heavily on gold as their plasmonic material.

Chapter 5

Conclusion and Recommendations

5.1 Conclusion

Computational and experimental approaches have been used to investigate optical resonance biosensors, ranging from LSPR-based biosensors to SPR-Raman integration and LMR metal-free biosensors. In the LSPR biosensor study, the investigation focused on a 15 nm AuNPs-based LSPR immunosensor used to detect BSA. Computational results showed an enhancement in the electric field caused by the dielectric layer on the nanoparticle surface. This enhancement in the electric field results in a limited detection range of the LSPR sensor due to the Hook effect. Previously, the Hook effect has also been observed in larger AuNPs nanoparticle sizes, namely 35 nm in the case of 17β-estradiol (E2) detection and 40 nm in the case of human immunoglobulin G (IgG) detection. The fact that the Hook effect phenomenon occurs in AuNPs with different sizes provides a comprehensive understanding that this phenomenon is inevitable and the linearity of the LSPR sensor is limited, therefore, it is very important to know the Hook point of each detected analyte.

The second topic explores the integration of 1D grating-based SPR with Raman spectroscopy. This study demonstrates the potential of SPR-Raman integration for specific molecule detection with high sensitivity and spectral identification (molecular fingerprinting) capability. Two grating periods were examined: 400 nm and 800 nm. The SPR mode was only observed in the chip with the larger grating period. Reflectance map analysis revealed that under 670 nm wavelength excitation, SPR modes emerge when the grating period exceeds approximately 644 nm. In contrast, for the chip with the smaller grating period (400 nm), the observed resonance is predominantly attributed to cavity modes. Experimental results further demonstrate that the Raman signal can be enhanced through the amplification of the local electric field generated by the SPR phenomenon. However, the Raman measurements in this study still require relatively high excitation power (up to 65 mW). To enhance the Raman signal while reducing the required power, it is suggested to modify the grating chip, for instance by incorporating metal nanoparticles, which can further boost the plasmonic effect.

For the LMR metal-free sensor, the structure proposed in this study is composed of Cytop or MgF_2 as the matching layer and 2D materials (MoS_2 and WS_2) as its lossy layer. From the results of the computational study, the LMR sensor with the proposed structure has good signal stability with a wider detection range even exceeding the SPR sensor. The LMR sensor excited by s-polarized light can be utilized for quantification of analytes up to a refractive index of 1.5.

5.2 Sensor Performance Comparison

Resonance-based optical sensors have become one of the promising approaches in developing sensitive, rapid, and label-free chemical and biological detection systems. Among

these approaches, LSPR, SPR, and LMR offer different but complementary detection mechanisms in terms of performance characteristics, application areas, and device architecture. Therefore, to provide a more comprehensive overview of these three types of sensors, the performance of the three sensors is compared based on various technical parameters such as penetration depth, sensitivity, FoM, spectral resolution, cost and others. The comparison is presented in Table 5. 1 below:

Table 5. 1 Performance comparison of LSPR, SPR-Raman and LMR sensors

Parameters	**LSPR**	**SPR/Raman**	**LMR**
Field penetration depth	~ 5–24 nm (depends on the size and inter particle distance of the nanoparticles (Semwal et al., 2023))	~200–300 nm (depends on wavelength and structure (Maurya et al., 2023))	~150–275 nm (depends on wavelength and structure)
Refractive Index Sensitivity	Low–Medium (high only on the surface of nanoparticles)	High	High
Figure of Merit (FoM)	Medium (affected by spectral peak width)	High (when combined with sharp Raman spectrum)	High–very high (depending on the type of polarization used)
Spectral resolution	Medium (generally has a wider FWHM)	Higher than LSPR sensor	Very high (LMR peak is very narrow) (Nurrohman & Chiu, 2024b)
Specificity	High (due to high localization field)	Height (when combined with Raman fingerprint)	Medium–high
Chip fabrication costs	cheap	Medium – expensive	Medium – expensive
Optical set-up	Simple (can be sufficient with a UV-Vis spectrometer)	Complex (requires SPR/Raman setup)	Complex (requires LMR setup)
Suitable for POC (Point of Care)	Very suitable	Less suitable (large and complex)	Less suitable (large and complex)

In terms of sensitivity, the three sensors (LSPR, SPR, and LMR) have different electromagnetic field characteristics at their resonance conditions. In the LSPR sensor, the electromagnetic field is highly localized around the surface of the metal nanoparticles. Several reports state that the field penetration depth is only around 5 to 24 nm (Semwal et al., 2023)(H. Wang et al., 2023), making it very sensitive to events that occur right on the surface of the nanoparticles, such as the attachment of target molecules (Semwal et al., 2023). In contrast, in the SPR and LMR sensors, the electromagnetic field has a much deeper penetration range into the dielectric medium. Based on the simulation results in this study, the conventional SPR sensor excited at a wavelength of 670 nm has a field penetration depth of 210 nm, while in the LMR sensor based on the cytop/WS_2 structure, the penetration depth is even greater, which is around 275 nm. This higher penetration depth allows SPR and LMR to be more sensitive to refractive index changes in a larger volume, not just on the surface. For example, in the detection of exosomes with diameters between 30 and 200 nm (Gurung et al., 2021), SPR and LMR sensors are more promising because the size of the analyte is comparable to the effective detection zone of its electromagnetic field.

In terms of interrogation mode, LSPR generally only allows analyte quantification through wavelength interrogation mode. Meanwhile, SPR and LMR sensors offer higher flexibility, because they can be utilized in wavelength (Long et al., 2020)(B. Li et al., 2025), angle (Vala et al., 2010)(Wu et al., 2018), and phase/polarization interrogation modes (Ruffato et al., 2013), thus opening up opportunities for optimizing sensor performance from various aspects. When compared in terms of sensitivity, the SPR grating chip used in this study showed a sensitivity of 83.81°/RIU, a lower value compared to the LMR sensor. However, the SPR system combined with the Raman scattering technique offers better

specificity, especially in applications that require structural identification of molecules. In simple, it can be concluded that LSPR excels in local detection on a nanometer scale, while SPR and LMR offer high sensitivity to refractive index variations on a larger scale and flexibility in detection methods.

In terms of cost and application area, LSPR sensors have advantages in terms of ease and efficiency of fabrication. LSPR transducers are generally based on AuNPs which can be synthesized through simple chemical reduction methods, such as the Turkevich method. The size of AuNPs can be controlled relatively easily by adjusting the precursor concentration ($HAuCl_4$), reaction temperature, and reaction time (Bilal & Bandyopadhyay, 2025). In this study, the LSPR signal was obtained from measurements using a UV-Vis spectrophotometer. However, the LSPR signal can also be observed visually through changes in the color of the nanoparticle solution due to the presence of the target analyte (Aldewachi et al., 2018). These characteristics make LSPR a low-cost, easy-to-operate sensor, and very suitable for applications in Point-of-Care (POC) and environments with limited resources. In contrast, SPR and LMR sensors require more complex fabrication processes and higher costs. In this study, the grating chip for SPR was fabricated using the Electron Beam Lithography technique which requires high-precision equipment. For LMR sensors based on 2D materials such as MoS_2 or WS_2, a Chemical Vapor Deposition (CVD) process and material transfer steps to the target substrate are required, which adds to the complexity of the process. In addition, SPR and LMR sensors generally require larger optical systems and more precise setups, making them more suitable for use in laboratory or controlled testing environments. Thus, in terms of cost and implementation potential, LSPR

is superior for portable and field applications, while SPR and LMR are more suitable for applications that require high accuracy and tight control of experimental parameters.

5.3 Further Research Recommendations

5.3.1 Recommendations for LSPR sensors

The LSPR biosensor in this study utilized ~15 nm AuNPs to detect BSA, with anti-BSA antibody as the recognition element. This nanoparticle size was chosen because its optical properties are dominated by absorption and extinction, while its scattering contribution is very small (Jain et al., 2006). This characteristic makes absorbance-based measurement using UV-Vis spectrophotometers as an ideal method. In this research, the Hook point was observed at a BSA concentration of around 10 µg/mL, with a linear range of the sensor from 1 ng/mL to 10 μg/mL.

AuNPs with a size of 15 - 20 nm have been widely used in various studies, such as for the detection of hepatitis B surface antigen (HBsAg), and methamphetamine (J. Kim et al., 2018)(Qadami et al., 2018). Meanwhile, larger AuNPs, such as 40 nm, are known to have an optimal balance between absorption and scattering, thus providing optimal LSPR signals. However, several studies have also reported the emergence of the Hook effect at this size, indicating that this phenomenon is difficult to avoid in nanoparticle-based LSPR sensors (Iarossi et al., 2018)(Minopoli et al., 2020).

Based on these findings, it is recommended for further research to explore the use of AuNPs with a size of > 40 nm, whose optical properties are dominated by scattering. However, because scattering dominates, the detection method as carried out in this study which uses absorbance measurements seems no longer ideal. Instead, scattering-based

detection techniques such as dark-field microscopy (DFM) seem more recommended. With this approach, it is expected to develop LSPR sensors that not only have high sensitivity, but also have a wider linear range and resistance to the Hook effect.

5.3.2 Recommendations for Integrated SPR/Raman

The analysis of the reflectance map in Chapter 3 reveals that the SPR mode starts to form in the 1D grating chip structure when the grating period exceeds 644 nm. For chips with smaller periods, the observed resonance is primarily dominated by the cavity mode. Experimental results also demonstrate that SPR excitation generates a significant local electric field, which enhances the Raman signal intensity. However, clear identification of the R6G peak characteristics is only possible when the excitation power reaches 65 mW. This power level is still relatively high, indicating the need for optimization of the 1D grating chip structure to achieve a high Raman signal even with lower excitation power.

Therefore, future research should be directed at modifying the grating structure, such as by adding nanoparticles to the grating to increase the intensity of electromagnetic hot spots. This strategy is expected to improve the excitation efficiency of target molecules by strengthening the local field. As a reference, research by Driskell et al. has shown that the addition of AuNPs to a gold thin film substrate, with varying nanoparticle sizes, can increase the intensity of the Raman signal (Driskell et al., 2006). Based on the peak characteristics shown in Figure 5. 1, the gold substrate coated with AuNPs with a larger size produces a higher Raman peak intensity. This proves that the addition of AuNPs to the gold substrate has a significant effect on the amplification of the Raman signal.

However, in the context of an integrated SPR/Raman system, the addition of nanoparticles with too high concentration or too large size can interfere with the SPR sensor

signal. Therefore, the concentration and size of nanoparticles need to be optimized to enhance the Raman signal without sacrificing the SPR signal. This approach enables the proposed SPR/Raman system to work synergistically and effectively in detecting and analyzing target molecules, especially for biosensing applications that require high sensitivity and accuracy.

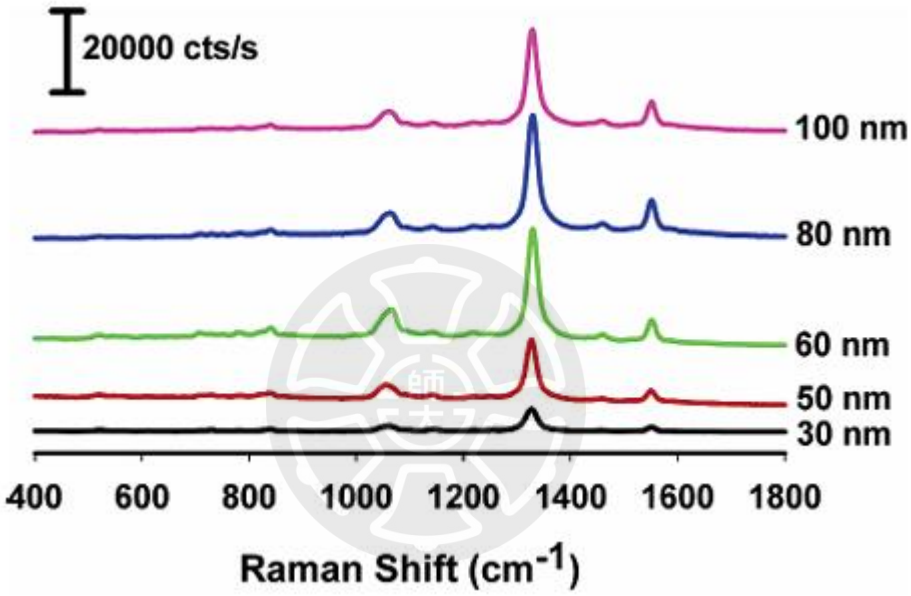

Figure 5. 1 Raman spectra for different sizes of 5,5'-dithiobis(succinimidyl-2-nitrobenzoate) (DSNB)-labeled AuNPs immobilized on gold substrate with 2-aminoethanethiol hydrochloride. Adapted with permission from Ref. (Driskell et al., 2006)*, copyright American Chemical Society.*

In the future, the direction of research needs to be focused on the design and optimization of hybrid structures between plasmonic gratings and nanoparticles to maximize Raman detection performance, especially under low excitation power conditions. In addition, the integration of machine learning technology can be utilized to process spectrum data more intelligently and automatically, such as in spectral pattern classification (A. Kumar et al., 2024), or noise elimination (Y. Jia et al., 2024). With the application of machine learning

algorithms, integrated SPR/Raman sensors can be developed into more adaptive, accurate, and efficient detection systems in various environmental conditions and sample variations.

Overall, these steps are expected to bring significant improvements in the performance of SPR/Raman-based sensors, making them more ready to be applied to biomolecule detection in the medical, environmental, and food safety fields with higher sensitivity and better reliability.

5.3.3 Recommendations for LMR Metal-free Sensors

In the case of metal-free LMR sensors, numerical simulations have demonstrated that this sensor type offers excellent signal stability and a broad detection range. However, to fully realize this potential, further experimental validation is required. As a step toward implementation, this section provides recommendations on suitable fabrication techniques for constructing LMR sensors composed of BK7 glass as the substrate, MgF_2 or Cytop as matching layers, and MoS_2 or WS_2 as lossy layers. In this study, MgF_2 and Cytop were evaluated as candidate materials for the matching layer. MgF_2 thin films can be fabricated using sputtering techniques. On the other hand, Cytop thin films are easier to fabricate, offering a more practical approach for experimental realization. The spin coating technique is particularly well-suited for applying Cytop onto BK7 substrates, as it allows precise control of film thickness through adjustments in spin speed and solution concentration. The experimental procedures for fabricating Cytop thin films are briefly outlined in the references provided below (Heo, 2020).

To obtain MoS_2 or WS_2 with varying thickness or number of layers, several techniques can be used, including spin coating and Chemical Vapor Deposition (CVD). However, based on several literatures, the fabrication process using these two techniques generally requires

high temperatures during the experiment (Das et al., 2020)(Kwack et al., 2021). Therefore, a transfer process is needed to move the 2D material to the LMR sensor chip substrate, which in this study uses BK7 glass.

In this section, two studies are highlighted that employed spin coating and CVD methods, along with their respective transfer techniques to target substrates. The first study, conducted by Yang et al., demonstrated the fabrication of MoS_2 films with varying layer numbers using a polymer-assisted deposition method, followed by thermolysis at a relatively low temperature without sulfurization (H. Yang et al., 2017). The fabrication process began with the preparation of a precursor–polymer complex thin film, consisting of anhydrous ammonium tetrathiomolybdate (ATM) as the precursor and linear poly(ethylenimine) (L-PEI) as the supporting polymer. In this method, the polymer facilitates uniform coating over a large area while retaining moisture during film formation. To avoid aggregation in the solution phase, ethanolamine was added to the complex solution to help dissolve any precursor aggregates. Subsequently, thermolysis was performed at 700 °C under an inert atmosphere of 4% H_2 and 96% Ar, without the need for an additional sulfur source, resulting in the formation of MoS_2 thin films. A summary of the experimental procedure and the resulting film quality is presented in Figure 5. 2 (a).

To transfer MoS_2 or WS_2 films onto desired substrates, a surface energy-assisted transfer technique can be employed. In one study, Gurarslan et al. successfully transferred MoS_2 films grown via the CVD method on sapphire substrates to arbitrary target substrates using this technique (Gurarslan et al., 2014). A brief illustration of the process is shown in Figure 5. 2 (b). In this method, 9 g of polystyrene (PS) was dissolved in 100 mL of toluene, and the resulting solution was spin-coated onto the MoS_2 film at 3500 rpm for 60 seconds.

The sample was then baked to enhance the adhesion between the PS layer and the MoS_2 film. Subsequently, water droplets were introduced onto the surface. Once the PS layer was gently scratched from its edge, water molecules infiltrated the interface, leading to delamination of the PS–MoS_2 assembly. This detached film could then be retrieved using tweezers and transferred onto a new substrate. In a related study, Gurarslan et al. reported that this surface energy-assisted transfer technique is broadly applicable and can also be used for transferring other 2D materials, such as WS_2.

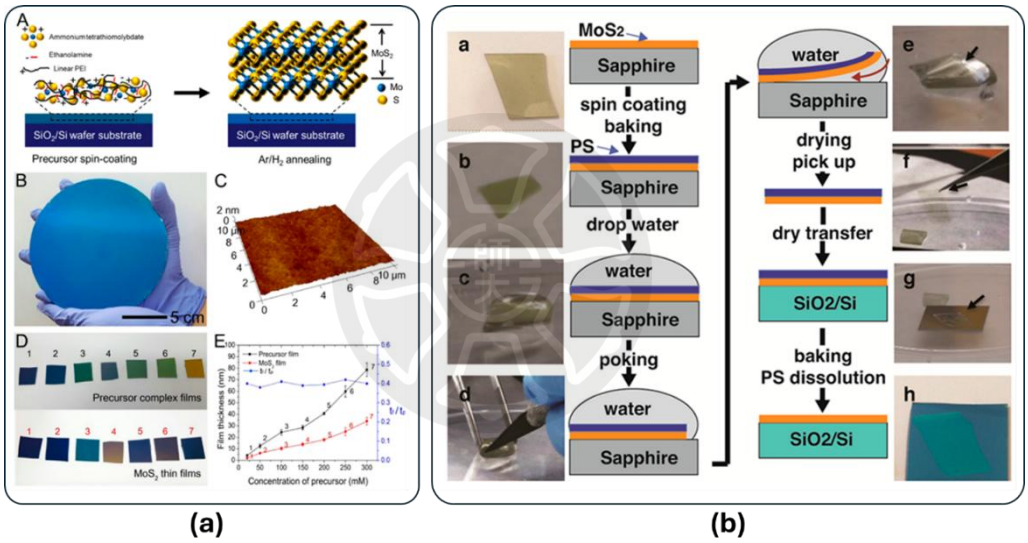

Figure 5. 2 (a) Fabrication of different thicknesses of MoS_2 by spin coating method (b) Surface energy assisted transfer technique to transfer MoS_2 films onto target substrates. Figure composed of elements reproduced from Ref. (H. Yang et al., 2017) *(licensed under CC BY 4.0) and Ref.* (Gurarslan et al., 2014) *(with permission from American Chemical Society).*

Up to this point, the fabrication of matching layers and lossy thin films has been discussed, along with the transfer techniques for MoS_2 and WS_2 onto LMR substrates. To further implement this LMR chip as a functional biosensor, biorecognition elements need to be immobilized on the chip surface using suitable linker molecules. In this context, the sulfur vacancies present on MoS_2 and WS_2 surfaces can be strategically utilized to facilitate the immobilization process, enabling specific interactions with target biomolecules. The detailed

discussion regarding the utilization of sulfur vacancies for molecular immobilization can be found in the following paper (Chiu et al., 2021).

References

Akila, C., Dhatchayani, M., Diwan, A., Shekhawat, A. S., Sharma, S., Srivastava, T., Kumar, R., Saxena, S. K., & Shrivastav, A. M. (2024). Tailoring LRSPR penetration depth employing 2D material at visible and IR range. *IEEE Sensors Journal*, *24*(21), 34265–34272. https://doi.org/10.1109/JSEN.2024.3443631

Akins, D. L., Özçelik, S., Zhu, H.-R., & Guo, C. (1997). Aggregation-Enhanced Raman Scattering of a Cyanine Dye in Homogeneous Solution. *The Journal of Physical Chemistry A*, *101*(18), 3251–3259. https://doi.org/10.1021/jp963122f

Al-Jarwany, Q. A., Habeeb, S. A., Bakly, A. A. K., & Walton, C. D. (2024). Fabrication and Fluorescence Analysis of Rhodamine Dyes in Polycarbonate Serpentine Microfluidic System. *Journal of Fluorescence*, *0123456789*. https://doi.org/10.1007/s10895-024-03984-3

Aldewachi, H., Chalati, T., Woodroofe, M. N., Bricklebank, N., Sharrack, B., & Gardiner, P. (2018). Gold nanoparticle-based colorimetric biosensors. *Nanoscale*, *10*(1), 18–33. https://doi.org/10.1039/c7nr06367a

Artemyev, D. N., & Shatskaya, A. A. (2022). Study of spurious optical signals in a fiber-optic Raman spectroscopy system. *Optics and Laser Technology*, *152*(July 2021), 108184. https://doi.org/10.1016/j.optlastec.2022.108184

Bahri, M., Yu, D., Zhang, C. Y., Chen, Z., Yang, C., Douadji, L., & Qin, P. (2024). Unleashing the potential of tungsten disulfide: Current trends in biosensing and nanomedicine applications. *Heliyon*, *10*(2), e24427. https://doi.org/10.1016/j.heliyon.2024.e24427

Bartolowits, M. D., Xin, M., Petrov, D. P., Tague, T. J., & Davisson, V. J. (2019). Multimeric Rhodamine Dye-Induced Aggregation of Silver Nanoparticles for Surface-Enhanced Raman Scattering. *ACS Omega*, *4*(1), 140–145. https://doi.org/10.1021/acsomega.8b02970

Bhakta, S. A., Evans, E., Benavidez, T. E., & Garcia, C. D. (2015). Protein adsorption onto nanomaterials for the development of biosensors and analytical devices: A review. *Analytica Chimica Acta*, *872*, 7–25. https://doi.org/10.1016/j.aca.2014.10.031

Bhaskar, S., Visweswar Kambhampati, N. S., Ganesh, K. M., Pa, M. S., Srinivasan, V., & Ramamurthy, S. S. (2021). Metal-Free, Graphene Oxide-Based Tunable Soliton and Plasmon Engineering for Biosensing Applications. *ACS Applied Materials and Interfaces*, *13*(14), 17046–17061. https://doi.org/10.1021/acsami.1c01024

Bijalwan, A., & Rastogi, V. (2017). Sensitivity enhancement of a conventional gold grating assisted surface plasmon resonance sensor by using a bimetallic configuration. *Applied Optics*, *56*(35), 9606. https://doi.org/10.1364/AO.56.009606

Bilal, M., & Bandyopadhyay, S. (2025). Controlled growth of citrate-stabilized gold nanoparticles using a semi-continuous seed-mediated route. *Discover Nano*, *20*(1), 39. https://doi.org/10.1186/s11671-025-04189-8

Cao, K., Wu, M., Wang, E., Liu, C., Zhu, H., Ma, C., & Cao, J. (2024). Dual-mode SPR/SERS biosensor utilizing metal nanogratings fabricated via wet etching-assisted direct laser interference patterning. *Applied Surface Science*, *655*(November 2023), 159621. https://doi.org/10.1016/j.apsusc.2024.159621

Cavalera, S., Pezzoni, G., Grazioli, S., Brocchi, E., Baselli, S., Lelli, D., Colitti, B., Serra, T., Di Nardo, F., Chiarello, M., Testa, V., Rosati, S., Baggiani, C., & Anfossi, L. (2022). Investigation of the “Antigen Hook Effect” in Lateral Flow Sandwich Immunoassay: The Case of Lumpy Skin Disease Virus Detection. *Biosensors*, *12*(9). https://doi.org/10.3390/bios12090739

Chang, K., Wang, S., Zhang, H., Guo, Q., Hu, X., Lin, Z., Sun, H., Jiang, M., & Hu, J. (2017). Colorimetric detection of melamine in milk by using gold nanoparticles-based LSPR via optical fibers. *PLoS ONE*, *12*(5), 1–12. https://doi.org/10.1371/journal.pone.0177131

Chen, C., Caucheteur, C., Voisin, V., Albert, J., & Berini, P. (2014). Long-range surface plasmons on gold-coated single-mode fibers. *Journal of the Optical Society of America B*, *31*(10), 2354. https://doi.org/10.1364/JOSAB.31.002354

Chen, J., Shi, S., Su, R., Qi, W., Huang, R., Wang, M., Wang, L., & He, Z. (2015). Optimization and application of reflective LSPR optical fiber biosensors based on silver nanoparticles. *Sensors (Switzerland)*, *15*(6), 12205–12217. https://doi.org/10.3390/s150612205

Chen, S., Zong, X., Zheng, J., Zhang, J., Zhou, M., Chen, Q., Man, C., & Jiang, Y. (2021). A colorimetric strategy based on aptamer-catalyzed hairpin assembly for the on-site detection of salmonella typhimurium in milk. *Foods*, *10*(11). https://doi.org/10.3390/foods10112539

Chen, W., Guo, L., & Sun, Z. (2014). Resonant Absorption of TE-Polarized Light at the Surface of a Dielectric-Coated Metal Grating. *IEEE Photonics Journal*, *6*(4), 1–6. https://doi.org/10.1109/JPHOT.2014.2337893

Chen, W., Shan, S., Peng, J., Liu, D., Xia, J., Shao, B., & Lai, W. (2020). Sensitive and

hook effect–free lateral flow assay integrated with cascade signal transduction system. *Sensors and Actuators, B: Chemical*, *321*(June), 128465. https://doi.org/10.1016/j.snb.2020.128465

Chen, Y., Li, K., Zhang, S., Xu, P., & Song, B. (2022). Turn-on fluorescence probe for BSA detection and selective cell imaging. *Dyes and Pigments*, *202*(February). https://doi.org/10.1016/j.dyepig.2022.110267

Cheng, L., Zhu, G., Liu, G., & Zhu, L. (2020). FDTD simulation of the optical properties for gold nanoparticles. *Materials Research Express*, *7*(12). https://doi.org/10.1088/2053-1591/abd139

Chiavaioli, F., & Janner, D. (2021). Fiber Optic Sensing with Lossy Mode Resonances: Applications and Perspectives. *Journal of Lightwave Technology*, *39*(12), 3855–3870. https://doi.org/10.1109/JLT.2021.3052137

Chiavaioli, F., Zubiate, P., Del Villar, I., ZamarrenÌo, C. R., Giannetti, A., Tombelli, S., Trono, C., Arregui, F. J., Matias, I. R., & Baldini, F. (2018). Femtomolar Detection by Nanocoated Fiber Label-Free Biosensors. *ACS Sensors*, *3*(5), 936–943. https://doi.org/10.1021/acssensors.7b00918

Chiu, N.-F., Lin, C.-W., Lee, J.-H., Kuan, C.-H., Wu, K.-C., & Lee, C.-K. (2007). Enhanced luminescence of organic/metal nanostructure for grating coupler active long-range surface plasmonic device. *Applied Physics Letters*, *91*(8). https://doi.org/10.1063/1.2773961

Chiu, N.-F., Nien, S.-Y., Yu, C., Lee, J., & Lin, C. (2006). Advanced Metal Nanostructure Design for Surface Plasmon Photonic Bandgap Biosensor Device. *2006 International Conference of the IEEE Engineering in Medicine and Biology Society*, *Supplement*, 6521–6524. https://doi.org/10.1109/IEMBS.2006.260869

Chiu, N.-F., Yu, C., Nien, S.-Y., Lee, J.-H., Kuan, C.-H., Wu, K.-C., Lee, C.-K., & Lin, C.-W. (2007). Enhancement and tunability of active plasmonic by multilayer grating coupled emission. *Optics Express*, *15*(18), 11608. https://doi.org/10.1364/oe.15.011608

Chiu, N. F., Chen, C. C., Yang, C. Du, Kao, Y. S., & Wu, W. R. (2018). Enhanced Plasmonic Biosensors of Hybrid Gold Nanoparticle-Graphene Oxide-Based Label-Free Immunoassay. *Nanoscale Research Letters*, *13*. https://doi.org/10.1186/s11671-018-2565-7

Chiu, Tai, M.-J., Nurrohman, D. T., Lin, T.-L., Wang, Y.-H., & Chen, C.-Y. (2021). Immunoassay-Amplified Responses Using a Functionalized MoS2-Based SPR Biosensor to Detect PAPP-A2 in Maternal Serum Samples to Screen for Fetal Down's

Syndrome. *International Journal of Nanomedicine*, *Volume 16*, 2715–2733. https://doi.org/10.2147/IJN.S296406

Coles, D. M., Meijer, A. J. H. M., Tsoi, W. C., Charlton, M. D. B., Kim, J.-S., & Lidzey, D. G. (2010). A Characterization of the Raman Modes in a J-Aggregate-Forming Dye: A Comparison between Theory and Experiment. *The Journal of Physical Chemistry A*, *114*(44), 11920–11927. https://doi.org/10.1021/jp107646p

Colthup, N. B., Daly, L. H., & Wiberley, S. E. (1990). Introduction to Infrared and Raman Spectroscopy. In *Introduction to Infrared and Raman Spectroscopy*. https://doi.org/10.1016/b978-0-08-091740-5.50003-x

Cui, M., Xin, Y., Song, R., Sun, Q., Wang, X., & Lu, D. (2020). Fluorescence sensor for bovine serum albumin detection based on the aggregation and release of CdS QDs within CMC. *Cellulose*, *27*(3), 1621–1633. https://doi.org/10.1007/s10570-019-02865-4

Damborský, P., Švitel, J., & Katrlík, J. (2016). Optical biosensors. *Essays in Biochemistry*, *60*(1), 91–100. https://doi.org/10.1042/EBC20150010

Das, C. M., Kang, L., Chen, M. W., Coquet, P., & Yong, K.-T. (2020). Heterolayered Films of Monolayer WS 2 Nanosheets on Monolayer Graphene Embedded in Poly(methyl methacrylate) for Plasmonic Biosensing. *ACS Applied Nano Materials*, *3*(10), 10446–10453. https://doi.org/10.1021/acsanm.0c02328

Dhar, S., Barman, A. R., Ni, G. X., Wang, X., Xu, X. F., Zheng, Y., Tripathy, S., Ariando, Rusydi, A., Loh, K. P., Rubhausen, M., Neto, A. H. C., Őzyilmaz, B., & Venkatesan, T. (2011). A new route to graphene layers by selective laser ablation. *AIP Advances*, *1*(2). https://doi.org/10.1063/1.3584204

Dheyab, M. A., Aziz, A. A., Moradi Khaniabadi, P., Jameel, M. S., Oladzadabbasabadi, N., Mohammed, S. A., Abdullah, R. S., & Mehrdel, B. (2022). Monodisperse Gold Nanoparticles: A Review on Synthesis and Their Application in Modern Medicine. *International Journal of Molecular Sciences*, *23*(13), 7400. https://doi.org/10.3390/ijms23137400

Dominguez, I., Corres, J. M., Del Villar, I., Mozo, J. D., Simerova, R., Sezemsky, P., Stranak, V., Śmietana, M., & Matias, I. R. (2023). Electrochemical lossy mode resonance for detection of manganese ions. *Sensors and Actuators B: Chemical*, *394*(February). https://doi.org/10.1016/j.snb.2023.134446

Doveiko, D., Kubiak-Ossowska, K., & Chen, Y. (2023). Impact of the Crystal Structure of Silica Nanoparticles on Rhodamine 6G Adsorption: A Molecular Dynamics Study.

ACS Omega. https://doi.org/10.1021/acsomega.3c06657

Driskell, J. D., Lipert, R. J., & Porter, M. D. (2006). Labeled Gold Nanoparticles Immobilized at Smooth Metallic Substrates: Systematic Investigation of Surface Plasmon Resonance and Surface-Enhanced Raman Scattering. *The Journal of Physical Chemistry B*, *110*(35), 17444–17451. https://doi.org/10.1021/jp0636930

Farooq, S., Neves, W. W., Pandoli, O., Del Rosso, T., de Lima, L. M., Dutra, R. F., & de Araujo, R. E. (2018). Engineering a plasmonic sensing platform for Candida albicans antigen identification. *Journal of Nanophotonics*, *12*(03), 1. https://doi.org/10.1117/1.jnp.12.033003

Farooq, S., Wali, F., Zezell, D. M., de Araujo, R. E., & Rativa, D. (2022). Optimizing and Quantifying Gold Nanospheres Based on LSPR Label-Free Biosensor for Dengue Diagnosis. *Polymers*, *14*(8), 1–12. https://doi.org/10.3390/polym14081592

Foucher, F. (2022). Influence of laser shape on thermal increase during micro-Raman spectroscopy analyses. *Journal of Raman Spectroscopy*, *53*(3), 664–676. https://doi.org/10.1002/jrs.6230

Gao, Y., Zhu, Z., Xi, X., Cao, T., Wen, W., Zhang, X., & Wang, S. (2019). An aptamer-based hook-effect-recognizable three-line lateral flow biosensor for rapid detection of thrombin. *Biosensors and Bioelectronics*, *133*(March), 177–182. https://doi.org/10.1016/j.bios.2019.03.036

Geraldes, C. F. G. C. (2020). Introduction to infrared and raman-based biomedical molecular imaging and comparison with other modalities. *Molecules*, *25*(23). https://doi.org/10.3390/molecules25235547

Gupta, B. D., Usha, S. P., & Shrivastav, A. M. (2016). A Novel Approach of LMR/MIP for Optical Fiber based Salivary Cortisol Sensor. *Conference on Lasers and Electro-Optics*, *1*, JTu5A.145. https://doi.org/10.1364/CLEO_AT.2016.JTu5A.145

Gurarslan, A., Yu, Y., Su, L., Yu, Y., Suarez, F., Yao, S., Zhu, Y., Ozturk, M., Zhang, Y., & Cao, L. (2014). Surface-Energy-Assisted Perfect Transfer of Centimeter-Scale Monolayer and Few-Layer MoS 2 Films onto Arbitrary Substrates. *ACS Nano*, *8*(11), 11522–11528. https://doi.org/10.1021/nn5057673

Gurung, S., Perocheau, D., Touramanidou, L., & Baruteau, J. (2021). The exosome journey: from biogenesis to uptake and intracellular signalling. *Cell Communication and Signaling*, *19*(1), 1–19. https://doi.org/10.1186/s12964-021-00730-1

Guthmuller, J., & Champagne, B. (2008). Resonance Raman spectra and Raman excitation profiles of rhodamine 6G from time-dependent density functional theory.

ChemPhysChem, *9*(12), 1667–1669. https://doi.org/10.1002/cphc.200800253

Hammond, J. L., Bhalla, N., Rafiee, S. D., & Estrela, P. (2014). Localized surface plasmon resonance as a biosensing platform for developing countries. *Biosensors*, *4*(2), 172–188. https://doi.org/10.3390/bios4020172

Hampitak, P., Melendrez, D., Iliut, M., Fresquet, M., Parsons, N., Spencer, B., Jowitt, T. A., & Vijayaraghavan, A. (2020). Protein interactions and conformations on graphene-based materials mapped using quartz-crystal microbalance with dissipation monitoring (QCM-D). *Carbon*, *165*, 317–327. https://doi.org/10.1016/j.carbon.2020.04.093

Haran, G., Champion, P. M., & Ziegler, L. D. (2010). Single-Molecule Raman Spectroscopy: A Probe of Charge Transfer and Plasmonic Fields. *AIP Conference Proceedings*, *1267*(8), 59–60. https://doi.org/10.1063/1.3482699

Hardy, M., & Goldberg Oppenheimer, P. (2024). 'When is a hotspot a good nanospot' - review of analytical and hotspot-dominated surface enhanced Raman spectroscopy nanoplatforms. *Nanoscale*, *14*(3), 3293–3323. https://doi.org/10.1039/d3nr05332f

He, X. N., Gao, Y., Mahjouri-Samani, M., Black, P. N., Allen, J., Mitchell, M., Xiong, W., Zhou, Y. S., Jiang, L., & Lu, Y. F. (2012). Surface-enhanced Raman spectroscopy using gold-coated horizontally aligned carbon nanotubes. *Nanotechnology*, *23*(20). https://doi.org/10.1088/0957-4484/23/20/205702

Heo, S. W. (2020). Ultra-Flexible Organic Photovoltaics with Nanograting Patterns Based on CYTOP/Ag Nanowires Substrate. *Nanomaterials*, *10*(11), 2185. https://doi.org/10.3390/nano10112185

Hsu, C., Frisenda, R., Schmidt, R., Arora, A., Vasconcellos, S. M., Bratschitsch, R., Zant, H. S. J., Castellanos-Gomez, A., de Vasconcellos, S. M., Bratschitsch, R., van der Zant, H. S. J., & Castellanos-Gomez, A. (2019). Thickness-Dependent Refractive Index of 1L, 2L, and 3L MoS 2 , MoSe 2 , WS 2 , and WSe 2. *Advanced Optical Materials*, *7*(13), 1900239. https://doi.org/10.1002/adom.201900239

Iarossi, M., Schiattarella, C., Rea, I., De Stefano, L., Fittipaldi, R., Vecchione, A., Velotta, R., & Ventura, B. Della. (2018). Colorimetric Immunosensor by Aggregation of Photochemically Functionalized Gold Nanoparticles. *ACS Omega*, *3*(4), 3805–3812. https://doi.org/10.1021/acsomega.8b00265

Jain, P. K., Lee, K. S., El-Sayed, I. H., & El-Sayed, M. A. (2006). Calculated Absorption and Scattering Properties of Gold Nanoparticles of Different Size, Shape, and Composition: Applications in Biological Imaging and Biomedicine. *The Journal of*

Physical Chemistry B, *110*(14), 7238–7248. https://doi.org/10.1021/jp057170o

Jeon, J., Uthaman, S., Lee, J., Hwang, H., Kim, G., Yoo, P. J., Hammock, B. D., Kim, C. S., Park, Y. S., & Park, I. K. (2018). In-direct localized surface plasmon resonance (LSPR)-based nanosensors for highly sensitive and rapid detection of cortisol. *Sensors and Actuators, B: Chemical*, *266*, 710–716. https://doi.org/10.1016/j.snb.2018.03.167

Jia, S., Bian, C., Sun, J., Tong, J., & Xia, S. (2018). A wavelength-modulated localized surface plasmon resonance (LSPR) optical fiber sensor for sensitive detection of mercury(II) ion by gold nanoparticles-DNA conjugates. *Biosensors and Bioelectronics*, *114*(January), 15–21. https://doi.org/10.1016/j.bios.2018.05.004

Jia, Y., Gao, Y., Xu, W., Wang, Y., Yan, Z., Chen, K., & Chen, S. (2024). Improving signal-to-noise ratio of Raman measurements based on ensemble learning approach. *Analytical and Bioanalytical Chemistry*, *417*(3), 641–652. https://doi.org/10.1007/s00216-024-05676-0

Jia, Y., Li, Z., Wang, H., Saeed, M., & Cai, H. (2019). Sensitivity Enhancement of a Surface Plasmon Resonance Sensor with Platinum Diselenide. *Sensors*, *20*(1), 131. https://doi.org/10.3390/s20010131

Jo, S., Lee, W., Park, J., Park, H., Kim, M., Kim, W., Hong, J., & Park, J. (2021). Wide-range direct detection of 25-hydroxyvitamin D3 using polyethylene-glycol-free gold nanorod based on LSPR aptasensor. *Biosensors and Bioelectronics*, *181*(March), 113118. https://doi.org/10.1016/j.bios.2021.113118

Johnson, P. B., & Christy, R. W. (1974). Optical constants of transition metals: Ti, V, Cr, Mn, Fe, Co, Ni, and Pd. *Physical Review B*, *2*(1), 31–34. https://doi.org/10.1016/0167-577X(83)90026-5

Jung, N., Namjoshi, S., Mohammed, Y., Grice, J. E., Benson, H. A. E., Raney, S. G., Roberts, M. S., & Windbergs, M. (2022). Application of Confocal Raman Microscopy for the Characterization of Topical Semisolid Formulations and their Penetration into Human Skin Ex Vivo. *Pharmaceutical Research*, *39*(5), 935–948. https://doi.org/10.1007/s11095-022-03245-7

Kang, J., Zhang, Y., Li, X., Miao, L., & Wu, A. (2016). A Rapid Colorimetric Sensor of Clenbuterol Based on Cysteamine-Modified Gold Nanoparticles. *ACS Applied Materials and Interfaces*, *8*(1), 1–5. https://doi.org/10.1021/acsami.5b09079

Kastner, S., Pritzke, P., Csáki, A., & Fritzsche, W. (2022). The effect of layer thickness and immobilization chemistry on the detection of CRP in LSPR assays. *Scientific Reports*,

12(1), 1–10. https://doi.org/10.1038/s41598-022-04824-9

Kaur, D., Sharma, V. K., & Kapoor, A. (2014). High sensitivity lossy mode resonance sensors. *Sensors and Actuators B: Chemical*, *198*, 366–376. https://doi.org/10.1016/j.snb.2014.03.058

Kaushik, S., Tiwari, U. K., Deep, A., & Sinha, R. K. (2019). Two-dimensional transition metal dichalcogenides assisted biofunctionalized optical fiber SPR biosensor for efficient and rapid detection of bovine serum albumin. *Scientific Reports*, *9*(1), 6987. https://doi.org/10.1038/s41598-019-43531-w

Khansili, N., Rattu, G., & Krishna, P. M. (2018). Label-free optical biosensors for food and biological sensor applications. *Sensors and Actuators B: Chemical*, *265*, 35–49. https://doi.org/10.1016/j.snb.2018.03.004

Khosroshahi, M. E., Patel, Y., Gaoiran, C., & Umashanker, V. (2025). SERS characterization of Rhodamine 6G dye molecule response using thin gold film covalently immobilized with gold nanourchins. *Characterization and Application of Nanomaterials*, *8*(2), 10951. https://doi.org/10.24294/can10951

Kim, D. M., Park, J. S., Jung, S.-W., Yeom, J., & Yoo, S. M. (2021). Biosensing Applications Using Nanostructure-Based Localized Surface Plasmon Resonance Sensors. *Sensors*, *21*(9), 3191. https://doi.org/10.3390/s21093191

Kim, J., Oh, S. Y., Shukla, S., Hong, S. B., Heo, N. S., Bajpai, V. K., Chun, H. S., Jo, C.-H., Choi, B. G., Huh, Y. S., & Han, Y.-K. (2018). Heteroassembled gold nanoparticles with sandwich-immunoassay LSPR chip format for rapid and sensitive detection of hepatitis B virus surface antigen (HBsAg). *Biosensors and Bioelectronics*, *107*(October 2017), 118–122. https://doi.org/10.1016/j.bios.2018.02.019

Kim, Y., Gonzales, J., & Zheng, Y. (2021). Sensitivity-Enhancing Strategies in Optical Biosensing. *Small*, *17*(4), 1–12. https://doi.org/10.1002/smll.202004988

König, T. A. F., Ledin, P. A., Kerszulis, J., Mahmoud, M. A., El-Sayed, M. A., Reynolds, J. R., & Tsukruk, V. V. (2014). Electrically tunable plasmonic behavior of nanocube-polymer nanomaterials induced by a redox-active electrochromic polymer. *ACS Nano*, *8*(6), 6182–6192. https://doi.org/10.1021/nn501601e

Kravets, V. G., Jalil, R., Kim, Y.-J., Ansell, D., Aznakayeva, D. E., Thackray, B., Britnell, L., Belle, B. D., Withers, F., Radko, I. P., Han, Z., Bozhevolnyi, S. I., Novoselov, K. S., Geim, A. K., & Grigorenko, A. N. (2014). Graphene-protected copper and silver plasmonics. *Scientific Reports*, *4*(1), 5517. https://doi.org/10.1038/srep05517

Krivosudský, O., Dráber, P., & Cifra, M. (2017). Resolving controversy of unusually high

refractive index of a tubulin. *Epl*, *117*(3). https://doi.org/10.1209/0295-5075/117/38003

Kumar, A., Islam, M. R., Zughaier, S. M., Chen, X., & Zhao, Y. (2024). Precision classification and quantitative analysis of bacteria biomarkers via surface-enhanced Raman spectroscopy and machine learning. *Spectrochimica Acta - Part A: Molecular and Biomolecular Spectroscopy*, *320*(April), 124627. https://doi.org/10.1016/j.saa.2024.124627

Kumar, S., Guo, Z., Singh, R., Wang, Q., Zhang, B., Cheng, S., Liu, F.-Z., Marques, C., Kaushik, B. K., & Jha, R. (2021). MoS 2 Functionalized Multicore Fiber Probes for Selective Detection of Shigella Bacteria Based on Localized Plasmon. *Journal of Lightwave Technology*, *39*(12), 4069–4081. https://doi.org/10.1109/JLT.2020.3036610

Kumar, S., Singh, R., Kaushik, B. K., Chen, N. K., Yang, Q. S., & Zhang, X. (2019). Lspr-based cholesterol biosensor using hollow core fiber structure. *IEEE Sensors Journal*, *19*(17), 7399–7406. https://doi.org/10.1109/JSEN.2019.2916818

Kwack, Y.-J., Can, T. T. T., & Choi, W.-S. (2021). Bottom-up water-based solution synthesis for a large MoS2 atomic layer for thin-film transistor applications. *Npj 2D Materials and Applications*, *5*(1), 84. https://doi.org/10.1038/s41699-021-00264-7

Lambert, A. S., Valiulis, S. N., Malinick, A. S., Tanabe, I., & Cheng, Q. (2020). Plasmonic Biosensing with Aluminum Thin Films under the Kretschmann Configuration. *Analytical Chemistry*, *92*(13), 8654–8659. https://doi.org/10.1021/acs.analchem.0c01631

Lee, T., Kim, J., Nam, I., Lee, Y., Kim, H. E., Sohn, H., Kim, S. E., Yoon, J., Seo, S. W., Lee, M. H., & Park, C. (2019). Fabrication of troponin i biosensor composed of multi-functional dna structure/au nanocrystal using electrochemical and localized surface plasmon resonance dual-detection method. *Nanomaterials*, *9*(7). https://doi.org/10.3390/nano9071000

Letko, E., Bundulis, A., Vanags, E., & Mozolevskis, G. (2024). Lossy mode resonance in photonic integrated circuits. *Optics and Lasers in Engineering*, *181*(May), 108387. https://doi.org/10.1016/j.optlaseng.2024.108387

Li, B., Li, Z., Zhang, F., Lu, B., Guo, P., Guo, L., & Hou, W. (2025). A Dual-Parameter Optical Fiber Sensor Based on SPR and LMR for Measuring Liquid Refractive Index and Temperature. *IEEE Sensors Journal*, *25*(8), 12907–12914. https://doi.org/10.1109/JSEN.2025.3549793

Li, J., Ye, J., Chen, C., Hermans, L., Verellen, N., Ryken, J., Jans, H., Van Roy, W.,

Moshchalkov, V. V., Lagae, L., & Van Dorpe, P. (2015). Biosensing using diffractively coupled plasmonic crystals: The figure of merit revisited. *Advanced Optical Materials*, *3*(2), 176–181. https://doi.org/10.1002/adom.201400394

Li, L., Zhao, J., Jin, M., Wu, S., Liu, F., Huang, Y., Feng, N., & Liu, Y. (2025). Dual-mode SPR/SERS optical fiber sensor for ultra-trace mercury ions detection. *Optics Express*, *33*(2), 2247. https://doi.org/10.1364/OE.547601

Li, M., Singh, R., Marques, C., Zhang, B., & Kumar, S. (2021). 2D material assisted SMF-MCF-MMF-SMF based LSPR sensor for creatinine detection. *Optics Express*, *29*(23), 38150. https://doi.org/10.1364/oe.445555

Li, W. H., Li, X. Y., & Yu, N. T. (1999). Surface-enhanced resonance hyper-Raman scattering and surface-enhanced resonance Raman scattering of dyes adsorbed on silver electrode and silver colloid: A comparison study. *Chemical Physics Letters*, *312*(1), 28–36. https://doi.org/10.1016/S0009-2614(99)00892-1

Li, Y., Jiang, L., Yu, Z., Jiang, C., Zhang, F., & Jin, S. (2024). SPRi/SERS dual-mode biosensor based on ployA-DNA/ miRNA/AuNPs-enhanced probe sandwich structure for the detection of multiple miRNA biomarkers. *Spectrochimica Acta Part A: Molecular and Biomolecular Spectroscopy*, *308*(November 2023), 123664. https://doi.org/10.1016/j.saa.2023.123664

Liang, X., Wei, H., Cui, Z., Deng, J., Zhang, Z., You, X., & Zhang, X. E. (2011). Colorimetric detection of melamine in complex matrices based on cysteamine-modified gold nanoparticles. *Analyst*, *136*(1), 179–183. https://doi.org/10.1039/c0an00432d

Lin, Y., Zou, Y., & Lindquist, R. G. (2011). A reflection-based localized surface plasmon resonance fiber-optic probe for biochemical sensing. *Biomedical Optics Express*, *2*(3), 478. https://doi.org/10.1364/boe.2.000478

Liu, B., Huang, R., Yu, Y., Su, R., Qi, W., & He, Z. (2018). Gold nanoparticle-aptamer-based LSPR sensing of Ochratoxin A at a widened detection range by double calibration curve method. *Frontiers in Chemistry*, *6*(APR), 1–9. https://doi.org/10.3389/fchem.2018.00094

Liu, H. L., Yang, T., Chen, J. H., Chen, H. W., Guo, H., Saito, R., Li, M. Y., & Li, L. J. (2020). Temperature-dependent optical constants of monolayer MoS 2 , MoSe 2 , WS 2 , and WSe 2 : spectroscopic ellipsometry and first-principles calculations. *Scientific Reports*, *10*(1), 1–11. https://doi.org/10.1038/s41598-020-71808-y

Liu, K., Zhang, J., Jiang, J., Xu, T., Wang, S., Chang, P., Zhang, Z., Ma, J., & Liu, T.

(2020). MoSe2-Au Based Sensitivity Enhanced Optical Fiber Surface Plasmon Resonance Biosensor for Detection of Goat-Anti-Rabbit IgG. *IEEE Access*, *8*, 660–668. https://doi.org/10.1109/ACCESS.2019.2961751

Liu, T., Ding, H., Zhan, C., Huang, J., & Wang, S. (2021). Simply and cost-effectively fabricated AuNP-based fusion spliced transmissive optical fiber LSPR probes. *Optics Express*, *29*(5), 7398. https://doi.org/10.1364/oe.417198

Liu, W., Yan, Z., Zhang, W., Wen, K., Sun, B., Hu, X., & Qin, Y. (2023). Facile Preparation of Au–Ag Composite Nanostructure for High-Sensitive and Uniform Surface-Enhanced Raman Spectroscopy. *Photonics*, *10*(4). https://doi.org/10.3390/photonics10040354

Liu, Y. B., Zhai, T. T., Liang, Y. Y., Wang, Y. B., & Xia, X. H. (2019). Gold core-satellite nanostructure linked by oligonucleotides for detection of glutathione with LSPR scattering spectrum. *Talanta*, *193*(September 2018), 123–127. https://doi.org/10.1016/j.talanta.2018.09.096

Liu, Y. C., Yu, C. C., & Sheu, S. F. (2006). Improved surface-enhanced Raman scattering on optimum electrochemically roughened silver substrates. *Analytica Chimica Acta*, *577*(2), 271–275. https://doi.org/10.1016/j.aca.2006.06.062

Long, S., Cao, J., Wang, Y., Gao, S., Xu, N., Gao, J., & Wan, W. (2020). Grating coupled SPR sensors using off the shelf compact discs and sensitivity dependence on grating period. *Sensors and Actuators Reports*, *2*(1), 100016. https://doi.org/10.1016/j.snr.2020.100016

López-Muñoz, G. A., Estevez, M. C., Peláez-Gutierrez, E. C., Homs-Corbera, A., García-Hernandez, M. C., Imbaud, J. I., & Lechuga, L. M. (2017). A label-free nanostructured plasmonic biosensor based on Blu-ray discs with integrated microfluidics for sensitive biodetection. *Biosensors and Bioelectronics*, *96*(May), 260–267. https://doi.org/10.1016/j.bios.2017.05.020

Lopez, S., Zamarreño, C. R., Hernaez, M., Del Villar, I., Arregui, F. J., & Matias, I. R. (2011). Optical fiber refractometers based on sputtered indium tin oxide coatings. *Proceedings of the International Conference on Sensing Technology, ICST*, *37*(1), 585–588. https://doi.org/10.1109/ICSensT.2011.6137047

Lu, C. H., Wang, S. L., Ye, S. L., Chen, G. N., & Yang, H. H. (2012). Ultrasensitive detection of Cu2+ with the naked eye and application in immunoassays. *NPG Asia Materials*, *4*(3). https://doi.org/10.1038/am.2012.18

Lu, C., Qi, Z., Hu, X., Ni, Z., & Cui, Y. (2019). Selectively enhanced Raman scattering with

triple-resonance nanohole arrays. *Optics Communications*, *452*(July), 494–498. https://doi.org/10.1016/j.optcom.2019.07.074

Lu, Y., Zhang, W., & Zhang, H. (2022). Study on Antireflection Film Based on Nano Pore. *2022 7th International Conference on Integrated Circuits and Microsystems (ICICM)*, 186–189. https://doi.org/10.1109/ICICM56102.2022.10011311

Ma, Y., Jiang, L., Mei, Y., Song, R., Tian, D., & Huang, H. (2013). Colorimetric sensing strategy for mercury(ii) and melamine utilizing cysteamine-modified gold nanoparticles. *Analyst*, *138*(18), 5338–5343. https://doi.org/10.1039/c3an00690e

Ma, Z., Lv, X., Fang, W., Chen, H., Pei, W., & Geng, Z. (2022). Au Nanoparticle-Based Integrated Microfluidic Plasmonic Chips for the Detection of Carcinoembryonic Antigen in Human Serum. *ACS Applied Nano Materials*, *5*(11), 17281–17292. https://doi.org/10.1021/acsanm.2c04495

Majoube, M., & Henry, M. (1991). Fourier transform Raman and infrared and surface-enhanced Raman spectra for rhodamine 6G. *Spectrochimica Acta Part A: Molecular Spectroscopy*, *47*(9–10), 1459–1466. https://doi.org/10.1016/0584-8539(91)80237-D

Marshall, A. R. L., Stokes, J., Viscomi, F. N., Proctor, J. E., Gierschner, J., Bouillard, J.-S. G., & Adawi, A. M. (2017). Determining molecular orientation via single molecule SERS in a plasmonic nano-gap. *Nanoscale*, *9*(44), 17415–17421. https://doi.org/10.1039/C7NR05107G

Maurya, J. B., François, A., & Prajapati, Y. (2018). Two-Dimensional Layered Nanomaterial-Based One-Dimensional Photonic Crystal Refractive Index Sensor. *Sensors*, *18*(3), 857. https://doi.org/10.3390/s18030857

Maurya, J. B., Nikki, Saini, J. P., Sharma, A. K., & Prajapati, Y. K. (2023). A localized SPR D-shaped fiber optic sensor utilizing silver grating coated with graphene: Field analysis. *Optical Fiber Technology*, *75*(October 2022), 103204. https://doi.org/10.1016/j.yofte.2022.103204

Meza-Sánchez, D. E., & Maravillas-Montero, J. L. (2019). Clinical and biomedical applications of surface plasmon resonance systems. *Revista de Investigacion Clinica*, *71*(2), 85–90. https://doi.org/10.24875/RIC.18002754

Minopoli, A., Sakač, N., Lenyk, B., Campanile, R., Mayer, D., Offenhäusser, A., Velotta, R., & Della Ventura, B. (2020). LSPR-based colorimetric immunosensor for rapid and sensitive 17β-estradiol detection in tap water. *Sensors and Actuators, B: Chemical*, *308*(January). https://doi.org/10.1016/j.snb.2020.127699

Mishra, A. K., & Mishra, S. K. (2016). Gas sensing in Kretschmann configuration utilizing

bi-metallic layer of Rhodium-Silver in visible region. *Sensors and Actuators, B: Chemical*, *237*, 969–973. https://doi.org/10.1016/j.snb.2016.07.041

Mostufa, S., Rezaei, B., Ciannella, S., Yari, P., Gómez-Pastora, J., He, R., & Wu, K. (2024). Advancements and Perspectives in Optical Biosensors. *ACS Omega*, *9*(23), 24181–24202. https://doi.org/10.1021/acsomega.4c01872

Nisar, M. S., Kang, S., & Zhao, X. (2020). Photothermal Effect in Plasmonic Nanotip for LSPR Sensing. *Sensors*, *20*(3), 671. https://doi.org/10.3390/s20030671

Novák, P., Očenášek, J., Prušáková, L., Vavruňková, V., Savková, J., & Rezek, J. (2016). Influence of heat generated by a Raman excitation laser on the structural analysis of thin amorphous silicon film. *Applied Surface Science*, *364*, 302–307. https://doi.org/10.1016/j.apsusc.2015.12.091

Nurrohman, D. T., Cagayan, G. R. A., & Chiu, N.-F. (2025). Characterization of SPR and cavity modes in one-dimensional (1D) gold nanograting chips: figure of merit analysis and implications for Raman signal enhancement. *Optics Express*, *33*(1), 1542. https://doi.org/10.1364/oe.547581

Nurrohman, D. T., & Chiu, N.-F. (2024a). Performance Comparison of Lossy Mode Resonance Refractive Index Sensors on Structures Based on Graphene and MoS 2. *ECS Journal of Solid State Science and Technology*, *13*(3), 037010. https://doi.org/10.1149/2162-8777/ad325d

Nurrohman, D. T., & Chiu, N. (2024b). Molybdenum Disulfide-based Lossy Mode Resonance Sensors: Uncovering Wider Dynamic Range and High Sensitivity Through Computational Approaches. *Advanced Theory and Simulations*, *7*(4). https://doi.org/10.1002/adts.202300909

Nurrohman, D. T., & Chiu, N. F. (2023). Interaction Studies of Localized Surface Plasmon Resonance Immunosensor Based on Gold Nanoparticles. *IEEE Sensors Journal*, *23*(17), 19262–19271. https://doi.org/10.1109/JSEN.2023.3298677

Nurrohman, D. T., Chiu, N. F., Hsiao, Y. S., Lai, Y. J., & Nanda, H. S. (2024). Advances in Nanoplasmonic Biosensors: Optimizing Performance for Exosome Detection Applications. *Biosensors*, *14*(6). https://doi.org/10.3390/bios14060307

Oh, S. Y., Heo, N. S., Bajpai, V. K., Jang, S. C., Ok, G., Cho, Y., & Huh, Y. S. (2019). Development of a Cuvette-Based LSPR Sensor Chip Using a Plasmonically Active Transparent Strip. *Frontiers in Bioengineering and Biotechnology*, *7*(November), 1–11. https://doi.org/10.3389/fbioe.2019.00299

Oh, S. Y., Heo, N. S., Shukla, S., Cho, H. J., Vilian, A. T. E., Kim, J., Lee, S. Y., Han, Y. K.,

Yoo, S. M., & Huh, Y. S. (2017). Development of gold nanoparticle-aptamer-based LSPR sensing chips for the rapid detection of Salmonella typhimurium in pork meat. *Scientific Reports*, *7*(1), 1–10. https://doi.org/10.1038/s41598-017-10188-2

Oliveira, J. P., Prado, A. R., Keijok, W. J., Ribeiro, M. R. N., Pontes, M. J., Nogueira, B. V., & Guimarães, M. C. C. (2020). A helpful method for controlled synthesis of monodisperse gold nanoparticles through response surface modeling. *Arabian Journal of Chemistry*, *13*(1), 216–226. https://doi.org/10.1016/j.arabjc.2017.04.003

Orbaek, A. W., McHale, M. M., & Barron, A. R. (2015). Synthesis and characterization of silver nanoparticles for an undergraduate laboratory. *Journal of Chemical Education*, *92*(2), 339–344. https://doi.org/10.1021/ed500036b

Orlando, A., Franceschini, F., Muscas, C., Pidkova, S., Bartoli, M., Rovere, M., & Tagliaferro, A. (2021). A comprehensive review on Raman spectroscopy applications. *Chemosensors*, *9*(9), 1–28. https://doi.org/10.3390/chemosensors9090262

Ozcariz, A. (2018). Development of Copper Oxide Thin Film for Lossy Mode Resonance-Based Optical Fiber Sensor. *EUROSENSORS 2018*, 893. https://doi.org/10.3390/proceedings2130893

Ozcariz, A., Dominik, M., Smietana, M., Zamarreño, C. R., Del Villar, I., & Arregui, F. J. (2019). Lossy mode resonance optical sensors based on indium-gallium-zinc oxide thin film. *Sensors and Actuators, A: Physical*, *290*, 20–27. https://doi.org/10.1016/j.sna.2019.03.010

Ozcariz, A., Piña-Azamar, D. A., Zamarreño, C. R., Dominguez, R., & Arregui, F. J. (2019). Aluminum doped zinc oxide (AZO) coated optical fiber LMR refractometers—An experimental demonstration. *Sensors and Actuators, B: Chemical*, *281*(April 2018), 698–704. https://doi.org/10.1016/j.snb.2018.10.158

Pal, A., & Varma, M. M. (2024). Study of Surface-Enhanced Raman Scattering of Rhodamine 6G from repeated dewetted gold thin film. *APSCON 2024 - 2024 IEEE Applied Sensing Conference, Proceedings*, 1–4. https://doi.org/10.1109/APSCON60364.2024.10465787

Pál, P., Bonyár, A., Veres, M., Juhász, L., Szalóki, M., & Csarnovics, I. (2021). An Investigation of Surface-Enhanced Raman Scattering of Different Analytes Adsorbed on Gold Nanoislands. *Applied Sciences*, *11*(21), 9838. https://doi.org/10.3390/app11219838

Pandey, A. K., & Sharma, A. K. (2021). Advancements in Grating Nanostructure Based Plasmonic Sensors in Last Two Decades: A Review. *IEEE Sensors Journal*, *21*(11),

12633–12644. https://doi.org/10.1109/JSEN.2020.3045292

Park, J.-W., & Shumaker-Parry, J. S. (2014). Structural Study of Citrate Layers on Gold Nanoparticles: Role of Intermolecular Interactions in Stabilizing Nanoparticles. *Journal of the American Chemical Society*, *136*(5), 1907–1921. https://doi.org/10.1021/ja4097384

Park, J. H., Byun, J. Y., Jang, H., Hong, D., & Kim, M. G. (2017). A highly sensitive and widely adaptable plasmonic aptasensor using berberine for small-molecule detection. *Biosensors and Bioelectronics*, *97*(June), 292–298. https://doi.org/10.1016/j.bios.2017.06.019

Parvin, T., Ahmed, K., Alatwi, A. M., & Rashed, A. N. Z. (2021). Differential optical absorption spectroscopy-based refractive index sensor for cancer cell detection. *Optical Review*, *28*(1), 134–143. https://doi.org/10.1007/s10043-021-00644-w

Prasanth, A., Meher, S. R., & Alex, Z. C. (2021). Experimental analysis of SnO2 coated LMR based fiber optic sensor for ethanol detection. *Optical Fiber Technology*, *65*(November 2020), 102618. https://doi.org/10.1016/j.yofte.2021.102618

Prieto-Cortés, P., Álvarez-Tamayo, R. I., García-Méndez, M., & Durán-Sánchez, M. (2019). Lossy Mode Resonance Generation on Sputtered Aluminum-Doped Zinc Oxide Thin Films Deposited on Multimode Optical Fiber Structures for Sensing Applications in the 1.55 μm Wavelength Range. *Sensors*, *19*(19), 4189. https://doi.org/10.3390/s19194189

Purcar, V., Donescu, D., Petcu, C., & Vasilescu, M. (2008). Nanostructured hybrid systems with rhodamine 6G. *Journal of Dispersion Science and Technology*, *29*(9), 1233–1239. https://doi.org/10.1080/01932690701856915

Qadami, F., Molaeirad, A., Alijanianzadeh, M., Azizi, A., & Kamali, N. (2018). Localized Surface Plasmon Resonance (LSPR)-Based Nanobiosensor for Methamphetamin Measurement. *Plasmonics*, *13*(6), 2091–2098. https://doi.org/10.1007/s11468-018-0725-3

Qian, S., Chen, X., Jiang, S., Pan, Q., Gao, Y., Wang, L., Peng, W., Liang, S., Zhu, J., & Liu, S. (2020). Direct detection of charge and discharge process in supercapacitor by fiber-optic LSPR sensors. *Nanophotonics*, *9*(5), 1071–1079. https://doi.org/10.1515/nanoph-2019-0504

Qiu, C., Gan, S., Xiang, Y., & Dai, X. (2021). High Figure of Merit in Lossy Mode Resonance Sensors with PtSe2 Thin Film. *Plasmonics*, *16*(3), 729–735. https://doi.org/10.1007/s11468-020-01337-x

Ruffato, G., Pasqualotto, E., Sonato, A., Zacco, G., Silvestri, D., Morpurgo, M., De Toni, A., & Romanato, F. (2013). Implementation and testing of a compact and high-resolution sensing device based on grating-coupled surface plasmon resonance with polarization modulation. *Sensors and Actuators, B: Chemical*, *185*, 179–187. https://doi.org/10.1016/j.snb.2013.04.113

Rupert, D. L. M., Mapar, M., Shelke, G. V., Norling, K., Elmeskog, M., Lötvall, J. O., Block, S., Bally, M., Agnarsson, B., & Höök, F. (2018). Effective Refractive Index and Lipid Content of Extracellular Vesicles Revealed Using Optical Waveguide Scattering and Fluorescence Microscopy. *Langmuir*, *34*(29), 8522–8531. https://doi.org/10.1021/acs.langmuir.7b04214

Saini, G. S. S., Kaur, S., Tripathi, S. K., Mahajan, C. G., Thanga, H. H., & Verma, A. L. (2005). Spectroscopic studies of rhodamine 6G dispersed in polymethylcyanoacrylate. *Spectrochimica Acta - Part A: Molecular and Biomolecular Spectroscopy*, *61*(4), 653–658. https://doi.org/10.1016/j.saa.2004.05.022

Saini, R., Kumar, A., Bhatt, G., Kapoor, A., Paliwal, A., Tomar, M., & Gupta, V. (2020). Lossy Mode Resonance-Based Refractive Index Sensor for Sucrose Concentration Measurement. *IEEE Sensors Journal*, *20*(3), 1217–1222. https://doi.org/10.1109/JSEN.2019.2946760

Scardamaglia, M., Boix, V., D'Acunto, G., Struzzi, C., Reckinger, N., Chen, X., Shivayogimath, A., Booth, T., & Knudsen, J. (2021). Comparative study of copper oxidation protection with graphene and hexagonal boron nitride. *Carbon*, *171*, 610–617. https://doi.org/10.1016/j.carbon.2020.09.021

Semwal, V., & Gupta, B. D. (2020). Lossy mode resonance-based highly sensitive fiber optic refractive index sensor using the bilayer of FTO/HfO 2 for operation in the visible region. *Journal of the Optical Society of America B*, *37*(12), 3841. https://doi.org/10.1364/JOSAB.404670

Semwal, V., Jensen, O. R., Bang, O., & Janting, J. (2023). Investigation of Performance Parameters of Spherical Gold Nanoparticles in Localized Surface Plasmon Resonance Biosensing. *Micromachines*, *14*(9), 1717. https://doi.org/10.3390/mi14091717

Seo, W. S., Kim, D. K., Han, J.-H., Park, K.-B., Ryu, S. C., Min, N. K., & Kim, J. H. (2020). Functionalization of Molybdenum Disulfide via Plasma Treatment and 3-Mercaptopropionic Acid for Gas Sensors. *Nanomaterials*, *10*(9), 1860. https://doi.org/10.3390/nano10091860

Serebrennikova, K. V., Berlina, A. N., Sotnikov, D. V., Dzantiev, B. B., & Zherdev, A. V. (2021). Raman scattering-based biosensing: New prospects and opportunities. *Biosensors*, *11*(12). https://doi.org/10.3390/bios11120512

Shajari, D., Bahari, A., & Gill, P. (2018). Fast and simple detection of bovine serum albumin concentration by studying its interaction with gold nanorods. *Colloids and Surfaces A: Physicochemical and Engineering Aspects*, *543*(February), 118–125. https://doi.org/10.1016/j.colsurfa.2018.02.008

Shen, Y., Zhu, Q., Chen, Z., Wu, J., Chen, B., Dai, E., & Pan, W. (2024). Lossy Mode Resonance Sensors Based on Anisotropic Few-Layer Black Phosphorus. *Nanomaterials*, *14*(9). https://doi.org/10.3390/nano14090736

Shim, S., Stuart, C. M., & Mathies, R. A. (2008). Resonance Raman Cross-Sections and Vibronic Analysis of Rhodamine 6G from Broadband Stimulated Raman Spectroscopy. *ChemPhysChem*, *9*(5), 697–699. https://doi.org/10.1002/cphc.200700856

Shrivastav, A. M., Satish, L., Kushmaro, A., Shvalya, V., Cvelbar, U., & Abdulhalim, I. (2021). Engineering the penetration depth of nearly guided wave surface plasmon resonance towards application in bacterial cells monitoring. *Sensors and Actuators B: Chemical*, *345*(March), 130338. https://doi.org/10.1016/j.snb.2021.130338

Shukri, W. N. W., Bidin, N., Islam, S., Krishnan, G., Bakar, M. A. A., & Affandi, M. S. (2016). Synthesis and characterization of uncoated and cysteamine-coated gold nanoparticles by pulsed laser ablation. *Journal of Nanophotonics*, *10*(4), 046007. https://doi.org/10.1117/1.jnp.10.046007

Sicacha, M. S., Minkovich, V. P., Sotsky, A. B., Shilov, A. V., Sotskaya, L. I., & Chudakov, E. A. (2021). Lossy mode resonances in photonic crystal fibers. *Journal of the European Optical Society-Rapid Publications*, *17*(1). https://doi.org/10.1186/s41476-021-00169-4

Singh, R., Wang, Z., Marques, C., Min, R., Zhang, B., & Kumar, S. (2023). Alanine aminotransferase detection using TIT assisted four tapered fiber structure-based LSPR sensor: From healthcare to marine life. *Biosensors and Bioelectronics*, *236*(May), 115424. https://doi.org/10.1016/j.bios.2023.115424

Song, C., Jiang, X., Yang, Y., Zhang, J., Larson, S., Zhao, Y., & Wang, L. (2020). High-Sensitive Assay of Nucleic Acid Using Tetrahedral DNA Probes and DNA Concatamers with a Surface-Enhanced Raman Scattering/Surface Plasmon Resonance Dual-Mode Biosensor Based on a Silver Nanorod-Covered Silver

Nanohole Array. *ACS Applied Materials and Interfaces*, *12*(28), 31242–31254. https://doi.org/10.1021/acsami.0c08453

Song, C., Zhang, J., Jiang, X., Gan, H., Zhu, Y., Peng, Q., Fang, X., Guo, Y., & Wang, L. (2021). SPR/SERS dual-mode plasmonic biosensor via catalytic hairpin assembly-induced AuNP network. *Biosensors and Bioelectronics*, *190*(May), 113376. https://doi.org/10.1016/j.bios.2021.113376

Sridhar, K., Inbaraj, B. S., & Chen, B. H. (2022). An improved surface enhanced Raman spectroscopic method using a paper-based grape skin-gold nanoparticles/graphene oxide substrate for detection of rhodamine 6G in water and food. *Chemosphere*, *301*(March), 134702. https://doi.org/10.1016/j.chemosphere.2022.134702

StellarNet, I. (2025). *Raman Spectroscopy Accessories*. https://www.stellarnet.us/wp-content/uploads/RamuLaser.pdf

Sun, H., Li, D., Yue, X., Hong, R., Yang, W., Liu, C., Xu, H., Lu, J., Dong, L., Wang, G., & Li, D. (2022). A Review of Transition Metal Dichalcogenides-Based Biosensors. *Frontiers in Bioengineering and Biotechnology*, *10*(June), 1–11. https://doi.org/10.3389/fbioe.2022.941135

Szunerits, S., Maalouli, N., Wijaya, E., Vilcot, J.-P., & Boukherroub, R. (2013). Recent advances in the development of graphene-based surface plasmon resonance (SPR) interfaces. *Analytical and Bioanalytical Chemistry*, *405*(5), 1435–1443. https://doi.org/10.1007/s00216-012-6624-0

Tene, T., Arias Arias, F., Paredes-Páliz, K. I., Haro-Barroso, C., & Vacacela Gomez, C. (2024). An Optimized Graphene-Based Surface Plasmon Resonance Biosensor for Detecting SARS-CoV-2. *Applied Sciences*, *14*(22), 10724. https://doi.org/10.3390/app142210724

Terdale, S., & Tantray, A. (2017). Spectroscopic study of the dimerization of rhodamine 6G in water and different organic solvents. *Journal of Molecular Liquids*, *225*, 662–671. https://doi.org/10.1016/j.molliq.2016.10.090

Tien, C. L., Lin, H. Y., & Su, S. H. (2018). High Sensitivity Refractive Index Sensor by D-Shaped Fibers and Titanium Dioxide Nanofilm. *Advances in Condensed Matter Physics*, *2018*. https://doi.org/10.1155/2018/2303740

Usha, S. P., Shrivastav, A. M., & Gupta, B. D. (2018). Semiconductor metal oxide/polymer based fiber optic lossy mode resonance sensors: A contemporary study. *Optical Fiber Technology*, *45*(May), 146–166. https://doi.org/10.1016/j.yofte.2018.07.003

Vala, M., Chadt, K., Piliarik, M., & Homola, J. (2010). High-performance compact SPR

sensor for multi-analyte sensing. *Sensors and Actuators, B: Chemical*, *148*(2), 544–549. https://doi.org/10.1016/j.snb.2010.05.067

Villar, I. Del, Arregui, F. J., Zamarreño, C. R., Corres, J. M., Bariain, C., Goicoechea, J., Elosua, C., Hernaez, M., Rivero, P. J., Socorro, A. B., Urrutia, A., Sanchez, P., Zubiate, P., Lopez, D., De Acha, N., Ascorbe, J., & Matias, I. R. (2017). Optical sensors based on lossy-mode resonances. *Sensors and Actuators B: Chemical*, *240*, 174–185. https://doi.org/10.1016/j.snb.2016.08.126

Villar, I. Del, Torres, V., & Beruete, M. (2015). Experimental demonstration of lossy mode and surface plasmon resonance generation with Kretschmann configuration. *Optics Letters*, *40*(20), 4739. https://doi.org/10.1364/ol.40.004739

Villar, I. Del, Zamarreño, C. R., Hernaez, M., Arregui, F. J., & Matias, I. R. (2010). Lossy mode resonance generation with indium-tin-oxide-coated optical fibers for sensing applications. *Journal of Lightwave Technology*, *28*(1), 111–117. https://doi.org/10.1109/JLT.2009.2036580

Waghmare, M., Khade, B., Chaudhari, P., & Dongre, P. (2018). Multiple layer formation of bovine serum albumin on silver nanoparticles revealed by dynamic light scattering and spectroscopic techniques. *Journal of Nanoparticle Research*, *20*(7), 185. https://doi.org/10.1007/s11051-018-4286-3

Wang, D., He, P., Wang, Z., Li, G., Majed, N., & Gu, A. Z. (2020). Advances in single cell Raman spectroscopy technologies for biological and environmental applications. *Current Opinion in Biotechnology*, *64*(July), 218–229. https://doi.org/10.1016/j.copbio.2020.06.011

Wang, H., He, Y., Zhang, J., & Xu, Y. (2022). Highly sensitive refractive index sensor based on the lossy mode resonance enhanced photonic spin Hall effect. *Journal of the Optical Society of America B*, *39*(11), 2992. https://doi.org/10.1364/JOSAB.472718

Wang, H., Wang, T., Yuan, X., Wang, Y., Yue, X., Wang, L., Zhang, J., & Wang, J. (2023). Plasmonic Nanostructure Biosensors: A Review. *Sensors*, *23*(19), 8156. https://doi.org/10.3390/s23198156

Wang, X., Wang, C., Sun, X., Li, X., Liu, H., Sun, X., Wang, F., Lu, X., & Huang, C. (2021). Locally excited surface plasmon resonance for refractive index sensing with high sensitivity and high resolution. *Optics Letters*, *46*(15), 3625. https://doi.org/10.1364/ol.432385

Wang, Y., Mao, Z., Chen, Q., Koh, K., Hu, X., & Chen, H. (2022). Rapid and sensitive

detection of PD-L1 exosomes using Cu-TCPP 2D MOF as a SPR sensitizer. *Biosensors and Bioelectronics*, *201*(December 2021), 113954. https://doi.org/10.1016/j.bios.2021.113954

Wang, Y., Xu, C., Zhou, Y., Lee, J., Chen, Q., & Chen, H. (2024). Interface-Engineered 2D Heterojunction with Photoelectric Dual Gain: Mxene@MOF-Enhanced SPR Spectroscopy for Direct Sensing of Exosomes. *Small*, *20*(23), 1–20. https://doi.org/10.1002/smll.202308897

Wangüemert-Pérez, J. G., Hadij-ElHouati, A., Sánchez-Postigo, A., Leuermann, J., Xu, D. X., Cheben, P., Ortega-Moñux, A., Halir, R., & Molina-Fernández, Í. (2019). Subwavelength structures for silicon photonics biosensing. *Optics and Laser Technology*, *109*, 437–448. https://doi.org/10.1016/j.optlastec.2018.07.071

Watanabe, H., Hayazawa, N., Inouye, Y., & Kawata, S. (2005). DFT Vibrational Calculations of Rhodamine 6G Adsorbed on Silver: Analysis of Tip-Enhanced Raman Spectroscopy. *The Journal of Physical Chemistry B*, *109*(11), 5012–5020. https://doi.org/10.1021/jp045771u

Wu, L., Wang, Q., Ruan, B., Zhu, J., You, Q., Dai, X., & Xiang, Y. (2018). High-Performance Lossy-Mode Resonance Sensor Based on Few-Layer Black Phosphorus. *The Journal of Physical Chemistry C*, *122*(13), 7368–7373. https://doi.org/10.1021/acs.jpcc.7b12549

Wu, L., Zhu, J., Gan, S., Ma, Q., Dai, X., & Xiang, Y. (2019). Application of Few-Layer Transition Metal Dichalcogenides to Detect the Refractive Index Variation in Lossy-Mode Resonance Sensors with High Figure of Merit. *IEEE Sensors Journal*, *19*(13), 5030–5034. https://doi.org/10.1109/JSEN.2019.2904199

Xu, Y., Wu, L., & Ang, L. K. (2019). Surface exciton polaritons: A promising mechanism for refractive-index sensing. *Physical Review Applied*, *12*(2). https://doi.org/10.1103/PhysRevApplied.12.024029

Yamamoto, Y. S., Ozaki, Y., & Itoh, T. (2014). Recent progress and frontiers in the electromagnetic mechanism of surface-enhanced Raman scattering. *Journal of Photochemistry and Photobiology C: Photochemistry Reviews*, *21*, 81–104. https://doi.org/10.1016/j.jphotochemrev.2014.10.001

Yang, H., Giri, A., Moon, S., Shin, S., Myoung, J.-M., & Jeong, U. (2017). Highly Scalable Synthesis of MoS 2 Thin Films with Precise Thickness Control via Polymer-Assisted Deposition. *Chemistry of Materials*, *29*(14), 5772–5776. https://doi.org/10.1021/acs.chemmater.7b01605

Yang, P., Yao, S., Wei, W., & Cai, J. (2011). An Indirect Immunoassay for Detecting Antigen Based on Fluorescence Resonance Energy Transfer. *American Journal of Analytical Chemistry*, *02*(04), 484–490. https://doi.org/10.4236/ajac.2011.24058

Yang, Y., Murray, J., Haverstick, J., Tripp, R. A., & Zhao, Y. (2022). Silver nanotriangle array based LSPR sensor for rapid coronavirus detection. *Sensors and Actuators B: Chemical*, *359*(January), 131604. https://doi.org/10.1016/j.snb.2022.131604

Yari, A., & Saeidikhah, M. (2015). Ultra-trace electrochemical impedance determination of bovine serum albumin by a two dimensional silica network citrate-capped gold nanoparticles modified gold electrode. *Talanta*, *144*, 1336–1341. https://doi.org/10.1016/j.talanta.2015.08.019

Yasli, A. (2021). Cancer Detection with Surface Plasmon Resonance-Based Photonic Crystal Fiber Biosensor. *Plasmonics*, *16*(5), 1605–1612. https://doi.org/10.1007/s11468-021-01425-6

Yoo, J., Han, S., Park, B., Sonwal, S., Alhammadi, M., Kim, E., Aliya, S., Lee, E. S., Jeon, T. J., Oh, M. H., & Huh, Y. S. (2022). Highly Specific Peptide-Mediated Cuvette-Form Localized Surface Plasmon Resonance (LSPR)-Based Fipronil Detection in Egg. *Biosensors*, *12*(11). https://doi.org/10.3390/bios12110914

Zamarreño, C. R., Sanchez, P., Hernaez, M., Villar, I. Del, Fernandez-Valdivielso, C., Matias, I. R., & Arregui, F. J. (2010). Dual-peak resonance-based optical fiber refractometers. *IEEE Photonics Technology Letters*, *22*(24), 1778–1780. https://doi.org/10.1109/LPT.2010.2082517

Zhang, H., Zhou, X., Li, X., Gong, P., Zhang, Y., & Zhao, Y. (2023). Recent Advancements of LSPR Fiber-Optic Biosensing: Combination Methods, Structure, and Prospects. *Biosensors*, *13*(3). https://doi.org/10.3390/bios13030405

Zhang, J., Srivatsa, P., Ahmadzai, F. H., Liu, Y., Song, X., Karpatne, A., Kong, Z., & Johnson, B. N. (2023). Reduction of Biosensor False Responses and Time Delay Using Dynamic Response and Theory-Guided Machine Learning. *ACS Sensors*, *8*(11), 4079–4090. https://doi.org/10.1021/acssensors.3c01258

Zhang, J., Wang, X., & Yang, X. (2012). Colorimetric determination of hypochlorite with unmodified gold nanoparticles through the oxidation of a stabilizer thiol compound. *Analyst*, *137*(12), 2806–2812. https://doi.org/10.1039/c2an35239g

Zhang, S., Qi, Y., Tan, S. P. H., Bi, R., & Olivo, M. (2023). Molecular Fingerprint Detection Using Raman and Infrared Spectroscopy Technologies for Cancer Detection: A Progress Review. *Biosensors*, *13*(5). https://doi.org/10.3390/bios13050557

Zhang, Y., Zhang, P., Zhao, M., Li, Z., Xu, D., Tong, C., Shen, J., & Li, C. (2022). Theoretical modeling and investigations of lossy mode resonance prism sensor based on TiO 2 film . *Optics Express*, *30*(18), 32483. https://doi.org/10.1364/oe.466170

Zhang, Y., Zheng, guo, & Wang. (2011). Biosynthesis of gold nanoparticles using chloroplasts. *International Journal of Nanomedicine*, *6*, 2899. https://doi.org/10.2147/IJN.S24785

Zheng, L., Hu, F., Zhao, Y., Zhu, J., Wang, X., Su, M., & Liu, H. (2023). Core–Satellite Nanoassemblies as SPR/SERS Dual-Mode Plasmonic Sensors for Sensitively Detecting Ractopamine in Complex Media. *Journal of Agricultural and Food Chemistry*, *71*(51), 20793–20800. https://doi.org/10.1021/acs.jafc.3c06475

Zhong, F., Wu, Z., Guo, J., & Jia, D. (2018). Porous Silicon Photonic Crystals Coated with Ag Nanoparticles as Efficient Substrates for Detecting Trace Explosives Using SERS. *Nanomaterials*, *8*(11), 872. https://doi.org/10.3390/nano8110872

Zhou, Y., Wang, M., Wang, J., Shi, J., Zhang, C., Da, Z., Xu, Y., Ji, Y., Gaponenko, N. V., & Bhatti, A. S. (2025). Surface-enhanced Raman scattering of R6G dimerization during self-healing of gel. *Microchimica Acta*, *192*(1), 48. https://doi.org/10.1007/s00604-024-06918-9

Zrimsek, A. B., Henry, A. I., & Van Duyne, R. P. (2013). Single molecule surface-enhanced raman spectroscopy without nanogaps. *Journal of Physical Chemistry Letters*, *4*(19), 3206–3210. https://doi.org/10.1021/jz4017574

Appendices

Appendix A : TEM and Zeta potential characterization results of AuNPs

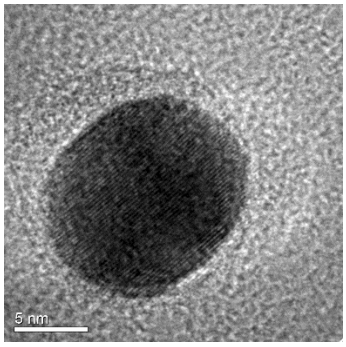

(a)

Results

			Size (d.n...	% Number:	St Dev (d.n...
Z-Average (d.nm):	55.97	Peak 1:	16.05	100.0	4.944
PdI:	0.442	Peak 2:	0.000	0.0	0.000
Intercept:	0.905	Peak 3:	0.000	0.0	0.000
Result quality	Good				

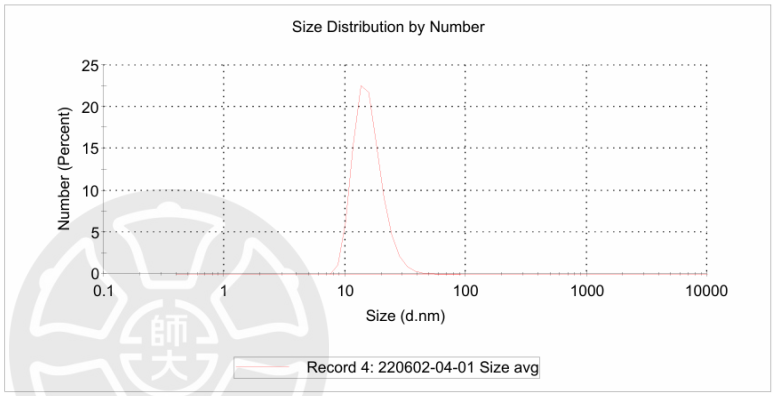

(b)

Figure A1. TEM and zeta potential characterization results of bare AuNPs

Appendix B: Raman peak of Rhodamine 6G

Raman spectroscopy is a characterization technique that is very sensitive to the physical and chemical conditions of the sample, including the molecular form (monomer, dimer, or aggregate), the type of substrate used, and the signal acquisition system and method. In this study, significant spectral differences were observed between measurements using micro-Raman and fiber-optic Raman, both in terms of Raman peak positions and their relative intensities. The three main factors that influence these differences are the measurement conditions (dry or in solution), the presence of AuNPs substrate, and the type of Raman system used.

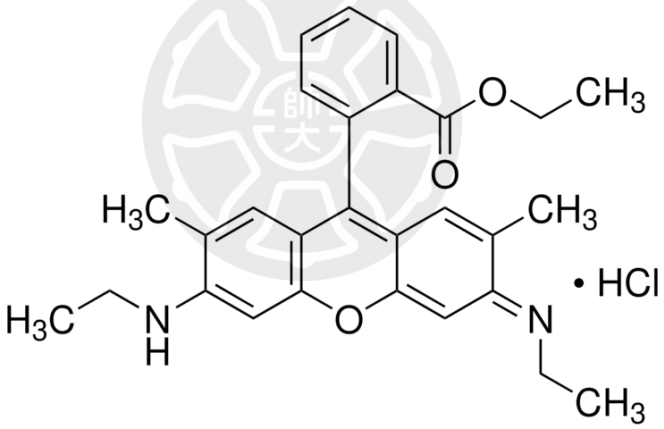

Figure B1. Chemical structure of R6G. Adapted with permission from Ref. (Al-Jarwany et al., 2024)*, copyright Springer.*

To evaluate the effect of the Raman system on the resulting signal, a comparison was made between the Raman spectra of micro-Raman (MRI-Raman, ProTrusTech Co., Ltd., Taiwan) and fiber-optic Raman (StellarNet, Inc.). The molecular structure of R6G is shown in Figure B1 to provide context for the vibrational modes observed in the spectra. The results of the R6G measurements using micro-

Raman are shown in Figure B2, with the complete identified Raman peaks presented in Table B1. Based on these data, the R6G spectrum measured without the addition of AuNPs did not display any characteristic peaks. However, after the addition of AuNPs, the Raman spectrum showed clearly defined peaks typical of R6G. In addition, a comparison of the two excitation wavelengths, 532 nm and 785 nm, showed that the excitation at 532 nm resulted in a higher signal intensity due to the resonance effect, since this wavelength is closer to the electronic absorption band of R6G (Pál et al., 2021).

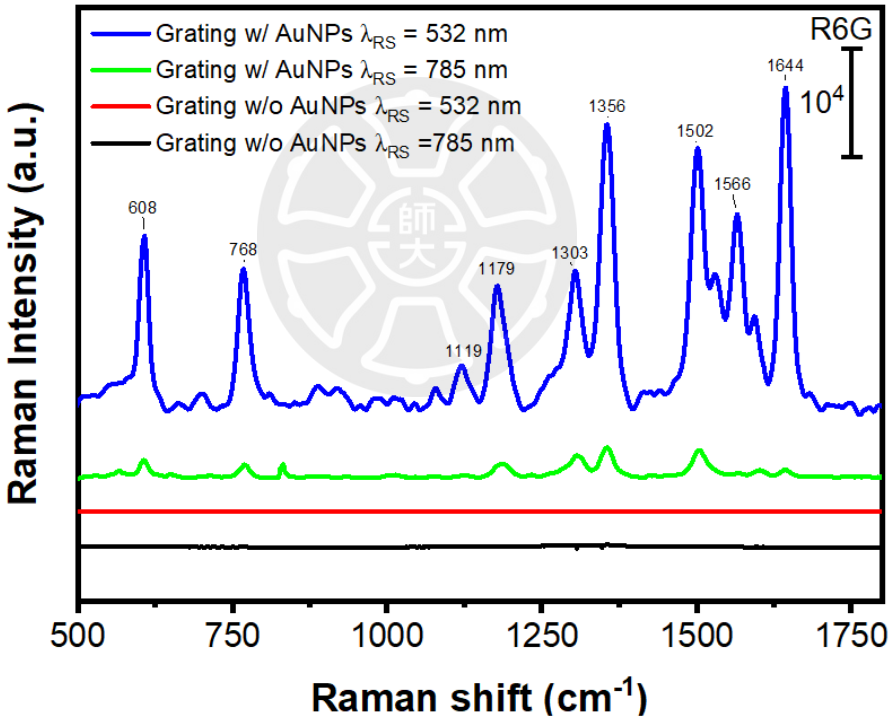

Figure B2. Comparison of R6G signals with two different excitation wavelength (532 nm and 785 nm) and measured using micro-Raman on samples with (w/) and without (w/o) AuNPs.

Technically, the micro-Raman system has a small depth of focus (about 1 μm) and an axial resolution close to 2 μm (Foucher, 2022)(Novák et al., 2016)(Jung et al., 2022), which makes it more suitable for the measurement of samples in dry

conditions. The limited detection volume causes the signal acquisition to originate only from molecules located very close to the substrate surface. Therefore, the detected signal mainly originates from R6G molecules adsorbed on AuNPs, most likely in the form of monomers.

Table B1. Raman peak which is obtained from micro-Raman measurements

Raman shift (cm^{-1})	**Vibration**	**Ref**
608	C–C–C bending vibrations in xanthene ring	(Y. Zhang et al., 2011)
768	C–H bending vibrations in xanthene or phenyl ring	(Y. C. Liu et al., 2006)
1122	C–H bending vibrations in xanthene or phenyl ring	(Sridhar et al., 2022)
1179	C–H bending vibrations in xanthene or phenyl ring	
1303	symmetric modes of in-plane C–C stretching vibrations in xanthene or phenyl ring	(Y. Zhang et al., 2011)
1356	symmetric modes of in-plane C–C stretching vibrations in xanthene or phenyl ring	(Sridhar et al., 2022)
1502	symmetric modes of in-plane C–C stretching vibrations in xanthene or phenyl ring	(He et al., 2012)
1566	symmetric modes of in-plane C–C stretching vibrations in xanthene or phenyl ring	(Sridhar et al., 2022)
1644	symmetric modes of in-plane C–C stretching vibrations in xanthene or phenyl ring	(Y. Zhang et al., 2011)

In contrast, the fiber-optic Raman system shows higher signal intensity when the measurements are performed in solution. The difference in Raman signals measured in dry and solution is shown in Figure B3. This is due to the increased effective detection volume in the liquid phase. With a larger spot diameter (up to 250 µm (Artemyev & Shatskaya, 2022)) and an axial resolution of up to 1 mm (StellarNet, 2025), the system is able to sample signals from more molecules in the sample. In liquid conditions, more molecules are in the excitation and detection path, resulting in a larger interaction volume and a stronger Raman signal. Therefore, the physical

condition of the sample (dry or solution) greatly affects the quality and intensity of the Raman signal.

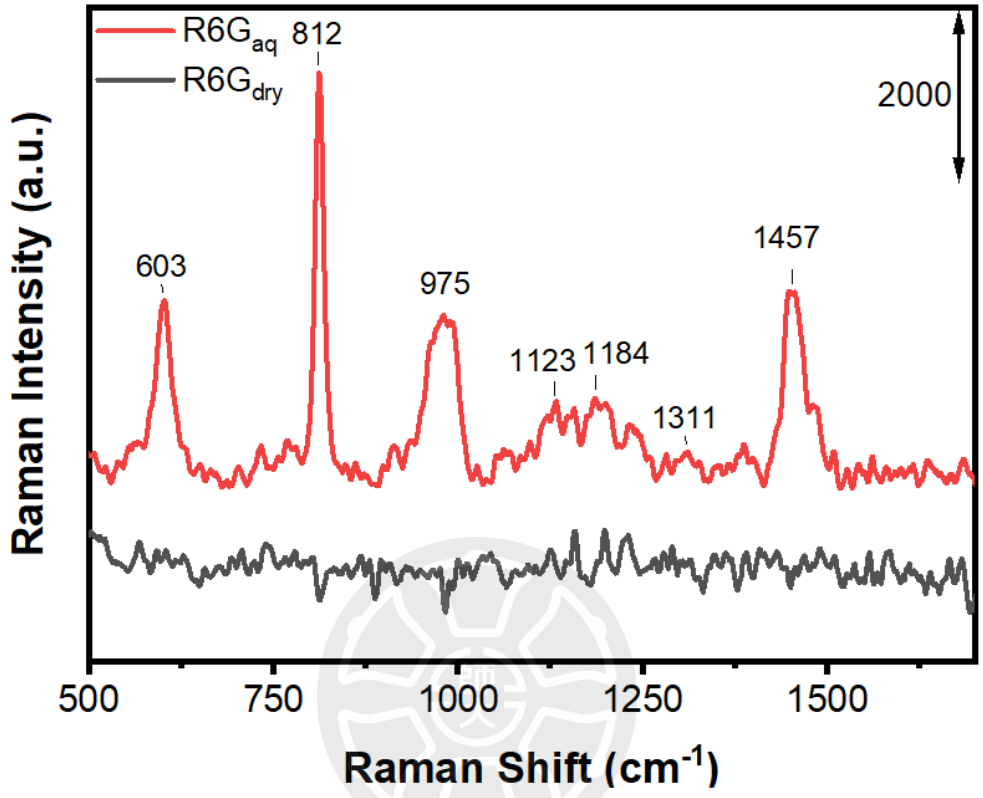

Figure B3. Raman spectra were recorded under both dry (black) and aqueous (red) conditions using a fiber-optic Raman system with 785 nm excitation.

The results of Raman measurements of fiber-optic Raman in dry and solution conditions are shown in Figure B3, while the list of detected Raman peaks is presented in Table B2. Some Raman peaks show the same position as the data obtained from the micro-Raman measurement results. Some of them are peaks which are at Raman shifts of 1123 cm^{-1} and 1184 cm^{-1}. However, some peaks which have prominent intensities have different positions from the peaks obtained from the micro-Raman measurements. For example, C–C–C bending vibrations in xanthene ring and C–H bending vibrations in xanthene or phenyl ring are detected at Raman

shifts of 608 cm^{-1} and 768 cm^{-1}. The measured peaks are actually influenced by the measurement conditions and the type of substrate used. Khosroshahi et al. conducted Raman measurements on a gold thin film substrate immobilized with gold nanourchins with a Raman excitation wavelength of 632 nm (Khosroshahi et al., 2025). The results of the peak in this area were found at Raman shift 653 cm^{-1} and 824 cm^{-1}. Different researchers, namely Zhou et al., used silver gel particles as Raman substrates and the results found rare peak characteristics such as at 820 cm^{-1} and they stated that this peak was related to the phenomenon of R6G molecule dimerization (Zhou et al., 2025).

Table B2. Raman peak assignment of Rhodamine 6G (R6G)

Raman shift (cm^{-1})	**Raman peak assignment**
603	C–C–C ring in-plane bending (Zrimsek et al., 2013)(Bartolowits et al., 2019)(W. Liu et al., 2023)
812	symmetric stretching or out-of-plane wagging of the xanthene ring (Zhou et al., 2025)
975	weak C–H in-plane bend (Watanabe et al., 2005)
1123	C–H bending vibrations in xanthene or phenyl ring (Pal & Varma, 2024)(Sridhar et al., 2022)(He et al., 2012)
1184	C–H bending vibrations in xanthene or phenyl ring (Pal & Varma, 2024)(Sridhar et al., 2022)(He et al., 2012)
1311	C-O-C vibrations (Pal & Varma, 2024)
1457	C–N stretching in NHC_2H_5 (Khosroshahi et al., 2025)(Zhong et al., 2018)

In this study, two peaks in this area were detected at Raman shift 603 cm^{-1} and 812 cm^{-1}. Based on Zrimsek and Bartolowits' research (Zrimsek et al., 2013)(Bartolowits et al., 2019)(W. Liu et al., 2023), the Peak at Raman shift 603 cm^{-1} shows one of the indicators of dimer signals (dimer structure and different orientations are shown in Figure B4). Likewise, the Raman peak at 812 cm^{-1} in this

spectrum is very likely related to the specific orientation of the R6G molecule during dimerization, as explained by Zhou et al. (2025) (Zhou et al., 2025). Based on the results of harmonic vibration simulations carried out with the B3LYP/6-31G(d) level of theory, it is known that the peaks around 810–820 cm^{-1} reflect the symmetric stretching vibration modes of the xanthene ring and the out-of-plane wagging of the ethyl group. However, Zhou et al. also showed that the geometry and orientation of the molecules in the dimer structure play a key role in generating these peaks.

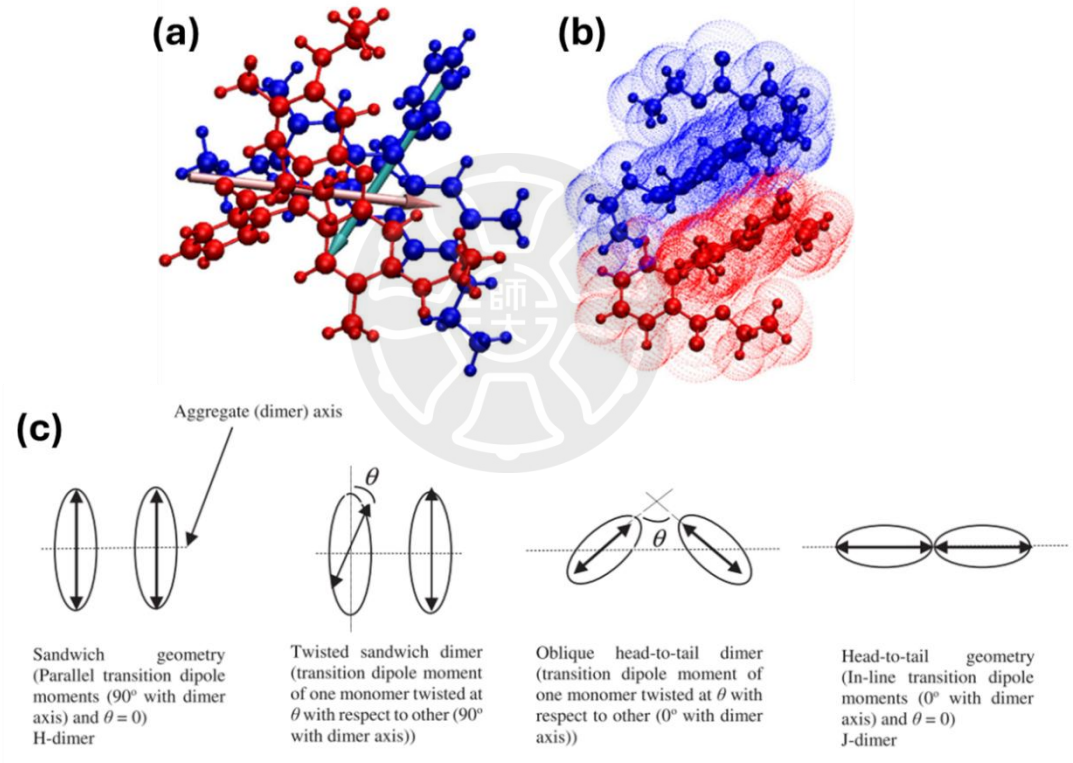

Figure B4. The R6G dimer structure is shown in three views: (a) top, showing the direction of the dipole moment; (b) side, showing the relative positions of the molecules; and (c) the location of the transition dipole moment in the dimer form. Figure composed of elements adapted from Ref. (Doveiko et al., 2023) *(licensed under CC BY 4.0) and Ref.* (Terdale & Tantray, 2017) *(with permission from Elsevier).*

In the Raman shift range of 900–1000 cm^{-1}, several previous studies have reported the emergence of several characteristic peaks of R6G. Among them, Shim

et al. observed a peak at 917 cm^{-1} (Shim et al., 2008), Guthmuller and Champagne at 924 cm^{-1}(Guthmuller & Champagne, 2008), and Watanabe et al. at 978 cm^{-1}(Watanabe et al., 2005). According to Majoube and Henry, the peaks in this range are active peaks, which is evidenced by the comparison of the spectra between surface-enhanced Raman spectroscopy (SER) and surface-enhanced resonance Raman spectroscopy (SERR) signals (Majoube & Henry, 1991). In the SERR experiment, a peak appeared at a Raman shift of 933 cm^{-1}, which was not detected in the SER spectrum. This peak was attributed to the vibrational mode involving the deformation of the xanthene ring. In this study, the R6G peak around 900–1000 cm^{-1} was identified at Raman shift 975 cm^{-1}, which according to Watanabe et al. was related to the bending or stretching motion of the phenyl ring plane (Watanabe et al., 2005). In addition, another dominant peak was observed at 1457 cm^{-1}, which was related to the stretching of the C–N bond in the NHC_2H_5 group, as reported in the following literature (Khosroshahi et al., 2025)(Zhong et al., 2018). These two peaks, namely 975 cm^{-1} and 1457 cm^{-1}, have quite dominant intensities. Several studies have revealed the phenomenon of signal changes from initially weak to very intense intensity and this can be caused by changes in the orientation of the molecules (Marshall et al., 2017), Raman scattering enhanced by aggregation (Akins et al., 1997) and also intermolecular coupling in the aggregates (Coles et al., 2010).

The difference between the results shown by Micro-Raman and fiber optic Raman measurements indicates a change in the detected molecular structure, which is most likely related to the aggregation state in solution. The fiber-optic Raman system has a wider and deeper detection volume, because the excitation light and

signal collection are sent through the optical fiber, so that the signals obtained are more representative of the molecules in the bulk solution. Therefore, the resulting signal mainly comes from R6G molecules that are homogeneously distributed in solution, including the possible presence of dimers or aggregates formed due to concentration and environmental conditions.

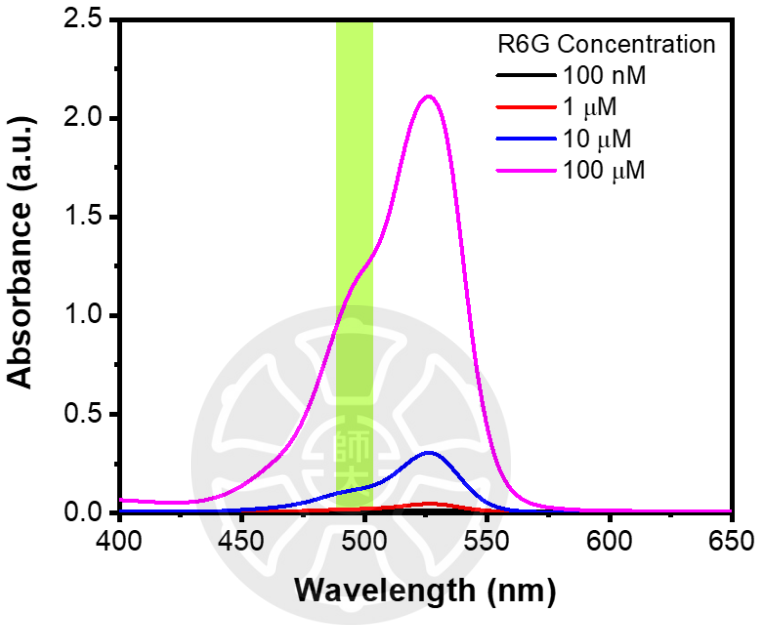

Figure B5. Absorbance profiles of R6G solutions with different concentrations. The shoulder indicated by the green area confirms the formation of dimers.

The change in molecular structure from monomer to dimer was further confirmed through UV-Vis characterization. Figure B5 shows the absorbance spectrum of R6G at various concentrations, ranging from 100 nM to 100 μM. The main absorption band which is characteristic of R6G is located at a wavelength of 526 nm and the spectrum also shows the appearance of a shoulder around 498 nm, which has been reported as a typical indicator of the formation of H-type dimers based on several references (G. S. S. Saini et al., 2005)(Terdale & Tantray, 2017)(Purcar et al., 2008). This shoulder indicates the presence of π–π stacking

interactions between aromatic molecules in face-to-face orientation, which causes exciton coupling between molecules. Therefore, the presence of this shoulder is strong evidence for the formation of dimer structures in solutions.

The type of Raman system and the substrate used significantly affect the types of molecules detected. Micro-Raman systems with AuNPs substrates amplify signals from molecules located very close to the metal surface, and because the sample is dried, R6G molecules are less likely to interact with each other and remain in monomeric form. In contrast, fiber-optic Raman has a wider detection volume and measures molecules in solution throughout. Under these conditions, molecular aggregation such as dimerization is not only possible but also becomes the dominant form.

It should be noted that the position and intensity of Raman peaks can be affected by various factors, including experimental conditions (such as laser intensity, excitation wavelength, and solvent type and polarity), the type of substrate used (e.g., flat metal surfaces, nanoparticles, or porous structures), and specific interactions between R6G molecules and the substrate surface or surrounding environment (Haran et al., 2010)(W. H. Li et al., 1999)(C. Lu et al., 2019). In a study by Majoube and Henry (Majoube & Henry, 1991), the use of an excitation wavelength resonant with the R6G electronic transition resulted in the appearance of a specific Raman peak at 933 cm^{-1}, which was not observed under off-resonance conditions, indicating the importance of excitation selection in eliciting a specific vibrational mode. In addition, the influence of the substrate has also been investigated by Li and co-workers (W. H. Li et al., 1999), who prepared substrates with different degrees of

roughness by electrochemical methods. They found that the Raman signal enhancement depends not only on the type of metal and its surface roughness, but also on the type of molecules adsorbed on the electrode. Therefore, the differences in peaks observed in this study most likely reflect the contribution of one or more of these factors.

All the Raman peaks identified in this study have been discussed in detail. Of the six peaks observed, five were considered to be dominant, namely at 603, 812, 975, 1184, and 1457 cm^{-1}. The differences in Raman intensity of these five peaks caused by the effects of the substrate used and the SPR excitation wavelength are discussed in depth in Chapter 3 of this dissertation.

Appendix C : Transfer Matrix Method

Transfer Matrix Method (TMM) is a mathematical method used to analyze the propagation of electromagnetic waves through layered structures. These structures consist of layers of material with a certain thickness (d) and refractive index (n), each of which can affect how the wave is reflected, transmitted, or trapped. In TMM, the relationship of the electromagnetic fields is expressed in the form of a total matrix:

$$\begin{bmatrix} U_1 \\ V_1 \end{bmatrix} = M \begin{bmatrix} U_{N-1} \\ V_{N-1} \end{bmatrix} \tag{1}$$

where V and U represent the magnetic and electric field components at the boundary surface. In the above equation, M denotes the matrix feature of the stacked structure which is defined as:

$$M = \prod_{k=2}^{N-1} M_k = \begin{bmatrix} M_{11} & M_{12} \\ M_{21} & M_{22} \end{bmatrix} \tag{2}$$

Where,

$$M_k = \begin{bmatrix} \cos\beta_k & -\sin\beta_k/q_k \\ -iq_k \sin\beta_k & \cos\beta_k \end{bmatrix} \tag{3}$$

In equation 3, q_k and β_k are defined as:

$$q_k = \frac{\sqrt{(\varepsilon_k - {n_1}^2 \sin^2\theta_1)}}{\varepsilon_k} \quad \text{(p-pol)} \tag{4}$$

$$q_k = \sqrt{(\varepsilon_k - {n_1}^2 \sin^2\theta_1)} \quad \text{(s-pol)} \tag{5}$$

$$\beta_k = \frac{2\pi d_k}{\lambda} \sqrt{(\varepsilon_k - {n_1}^2 \sin\theta_1)} \tag{6}$$

Here, the incident angle is θ_1. The total reflection coefficient is expressed as:

$$\mathrm{r} = \frac{(M_{11} + M_{12}q_N)q_1 - (M_{21} + M_{22}q_N)}{(M_{11} + M_{12}q_N)q_1 + (M_{21} + M_{22}q_N)} \tag{7}$$

Finally, we can derive that the reflectance (R) of the N-layer model is:

$$R = |\mathrm{r}|^2 \qquad [8]$$

Appendix D : LMR sensor response to different refractive indices of sensing medium

Figure D1 illustrates the influence of varying thicknesses of the matching and lossy layers on the sensor response as the refractive index of the sensing medium increases. As observed in Figures D1(a) and D1(b), LMR sensors with thicker Cytop layers exhibit a narrower detection range. Specifically, the LMR sensor with a 1200 nm-thick Cytop layer can only detect analytes with a refractive index below 1.385. In general, LMR sensors excited with p-polarized light show poor signal stability, as evidenced by significant fluctuations in minimum reflectance in response to changes in the refractive index of the sensing environment.

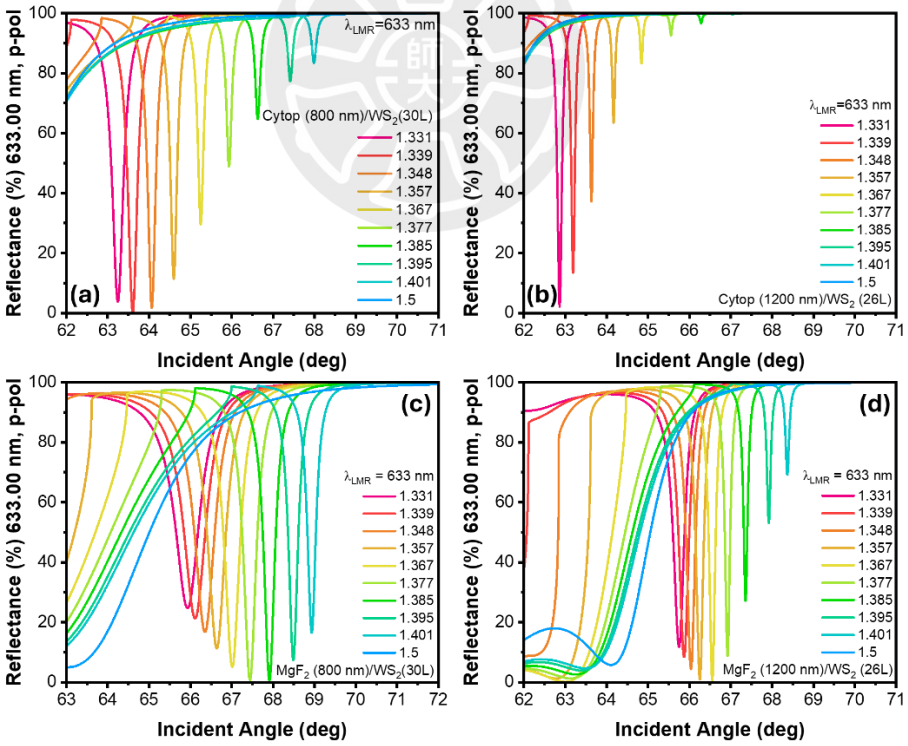

Figure D1. Response of LMR sensor excited by p-polarized light with Cytop matching layers of (a) 800 nm and (b) 1200 nm thickness. Response of LMR sensor excited by p-polarized light with MgF_2 matching layers of (c) 800 nm and (d) 1200 nm thickness.

In contrast to the LMR sensor excited with p-polarized light, the LMR sensor using s-polarized light demonstrates better signal stability within the refractive index range of 1.331 to 1.401. As shown in Figure D2, the resonance angle can still be clearly identified within this range for sensors employing either Cytop or MgF_2 as the matching layer. Remarkably, the resonance angle remains detectable even when the refractive index of the sensing medium is increased up to 1.5. This stability is consistently observed for both 200 nm and 300 nm matching layer thicknesses.

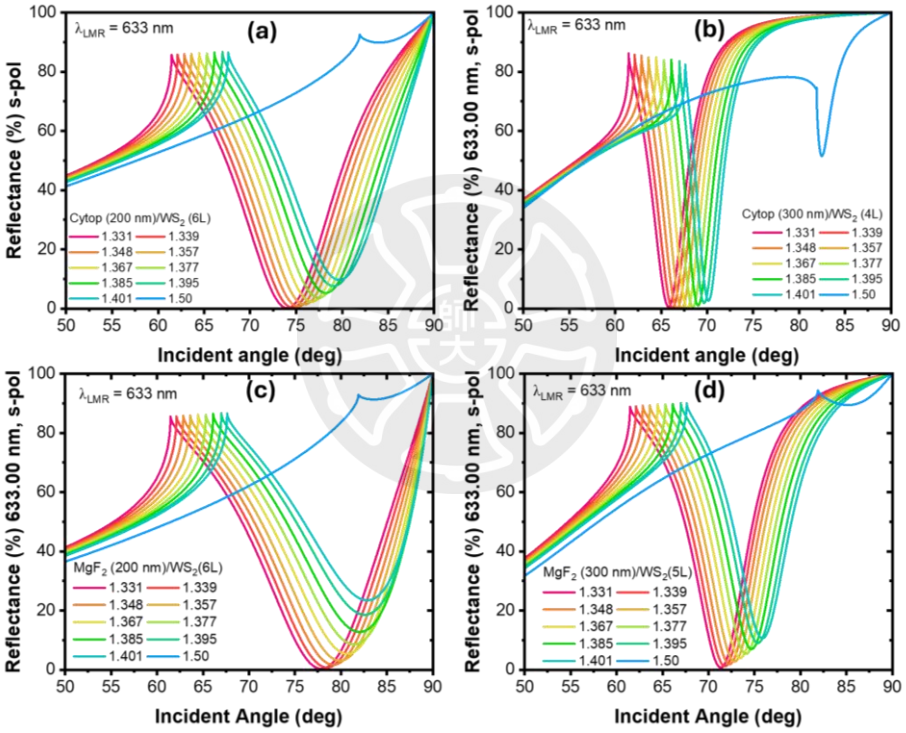

Figure D2. Response of LMR sensor excited by s-polarized light with Cytop matching layers of (a) 200 nm and (b) 300 nm thickness. Response of LMR sensor excited by s-polarized light with MgF_2 matching layers of (c) 200 nm and (d) 300 nm thickness.

Publications

1. **Devi Taufiq Nurrohman**, Nan-Fu Chiu*, *Interaction Studies of Localized Surface Plasmon Resonance Immunosensor Based on Gold Nanoparticles*, IEEE Sensors Journal 23 (17), 19262-19271 (2023).(JCR, SCI, IF 4.3 (2022); ranking 15/63= 23.8% in instruments & instrumentation). (SJR, ranking 13/141= 9.21% in Physics and Astronomy-Instrumentation) https://doi.org/10.1109/JSEN.2023.3298677
2. **Devi Taufiq Nurrohman**, Nan-Fu Chiu*, *Unraveling the Dynamics of SARS-CoV-2 Mutations: Insights from Surface Plasmon Resonance Biosensor Kinetics. Biosensors*, 14, 99 (2024). (JCR, SCI, IF 5.4 (2022); ranking 14/86= 16.28% in chemistry, analytical). (SJR, ranking 32/141=22.69% in Physics and Astronomy/ Instrumentation). https://doi.org/10.3390/bios14020099
3. **Devi Taufiq Nurrohman**, Nan-Fu Chiu*, *Molybdenum Disulfide-based Lossy Mode Resonance Sensors: Uncovering Wider Dynamic Range and High Sensitivity through Computational Approaches*, Adv. Theory Simul. 2300909, (2024). (JCR, SCI, IF 3.3 (2022); ranking 30/73= 41.09% in multidisciplinary sciences). (SJR, ranking 18/144=12.5% in Multidisciplinary/Multidisciplinary). https://doi.org/10.1002/adts.202300909
4. **Devi Taufiq Nurrohman**, Nan-Fu Chiu*, *Performance Comparison of Lossy Mode Resonance Refractive Index Sensors on Structures Based on Graphene and MoS_2, ECS* Journal of Solid State Science and Technology, (2024). (JCR, SCI, IF 1.8 (2023); ranking 306/438 = 69.86% in multidisciplinary sciences). (SJR, ranking 145/277 = 52.35% in Electronic, Optical and Magnetic Materials). https://doi.org/10.1149/2162-8777/ad325d
5. **Devi Taufiq Nurrohman**, Nan-Fu Chiu*, Yu-Sheng Hsiao, Yun-Ju Lai, Himansu Sekhar Nanda, *Advances in Nanoplasmonic Biosensors: Optimizing Performance for Exosome Detection Applications*, Biosensors, 14, 307 (2024). (JCR, SCI, IF 5.4 (2022); ranking 14/86= 16.28% in chemistry, analytical). (SJR, ranking 32/141=22.69% in Physics and Astronomy/ Instrumentation). https://doi.org/10.3390/bios14060307
6. **Devi Taufiq Nurrohman**, Gerald Reymari Acoba Cagayan, Nan-Fu Chiu, *Characterization of SPR and Cavity Modes in 1D Gold Nanograting Chips: Figure of Merit Analysis and Implications for Raman Signal Enhancement*, Optics Express, 33, 1542-1555 (2025).(JCR, SCI, IF 3.2 (2023); ranking 36/119= 30.25% in Optics).(SJR, ranking 40/214=18.69% in Physics and Astronomy/Atomic and Molecular Physics, and Optics). https://doi.org/10.1364/OE.547581